University of Alberta

A Comparison of EEG Source Localization Algorithms

by

John Philip Bruce Russell

A thesis submitted to the Faculty of Graduate Studies and Research
in partial fulfillment of the requirements for the degree of

Master of Science
in
Biomedical Engineering

Department of Electrical and Computer Engineering

Edmonton, Alberta
Fall, 2007

Library and Archives Canada

Published Heritage Branch

395 Wellington Street
Ottawa ON K1A 0N4
Canada

Bibliothèque et Archives Canada

Direction du Patrimoine de l'édition

395, rue Wellington
Ottawa ON K1A 0N4
Canada

Your file Votre référence
ISBN: 978-0-494-33337-2
Our file Notre référence
ISBN: 978-0-494-33337-2

NOTICE:
The author has granted a non-exclusive license allowing Library and Archives Canada to reproduce, publish, archive, preserve, conserve, communicate to the public by telecommunication or on the Internet, loan, distribute and sell theses worldwide, for commercial or non-commercial purposes, in microform, paper, electronic and/or any other formats.

The author retains copyright ownership and moral rights in this thesis. Neither the thesis nor substantial extracts from it may be printed or otherwise reproduced without the author's permission.

AVIS:
L'auteur a accordé une licence non exclusive permettant à la Bibliothèque et Archives Canada de reproduire, publier, archiver, sauvegarder, conserver, transmettre au public par télécommunication ou par l'Internet, prêter, distribuer et vendre des thèses partout dans le monde, à des fins commerciales ou autres, sur support microforme, papier, électronique et/ou autres formats.

L'auteur conserve la propriété du droit d'auteur et des droits moraux qui protège cette thèse. Ni la thèse ni des extraits substantiels de celle-ci ne doivent être imprimés ou autrement reproduits sans son autorisation.

In compliance with the Canadian Privacy Act some supporting forms may have been removed from this thesis.

While these forms may be included in the document page count, their removal does not represent any loss of content from the thesis.

Conformément à la loi canadienne sur la protection de la vie privée, quelques formulaires secondaires ont été enlevés de cette thèse.

Bien que ces formulaires aient inclus dans la pagination, il n'y aura aucun contenu manquant.

Canada

Abstract

An accurate electroencephalogram (EEG) source localization algorithm is an asset for the surgical treatment of patients with epilepsy. Due to the underdetermined nature of the EEG inverse problem, a variety of algorithms are applied to select the current source distribution that best accounts for the scalp recordings. We investigated five algorithms: minimum norm, LORETA, Borgiotti-Kaplan beamformer, eigenspace projection beamformer, and MUSIC. Compared over multiple SNR values, the eigenspace projection beamformer and MUSIC exhibited superior localizing capabilities while minimizing source current dispersion for the simulated seizure data. Increasing the electrode density improved the localizing capability of the beamformers and MUSIC, yet hindered the performance of minimum norm and LORETA. The five algorithms were applied to inter-ictal EEG data to localize the epileptogenic zone and the eigenspace projection beamformer proved most reliable. Redefining the signal subspace with principal and independent component analyses and the varimax rotation did little to improve localization.

Table of Contents

Chapter 1 - Introduction 1

1.1 Motivation for Research 1

1.2 Organization of Thesis 2

Chapter 2 - Background Information 3

2.1 The Electroencephalogram and the Dipole Model 3

2.2 The Forward and Inverse Problems 6

2.2.1 The Forward Problem 6

2.2.2 The Lead Field Matrix 7

2.2.3 The Inverse Problem 10

2.3 Inverse Algorithms Studied 13

2.3.1 Underdetermined Non-Adaptive Algorithms 13

2.3.2 Underdetermined Adaptive Algorithms 16

2.3.3 Overdetermined Adaptive Algorithms 20

Chapter 3 - Single Source Localization 22

3.1 Introduction 22

3.2 Materials 23

3.2.1 Head Model 23

3.2.2 Lead Field Matrix 25

3.2.3 Solution Space 25

3.3 Methods 26

3.4 Results 27

3.4.1 Example Localization Images 27

3.4.2 Localization Error 31

3.4.3 Electrode Bias 32

3.4.4 Dispersion 33

3.4.5 Dispersion with Normal Vectors 34

3.4.6 The Covariance Matrix 38

3.4.7 Computational/Time Requirements 40

3.4.8 Signal Subspace Dimensionality 41
3.5 Discussion 46
Chapter 4 - Electrode Montage Density vs. Localizing Capabilities 51
4.1 Introduction 51
4.2 Materials 51
4.2.1 Head Model 51
4.2.2 Lead Field Matrix 52
4.2.3 Solution Space 53
4.2.4 Electrode Montage 54
4.3 Methods 54
4.4 Results 55
4.5 Discussion 61
Chapter 5 - Localization of Real EEG Data 65
5.1 Introduction 65
5.2 Background Information 66
5.2.1 Principal Component Analysis 67
5.2.2 Independent Component Analysis 68
5.2.3 Varimax Rotation 69
5.3 Methods 70
5.3.1 Head Model and Solution Space 70
5.3.2 Electrode Montage 70
5.3.3 Lead Field Matrix 71
5.3.4 EEG Data 71
5.3.5 Data Window for the Covariance Matrix 74
5.3.6 Temporal Smoothing 74
5.4 Results 75
5.4.1 Localization Results Using Traditional Methods 75
5.4.2 EEG Analysis Using Advanced Methods 83
5.5 Discussion 97

Chapter 6 - Conclusions and Future Work 100

6.1 Conclusions 100

6.2 Future Work 100

Reference List 102

List of Tables

Table I – Number of voxels per tissue type 24
Table II – Tissue resistivities 25
Table III – Localization errors 32
Table IV – Quantifying electrode bias 33
Table V - Dispersions 34
Table VI – Localization error differences 35
Table VII – Normally projected dispersions 36
Table VIII – Reduction in dispersion due to normal vector projection 36
Table IX – Calculation times 41
Table X – Spherical head model resistivities 52

List of Figures

Figure 1 - Polarized pyramidal cell assembly 3
Figure 2 - Mesh resistor network between central and neighboring nodes..... 8
Figure 3 - Single slice of segmented head..... 24
Figure 4 – 32 electrode configuration 26
Figure 5 – EEG of sinusoidal source, SNR = 5 28
Figure 6 - Actual source location..... 28
Figure 7 - Inverse solution with ES Beam..... 29
Figure 8 - Inverse solution with BK Beam..... 29
Figure 9 - Inverse solution with MN..... 30
Figure 10 - Inverse solution with LORETA..... 30
Figure 11 - Inverse solution with MUSIC..... 31
Figure 12 - Localization error for various inverse algorithms..... 37
Figure 13 - Dispersion for various inverse algorithms..... 37
Figure 14 – Beamformer localization error for variable data window size..... 39
Figure 15 – MUSIC localization error for variable data window size..... 39
Figure 16 – Localization errors for variable data window size 40
Figure 17 – Actual location of three uncorrelated sinusoidal sources 42
Figure 18 – Three source inverse solutions (subspace independent)..... 43
Figure 19 – Normalized eigenvalues of three source configuration 44
Figure 20 – Three source inverse solutions (subspace dependent)..... 46
Figure 21 - Solution space for three concentric shell head model..... 54
Figure 22 – Multiple electrode configuration localization error (ES Beam)..... 56
Figure 23 – Multiple electrode configuration localization error (BK Beam)..... 56
Figure 24 – Multiple electrode configuration localization error (MN)..... 57
Figure 25 – Multiple electrode configuration localization error (LORETA)..... 57
Figure 26 – Multiple electrode configuration localization error (MUSIC)..... 58
Figure 27 – Multiple electrode configuration dispersion (ES Beam) 59
Figure 28 - Multiple electrode configurations dispersion (BK Beam)..... 59
Figure 29 – Multiple electrode configuration disepresion (MN)..... 59
Figure 30 – Multiple electrode configuration dispersion (LORETA) 60

Figure 31 – Location of 30 electrodes 71
Figure 32 – 772 sample, 29 electrode EEG 72
Figure 33 – Singular values of real EEG 73
Figure 34 – Minimum norm inverse solution 76
Figure 35 – LORETA inverse solution 76
Figure 36 – Borgiotti-Kaplan beamformer 77
Figure 37 – Eigenspace projection beamformer 78
Figure 38 – MUSIC Inverse Solution 79
Figure 39 - Portion of EEG used in consecutive images 81
Figure 40 - LORETA consecutive inverse solutions 82
Figure 41 - ES Beam consecutive inverse solutions 83
Figure 42 - Temporal principal components 84
Figure 43 – Back projected temporal components 85
Figure 44 – PC #1 inverse solution 86
Figure 45 – PC #2 Inverse solution 86
Figure 46 – Four unit variance independent components 88
Figure 47 – Back projected independent components 89
Figure 48 - Comparison of ICA and PCA eigenvectors 90
Figure 49 – IC #3 inverse solution 91
Figure 50 –IC #4 inverse solution 92
Figure 51 – Back projected varimax rotated principal components 94
Figure 52 - Comparison of PC and rotated PC eigenvectors 95
Figure 53 – Varimax rotated PC #1 inverse solution 96
Figure 54 – Varimax rotated PC #2 inverse solution 96

Chapter 1 - Introduction

1.1 Motivation for Research

Epilepsy is a disease of the central nervous system (CNS) and is classified as a seizure-related disorder that affects approximately 1% of the population [1]. Epilepsy is diagnosed when two or more seizures of an unknown cause occur. A seizure occurs when a volume of nerve cells within the cerebral cortex experience a sudden surge of synchronized electrical activity, temporarily disrupting the cells functionality. The electrical disruption can irritate surrounding cells causing the seizure to propagate to other parts of the brain. Seizures are often triggered by a small group of injured or maldeveloped neurons.

The main diagnostic tool for diagnosing seizures is the electroencephalogram (EEG) and/or the magnetoencephalogram (MEG). The ictal electrical discharges are evident in the EEG as "spike and wave" waveforms. While functional magnetic resonance imaging (fMRI), computed tomography (CT), magnetic resonance spectroscopy (MRS), and positron emission tomography (PET) may also be used for diagnostic purposes, only the E/MEG can directly measure the electrical activity of the brain. While the E/MEG exhibits superior temporal resolution compared to the aforementioned imaging techniques, the spatial resolution of the E/MEG is insufficient to directly localize the responsible cortical areas.

Seizures are classified as either partial or generalized. A partial seizure occurs when the initial discharge occurs at a localized focus while a generalized seizure has multiple foci at various locations throughout the brain. Seizure side-effects vary greatly with respect to the area of the brain that is affected. Side-effects include, but are not limited to: headaches, nausea, convulsions, shaking, immobility, increased heart rate, breathing difficulties, exhaustion, unconsciousness, pain, injuries that may be suffered during the seizure, as well as the ongoing fear of experiencing another seizure.

Some forms of epilepsy may be controlled with extensive drug treatment programs while other forms are medically intractable. For the latter cases, an alternative treatment option is to locate and surgically remove the region of the brain containing the seizure focus. Currently, there are several problems with this form of treatment that prevent patients from living a seizure-free post surgery lifestyle. The biggest problem is resolving the size and location of the seizure foci and ensuring that only the minimal amount of cortex is removed in order to minimize the loss of normal functioning gray matter. Therefore, an accurate and robust source localization algorithm would be an asset to the surgical treatment of patients suffering from epilepsy.

1.2 Organization of Thesis

This research will commence by examining the physical and mathematical problems associated with solving the EEG source localization problem. Simulated data will be used to illustrate and compare the various properties of five different inverse algorithms that are commonly used to localize electrical sources. Once a general feel for each method has been established, the methods will be applied to clinically obtained EEG data of an epileptic patient in order to compare the source localization performances under realistic conditions.

The mathematical notation used in the following research is as follows: vectors will be represented with bold, lower case letters, **v**. Matrices will be denoted with bold, capital letters, **M**. Estimated and/or predicted values are depicted with a "^" above the estimated quantity.

Chapter 2 - Background Information

2.1 The Electroencephalogram and the Dipole Model

The brain is comprised of a vast number (order of 10^{11}) of interconnected brain cells that integrate, interpret, and transport electrical signals from various regions of the brain [2]. The gray matter of the brain contains billions of pyramidal cell assemblies that act as integrators, summing excitatory and inhibitory signals received at the synapses located along the cell dendrites. During cell excitation, synaptic neurotransmitters induce a postsynaptic potential that will depolarize the dendrites at the apex of the cell. The depolarized dendrites will establish a potential difference with the cell body inducing primary and secondary currents.

Figure 1 - Polarized pyramidal cell assembly
Green dots represent the locations of excitatory post synaptic potentials [3]

The primary currents flow along the body of the pyramidal cell while the secondary currents (also known as volume currents) flow within the extracellular material of the brain in a closed-loop fashion to maintain a conservation of electrical charge [3]. The magnitude and direction of current flow of the secondary currents is a function of the inhomogeneous and anisotropic conductivities of the various tissue types within the head model. The current density at a given location is the sum of the primary current and the secondary currents induced by other sources.

A depolarized cell behaves similarly to an ideal electric dipole within a conductive medium. Therefore, for modeling and simulation purposes, active cells are modeled as electric dipoles of variable amplitude, orientation, and location.

While the EEG and MEG both indirectly measure the electrical activity within the head, they differ in their sensitivity to the two types of currents. The EEG measures potential differences between two electrode sites. Therefore, whenever there is a net current flow between two electrodes, a potential difference will result [3].

A crude MEG measurement electrode consists of small loops of wire that detect changes in magnetic flux outside of the scalp's surface. If the "right hand rule"[1] is applied to the primary and secondary currents of a depolarized pyramidal cell, the magnetic field lines of the secondary currents have a nulling effect on one another. Therefore, primary currents are the main generators of magnetic field flux.

A single postsynaptic depolarization will produce an extremely weak current of approximately 20 fA [3] yielding undetectable electric and magnetic fields at the scalp using standard clinical equipment. Due to the interconnected

---

[1] Right Hand Rule – the direction of magnetic field is in the direction your fingers on your right hand curl as you point your thumb in the direction of the current

and correlated nature of neighboring pyramidal cells, groups of neighboring cells regularly depolarize simultaneously producing a detectable net current. A 100 mm^3 volume of simultaneously depolarizing cells will produce a 10 nA current [3]. Common amplitudes of non-invasive EEG potentials are ~ 100 μV and are easily detectable with common and inexpensive surface electrode materials such as tin, gold, silver, and silver/silver chloride [4].

The magnetic fields measured at the scalp are very small (~ 10 fT) compared to other commonly occurring magnetic fields and are susceptible to corruption from external magnetic field noise. Therefore, MEG measurements are obtained in magnetically shielded rooms. In addition, superconducting quantum interference sensors (SQUIDs) are situated within a liquid helium supercooling helmet-like apparatus to increase sensor sensitivity. Due to the complexity of obtaining MEG measurements, all the simulations and data collection for the following research will be conducted with an EEG.

The EEG measures the flow of secondary currents which are influenced by both the conductivity and geometry of the head. The electrode that is closest to the region of activation does not necessarily yield the largest potential difference due to conductive properties of the tissues within the head. Therefore, the EEG cannot be relied upon to provide direct spatial information about regions of neural activity without further data analysis.

PET and fMRI are also used in neurological studies to detect changes in hemodynamic properties as a result of increased activity in active regions of the brain. While both these methods have superior spatial resolution compared to E/MEG, the temporal delay between cell activation and a measurable hemodynamic response (order of 1 s [3]) does not allow for reliable conclusions about the location and propagation of epileptic activity [5]. Conversely, the time delay between cell depolarization and detectable E/MEG scalp recordings is less than 1 ms allowing for the study of sequential electrical activity and propagation [5].

2.2 The Forward and Inverse Problems

Source localization is the process of localizing signal sources of interest from noisy measurements using an array of sensors positioned outside of the source space. The process has numerous medical, radar, and audio signal applications. In neurology, accurate source localization can provide insight and treatment possibilities for a number of neurological disorders including: epilepsy, schizophrenia, and Alzheimer's disease [3]. EEG potentials gathered from the scalp can be utilized to estimate the current density inside the head that best accounts for the measured EEG data. Source localization is subdivided into 2 complex problems: the forward problem and the inverse problem.

In order to solve both the forward and inverse problems, a realistic head model is required. Initially, the human head was approximated using a sphere. This model proved inaccurate because it did not account for the large differences in conductivities between the skull and the other tissues. An improved variation was the three concentric spherical head model which consisted of three nested spherical shells representing the cortex, skull, and scalp. Each shell had a unique conductivity. While the three concentric spherical head model was an improvement, it was still a crude approximation for a human head. A realistic head model is obtained from medical images and can more accurately account for the conductive differences between various tissue types. Realistic head models are typically discretized onto a regularized grid for computational ease.

2.2.1 The Forward Problem

The forward problem is solved to determine the scalp potentials, $\mathbf{v}(t_0)$, produced by a known internal current density, $\mathbf{j}(t_0)$, within the head. In generalized matrix form, the solution to the forward problem is [6]:

$$\mathbf{V} = \mathbf{KJ} \tag{2.1}$$

In order to perform the forward calculation, a forward operator known as the lead field matrix, **K**, must be determined. In (2.1), **V**, is a N x T matrix where N is the number of electrodes and T is the number of time samples considered. **J** is a

$3 \cdot M \times T$ matrix of discretized dipole magnitudes fluctuating over time. M is the number of voxels within the source space and each voxel may have a dipole component in three orthogonal directions [6].

The lead field matrix, **K**, accounts for the geometry and the conductivities of the various components of the head model. A single column of the lead field matrix dictates how a unit dipole source oriented along a given basis vector is seen at the various electrode locations.

For simple head models, such as the three concentric sphere model, the lead field matrix can be solved for analytically via Maxwell's and Poisson's equations [7]. For more complex models, such as the human head, the lead field matrix must be solved for numerically using the boundary element method (BEM), the finite element model (FEM) or the finite difference method (FDM) [8]. The accuracy of the lead field matrix has a direct relationship with the accuracy of any given source localization algorithm; therefore, factors such as anisotropic conductivities and tissue inhomogeneities should be included in the lead field matrix to ensure optimal localizing results.

2.2.2 The Lead Field Matrix

The determination of the lead field matrix, **K**, is the equivalent to solving the forward problem for each possible dipole location and orientation. The first step is to define an adequate head model. Realistic head models are typically generated from high resolution NMR or CT images that are segmented into various tissue types and discretized into cubic voxels. The recording electrodes are placed on the head model.

To compute the lead field matrix, a current source, I, is applied to the head model between electrode A (source) and electrode B (sink). Next, the potentials are determined at the nodes in the head model by solving Poisson's equation. Poisson's equation yields a relationship between the current sources and the resulting potentials in the head model. For the aforementioned current source/sink configuration, Poisson's equation is expressed as [8]:

$$\nabla \cdot (\sigma \nabla V) = I\delta(\mathbf{r} - \mathbf{r}_1) - I\delta(\mathbf{r} - \mathbf{r}_2) \tag{2.2}$$

For an isotropic case, σ is a position dependent conductivity scalar. For anisotropic head models, σ is a 3D conductivity tensor. The current source and sink are located at $\mathbf{r}_1$ and $\mathbf{r}_2$ respectively.

Due to the complexities of the realistic head model, Poisson's equation must be solved numerically. There are numerous techniques capable of solving for the potentials including the BEM, FEM, and FDM. Although all three methods are valid, Poisson's equation is solved for using the FDM in the current research. A more in depth description of BEM and FEM may be found in [8] and [9]. FDM was selected because it can most accurately account for tissue anisotropies and inhomogenities and FDM also produces solutions that span the entire head model, not just at specified boundaries. FDM is also more computationally efficient than BEM [8].

The FDM utilizes nodes located at the center of each voxel. A mesh resistor network is established between any given node and the six neighboring nodes. The conductivity between any two adjacent nodes can be varied to account for conductive anisotropies.

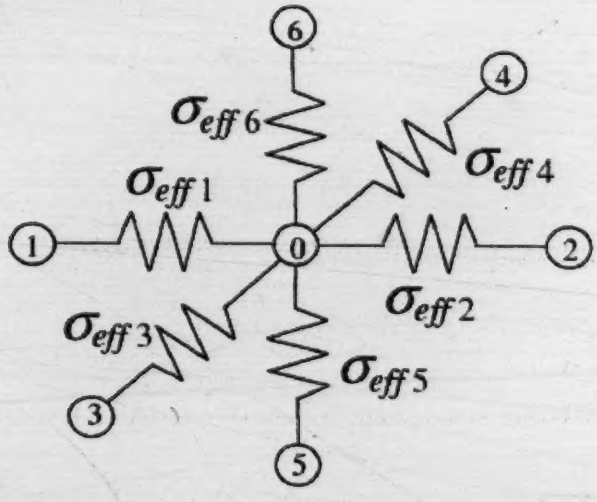

Figure 2 - Mesh resistor network between central and neighboring nodes [10]

Using a digitized head model, Poisson's equation can be re-written as follows [10]:

$$\sigma_{eff1}(v_1 - v_0) + \sigma_{eff2}(v_2 - v_0) + \sigma_{eff3}(v_3 - v_0) + \sigma_{eff4}(v_4 - v_0) + \sigma_{eff5}(v_5 - v_0) + \sigma_{eff6}(v_6 - v_0) = \frac{i_0}{h} \quad (2.3)$$

In (2.3), σ_{effi} represents the effective conductivity between the center and i^{th} node, v_i is the potential at the i^{th} node, v_0 is the potential at the center node, and i_0 is the net current flow into the central node and h is distance between adjacent nodes. From Kirchoff's Current Law, we conclude that there must be zero net current flowing into any given node, unless the node corresponds to a current source or sink. Considering all nodes, the matrix form of (2.3) is:

$$\mathbf{Av} = \mathbf{i} \quad (2.4)$$

In (2.4), **A** is a square (Q x Q, Q = number of voxels in head model) sparse symmetric system matrix containing the various inter-nodal conductivities. Each row of **A** contains a maximum of seven non-zero values. The potentials and net currents at the nodes are **v** and **i** respectively. The entries for **i** are all zeros except at the nodes containing the current source and current sink. The potential vector, **v** is solved for iteratively until the left and right hand sides of (2.4) agree within error:

$$\|\mathbf{A}_d \cdot \mathbf{v}_{dm} - \mathbf{i}_d\| < \varepsilon \quad (2.5)$$

The d subscript denotes a deflated system matrix[2]. The error tolerance level is ϵ and m denotes the number of iterations. The iterative increments are presented in [10] along with additional preconditioning techniques that facilitate convergence.

Once the potentials at the nodes are determined, we can exploit the reciprocity theorem in order to define a row of the lead field matrix. Intuitively, the reciprocity theorem can be described as follows: a current flowing between

---

[2] A deflated matrix is obtained by setting the potential at one of the nodes equal to zero.

nodes i and j inside the head, I_{ij}, will generate a potential difference between electrodes A and B, V_{AB}. Conversely, a current flowing in at electrode A and exiting via electrode B, I_{AB} will generate a potential difference across the internal nodes i and j, V_{ij}. The reciprocity theorem states that the currents and voltages will obey the following relationship [8]:

$$V_{AB} I_{AB} = V_{ij} I_{ij} \tag{2.6}$$

Generalizing (2.6) to account for a dipole source located at **r** with orientation **d**, the reciprocity theorem states that the potential generated between an electrodes A and B is:

$$V_{AB}(\mathbf{r},\mathbf{d}) = \frac{\mathbf{d}^T \cdot \nabla V(\mathbf{r})}{I_{AB}} \tag{2.7}$$

A complete mathematical derivation of (2.7) can be found in [8].

Solving Poisson's equation yields the potentials and the respective gradients needed in the numerator of (2.7). Computing the potential difference, V_{AB}, for all voxel locations, **r**, and three orthogonal directions, **d**, will generate a single row of the lead field matrix. The above process must be repeated N times to account for all the measurement electrodes and to fill all the rows of the lead field matrix.

2.2.3 The Inverse Problem

Predicting the underlying neuronal current density, **J**, that justifies a given set of measured potentials, **V**, is known as the inverse problem. Ideally, an exact mathematical inverse to **K** in (2.1) could be calculated to solve the inverse problem. Unfortunately, no such inverse exists due to the severely underdetermined nature of the inverse problem (solution space voxels, M >> number of electrodes, N). Therefore, we can only estimate the underlying current density, $\hat{\mathbf{J}}$. In the underdetermined case, there are an infinite number of source current configurations that can generate a given set of scalp potentials.

Numerous algorithms exist that estimate the neuronal current density. Each algorithm applies unique mathematical and/or physiological constraints to

select the most probable current density. The applied constraints and assumptions can introduce bias into the resulting inverse solution. Each inverse solution will be studied based on its ability to accurately localize regions of maximum electrical activity, to minimize solution dispersion, to resolve multiple electrical source configurations, and to obtain computational efficiency. For the localization of epileptic foci, an algorithm's ability to accurately locate regions of maximum electrical activity is the most important factor to consider.

Inverse algorithms perform various types of spatial filtering on the measured scalp potentials and can be categorized into non-adaptive and adaptive algorithms. The non-adaptive pseudo inverses are calculated independently of the measured scalp potentials and depend solely on the lead field matrix. Conversely, adaptive inverse algorithms incorporate the measured potentials into the derivation of spatial filter to place emphasis of regions of suspected activity. The adaptive filters are designed to be more accurate, but they are more computationally time consuming than the non-adaptive filters.

The adaptive algorithms are covariance structure based and require a sizable window of data in order to calculate the inverse solution. On the other hand, a non-adaptive inverse solution can be determined for an instantaneous slice of data. The inverse solutions can be obtained using either an underdetermined or an overdetermined source model.

2.2.3.1 Undetermined Inverse Problems

For underdetermined inverse solutions (also referred to as distributed dipole models), the solution space is discretized into many independent voxels, with each voxel containing a current source whose electrical contributions to the measured scalp potentials sum linearly. Although each dipole is fixed to a specific location, it has a variable orientation and amplitude to best account for the potentials measured at the electrode sites. Each dipole has three degrees of freedom: two for orientation and one for magnitude. In order to provide reasonable spatial resolution, the number of distributed dipoles greatly exceeds

the number of electrode sites yielding a severely underdetermined set of linear equations. Therefore, there are an infinite number of estimated distributed dipole configurations that can account for the observed data. In order to reduce the underdetermined nature of the inverse problem, a variety of physiological and mathematical assumptions and constraints are applied to the solutions to isolate the most probable of the possible solutions [5]. The underdetermined inverse algorithms do not necessarily require any à priori knowledge with respect to the number of sources needed to account for the data.

2.2.3.2 Overdetermined Inverse Problems

The overdetermined model assumes that a small number of dipole sources may be fitted onto the solution space to adequately account for the electrical activity measured on the scalp [5]. Each assumed dipole has six degrees of freedom: three for dipole location, two for dipole orientation, and one for dipole magnitude [3]. Therefore, as long as the total number of degrees of freedom for all of the assumed dipole sources does not exceed the number of data measurements (EEG electrodes), the inverse solution will be overdetermined and a unique solution will exist. Correctly predicting the number of underlying dipoles to represent the measured scalp potentials is a difficult problem that can lead to erroneous results, especially if the predicted number of sources is less than the actual number of uncorrelated sources.

The dipole(s) magnitude, location, and orientation are approximated by performing a solution space scan and determining the forward solution at each voxel location. A comparison is computed between the resulting forward solution and the measured scalp potentials and the source configuration resulting in the minimal difference is the "best-fit" solution.

2.3 Inverse Algorithms Studied

A brute force technique to solve the inverse problem would include estimating initial dipole conditions, solving the forward problem, comparing the resulting forward solution with the observed potentials, and iteratively incrementing the dipole characteristics until the resulting potentials agreed within error to the observed scalp potentials. Like most brute force methods, this technique would be both very time and memory consuming, therefore more efficient solving techniques have been developed.

Five different source localization algorithms are investigated in the following research. The algorithms studied have all been previously published with successful reviews in different experimental settings. The algorithms chosen include two underdetermined, non-adaptive filters: the minimum norm (MN) and low resolution electromagnetic tomography (LORETA), two underdetermined, adaptive filters: the eigenspace projection beamformer (ES Beam) and the Borgiotti-Kaplan beamformer (BK Beam), and one overdetermined adaptive filter: multiple signal classification (MUSIC).

2.3.1 Underdetermined Non-Adaptive Algorithms

2.3.1.1 Minimum Norm

The minimum norm algorithm constrains the estimated current density by minimizing the overall power of the inverse solution [6]:

$$\min_{\hat{\mathbf{j}}}\left(\hat{\mathbf{j}}^T\hat{\mathbf{j}}\right), \text{ subject to } \mathbf{v}=\mathbf{K}\hat{\mathbf{j}} \tag{2.8}$$

The solution to (2.8) is [6]:

$$\hat{\mathbf{j}}=\mathbf{T}\mathbf{v} \text{ where } \mathbf{T}=\mathbf{K}^T\left[\mathbf{K}\mathbf{K}^T\right]^{-1} \tag{2.9}$$

Although the MN pseudo inverse is elegantly simple, its power minimizing regime introduces bias into the inverse solution. Intuitively, this bias

can be understood by examining electric dipole behavior. The potential of an electric dipole in free space is given by [11]:

$$V_{dip}(\mathbf{r}) = \frac{\hat{\mathbf{r}} \cdot \mathbf{p}}{4\pi\varepsilon_0 r^2} \tag{2.10}$$

Where $\mathbf{r}$ is the vector between the measurement point and dipole center, $\hat{\mathbf{r}}$ is the corresponding unit vector, $\mathbf{p}$ is the dipole moment, and ϵ_0 is the permittivity of free space. The dipole moment, $\mathbf{p}$, is a function of the dipole properties, including its magnitude. It is important to notice the $\mathbf{p}/r^2$ factor in (2.10) because it is responsible for introducing an electrode bias in all MN solutions. In trying to achieve a given potential at location $\mathbf{r}$, the $\mathbf{p}/r^2$ ratio must remain fixed. Therefore, the dipole magnitude, $\mathbf{p}$, may be minimized provided that r^2 is reduced proportionately. The reduction in r^2 will pull the estimated dipole location towards an electrode site, biasing the minimized solution. Sources located deeper within the solution space are drawn closer to the surface during the minimization process. The validity of the physiological assumption of minimum energy also comes into question during discussions of the MN algorithm [5].

2.3.1.2 Low Resolution Brain Electromagnetic Tomography

LORETA is similar to the MN algorithm (2.9) with the exception of an additional weighting matrix, $\mathbf{W}$, in the pseudo inverse, $\mathbf{T}$ [6]:

$$\mathbf{T} = \mathbf{W}^{-1}\mathbf{K}^T\left[\mathbf{K}\mathbf{W}^{-1}\mathbf{K}^T\right]^{-1} \tag{2.11}$$

The matrix $\mathbf{W}$ performs solution smoothing and depth weighting to improve the MN estimation. $\mathbf{W}$ incorporates a 3D Laplacian high pass filter, $\mathbf{B}$, to enhance the edges/transitions in the amplitudes of $\hat{\mathbf{j}}$. Minimizing the energy of an edge enhanced image yields a maximally smooth solution. A smoothed solution is desirable because it emphasizes the interconnected and correlated nature of neighboring pyramidal cell assemblies. The high pass filter $\mathbf{B}$ is derived by

locating and weighting the nearest neighbors (side, edge, and corner) of every voxel.

The square matrix **W** also provides depth weighting for the voxels located deeper within the solution space to offset the bias suffered in MN solutions. The depth weighting for a particular voxel, j, is derived from the lead field matrix by [6]:

$$\Delta_{jj} = \sqrt{\sum_{i=1}^{N} \mathbf{k}_{ij}^T \mathbf{k}_{ij}} \tag{2.12}$$

Where $\mathbf{k}_{ij}^T = \left[k_{ij,x}, k_{ij,y}, k_{ij,z}\right]$, N is the number of electrodes and j = 1,...,M and M is the number of voxels in the solution space. The depth weighting for a particular voxel applies in the x, y, and z directions.

Taking both the Laplacian high pass filter, **B**, and depth weighting operator, **Δ** into account, the LORETA weighting matrix in (2.11) is [6]:

$$\mathbf{W} = (\Delta \otimes \mathbf{I}_3)\mathbf{B}^T\mathbf{B}(\Delta \otimes \mathbf{I}_3) \tag{2.13}$$

where $\otimes$ is the Kronecker product. It is computationally difficult to invert $\mathbf{B}^T\mathbf{B}$ as needed in (2.11), therefore the inverse of the high pass filter is replaced with a low pass filter.

Consistent with all smoothing operators, the resulting estimated current density suffers from considerable "blurring". One of the major quandaries with the LORETA algorithm is the volume over which correlated behavior can be correctly assumed. Arguments have been made that the region of assumed correlated behavior should be made on a physiological and anatomical basis instead of just physical proximity to prevent the blurred solution from spreading over multiple lobes and hemispheres [5]. Unfortunately, doing so would greatly complicate the LORETA algorithm beyond the scope of this research.

2.3.2 Underdetermined Adaptive Algorithms

2.3.2.1 Beamformer Basics

The underdetermined adaptive algorithms investigated are two variations of "beamformers". Beamformers use the data collected at the sensors to discriminate the amount of signal originating from each possible location [3]. They are a series of spatial "pass" and "stop" bands that allow signal to pass from only specified locations of interest while attenuating signals originating elsewhere [12]. Beamformers are regarded as virtual electrodes that scan the entire solution space measuring the signal emitted from each voxel. The estimated magnitude of a dipole at voxel location **r**, with orientation η, at time t, is the dot product of the measured potentials and a weighting vector [13], [14]:

$$\hat{j}(\mathbf{r},\eta,t) = \mathbf{w}^T(\mathbf{r},\eta)\mathbf{v}(t) \tag{2.14}$$

The derivation of the weighting vector, **w**, specifies the beamformer type. Each voxel of the solution space has three weights; one for each orthogonal direction. Due to the severely underdetermined nature of the inverse problem, sharp "pass" and "stop" bands are unattainable due to the high number of degrees of freedom. Instead, the stop bands are focused over other voxels that are emitting significant energy [13]. These "significant" voxel locations are determined from the covariance structure of the EEG. If EEG data, **V**, is sampled T times such that each column represents an instantaneous measurement of all N electrode potentials, then the covariance matrix is defined as:

$$\mathbf{R} = \frac{\mathbf{V}\mathbf{V}^T}{NT} \tag{2.15}$$

The two beamformers examined are extensions of the minimum variance beamformer (MV Beam). The three dimensional (i = x, y, z) MV Beam weightings are derived in order to minimize the energy of the inverse solution given the following set of constraints [13]:

$$
\begin{aligned}
&\min_{\mathbf{w}_x}\left(\mathbf{w}_x^T\mathbf{R}\mathbf{w}_x\right), \text{ constrained by:}\\
&\mathbf{w}_x^T\mathbf{k}_x(\mathbf{r})=1,\ \mathbf{w}_x^T\mathbf{k}_y(\mathbf{r})=0,\ \mathbf{w}_x^T\mathbf{k}_z(\mathbf{r})=0\\
&\min_{\mathbf{w}_y}\left(\mathbf{w}_y^T\mathbf{R}\mathbf{w}_y\right), \text{ constrained by:}\\
&\mathbf{w}_y^T\mathbf{k}_x(\mathbf{r})=0,\ \mathbf{w}_y^T\mathbf{k}_y(\mathbf{r})=1,\ \mathbf{w}_y^T\mathbf{k}_z(\mathbf{r})=0\\
&\min_{\mathbf{w}_z}\left(\mathbf{w}_z^T\mathbf{R}\mathbf{w}_z\right), \text{ constrained by:}\\
&\mathbf{w}_z^T\mathbf{k}_x(\mathbf{r})=0,\ \mathbf{w}_z^T\mathbf{k}_y(\mathbf{r})=0,\ \mathbf{w}_z^T\mathbf{k}_z(\mathbf{r})=1
\end{aligned}
\tag{2.16}
$$

$\mathbf{k}_\eta(\mathbf{r})$ is a single column of the lead field matrix, $\mathbf{K}$, corresponding to a single dipole located at $\mathbf{r}$, oriented in the η direction. The constraints in (2.16) illustrate the pass and stop bands enforced by the weighting vectors. Eq. (2.16) can be solved for using Lagrange multipliers and the vectorized solution for the MV Beam weights in (2.16) for a voxel located at $\mathbf{r}$ is [15]:

$$
\left[\mathbf{w}_x,\mathbf{w}_y,\mathbf{w}_z\right]=\mathbf{R}^{-1}\mathbf{K}(\mathbf{r})\left[\mathbf{K}^T(\mathbf{r})\mathbf{R}^{-1}\mathbf{K}(\mathbf{r})\right]^{-1}\mathbf{I}_3 \tag{2.17}
$$

where $\mathbf{I}_3$ is a 3 x 3 identity matrix. Appropriate transformation matrices would be applied if other non-Cartesian coordinate systems were used.

During simulations, the number of active sources does not normally exceed the number of electrodes. Therefore, $\mathbf{R}$ is not a full rank matrix and is not invertible. This problem may be rectified by inverting the regularized inverse $\left(\mathbf{R}+\gamma\mathbf{I}\right)^{-1}$ [13] where γ is called the regularization parameter. This is the equivalent to adding white noise with power equivalent to γ to the measured data to ensure a full rank covariance matrix. While the regularized inverse will be more stable and less susceptible to gross errors due to minute errors in the lead field matrix, the spatial resolution of the estimated current density will suffer from the added noise [16].

Beamformers produce erroneous results when the source configuration contains multiple sources experiencing some degree of correlation. Under these circumstances, the covariance matrix cannot discriminate between the correlated portions of the sources resulting in the possible suppression of the correlated

sources and the formation of phantom sources located elsewhere. The errors associated with correlated sources help justify the null constraints in (2.16). If the orthogonal null constraints are not present, the orthogonal components of a single dipole behave like two correlated sources and suppress one another [16].

2.3.2.2 Borgiotti-Kaplan Beamformer

The Borgiotti-Kaplan beamformer (BK Beam) is an extension of MV Beam with modified constraints to ensure unity white noise gain. The estimated noise power at a given location is:

$$\hat{P}(\mathbf{r},\eta)_{Noise} = \mathbf{w}^T(\mathbf{r},\eta)\mathbf{R}_{Noise}\mathbf{w}(\mathbf{r},\eta) \tag{2.18}$$

The covariance matrix of the white noise, $\mathbf{R}_{Noise}$ is equal to the power of the white noise detected at the electrode sites, $\mathbf{R}_{Noise} = \sigma^2\mathbf{I}$.

$$\hat{P}(\mathbf{r},\eta)_{Noise} = \mathbf{w}^T(\mathbf{r},\eta)\sigma^2\mathbf{I}\mathbf{w}(\mathbf{r},\eta) \tag{2.19}$$

To ensure the desired unity white noise gain:

$$\mathbf{w}^T(\mathbf{r},\eta)\mathbf{w}(\mathbf{r},\eta) = 1 \tag{2.20}$$

This constraint replaces the unity constraints in (2.16) while the null constraints remain the same.

$$\begin{aligned} &\mathbf{w}_x^T\mathbf{w}_x = 1,\ \mathbf{w}_x^T\mathbf{k}_y(\mathbf{r}) = 0,\ \mathbf{w}_x^T\mathbf{k}_z(\mathbf{r}) = 0 \\ &\mathbf{w}_y^T\mathbf{k}_x(\mathbf{r}) = 0,\ \mathbf{w}_y^T\mathbf{w}_y = 1,\ \mathbf{w}_y^T\mathbf{k}_z(\mathbf{r}) = 0 \\ &\mathbf{w}_z^T\mathbf{k}_x(\mathbf{r}) = 0,\ \mathbf{w}_z^T\mathbf{k}_y(\mathbf{r}) = 0,\ \mathbf{w}_z^T\mathbf{w}_z = 1 \end{aligned} \tag{2.21}$$

The BK Beam weights are [13]:

$$\mathbf{w}_\eta = \frac{\mathbf{R}^{-1}\mathbf{K}(\mathbf{r})\left[\mathbf{K}^T(\mathbf{r})\mathbf{R}^{-1}\mathbf{K}(\mathbf{r})\right]^{-1}\mathbf{f}_\eta}{\sqrt{\mathbf{f}_\eta^T\Omega\mathbf{f}_\eta}} \tag{2.22}$$

Where $\mathbf{f}_\eta$ is the unit vector for orientation η and

$$\Omega = \left[\mathbf{K}^T(\mathbf{r})\mathbf{R}^{-1}\mathbf{K}(\mathbf{r})\right]^{-1}\mathbf{K}^T(\mathbf{r})\mathbf{R}^{-2}\mathbf{K}(\mathbf{r})\left[\mathbf{K}^T(\mathbf{r})\mathbf{R}^{-1}\mathbf{K}(\mathbf{r})\right]^{-1} \tag{2.23}$$

2.3.2.3 Eigenspace Projection Beamformer

The eigenspace projection beamformer (ES Beam) projects the weights derived with BK Beam (2.22) onto the signal subspace of **V**. The data covariance matrix, **R**, can be factored via eigenvalue decomposition into signal and noise subspaces [16]. If the power of the white noise is known to be σ^2, then we can deduce that eigenvectors whose corresponding eigenvalues are greater than σ^2 define the signal subspace and eigenvectors with corresponding eigenvalues less than σ^2 define the noise subspace. The decomposition of **R** is [16]:

$$\mathbf{R} = \mathbf{E}_S \Lambda_S \mathbf{E}_S^T + \mathbf{E}_N \Lambda_N \mathbf{E}_N^T \tag{2.24}$$

$\mathbf{E}_S$ and $\mathbf{E}_N$ are matrices whose columns are the eigenvectors of the signal and noise subspaces respectively. Λ_S and Λ_N are diagonal matrices of the corresponding eigenvalues. The weights derived with BK Beam (2.22) are projected onto the signal eigenvectors of **R** [13]:

$$\tilde{\mathbf{w}}_\eta = \mathbf{E}_S \mathbf{E}_S^T \mathbf{w}_\eta \tag{2.25}$$

The number of eigenvectors representing the signal subspace is equal to the number of uncorrelated sources. In order to accurately factor the covariance matrix into signal and noise subspaces, the number of sources or the noise power must be known à priori. This can pose problems when decomposing actual EEG data, where the number of sources or white noise power is unknown. ES Beam can extract a maximum of N uncorrelated sources from the data covariance structure. If all of the eigenvectors are used in the projection, $\mathbf{E}_S \mathbf{E}_S^T = \mathbf{I}$ and ES Beam devolves into BK Beam.

The advantages of ES Beam with respect to BK Beam or MV Beam become evident when there are differences in the actual and estimated lead field matrices. The signal to noise ratios for MV Beam and the ES Beam with a single current dipole located at **r** is [16]:

$$SNR_{MV} = \frac{\hat{P}_S}{\hat{P}_N} = \frac{P_S}{\sigma^2} \frac{\left[\hat{\mathbf{k}}^T(\mathbf{r}) \Gamma_S \mathbf{k}(\mathbf{r})\right]^2}{\left[\hat{\mathbf{k}}^T(\mathbf{r}) \Gamma_S^2 \hat{\mathbf{k}}(\mathbf{r}) + \hat{\mathbf{k}}^T(\mathbf{r}) \Gamma_N^2 \hat{\mathbf{k}}(\mathbf{r})\right]} \tag{2.26}$$

$$SNR_{ES} = \frac{\hat{P}_S}{\hat{P}_N} = \frac{P_S}{\sigma^2} \frac{\left[\hat{\mathbf{k}}^T(\mathbf{r})\Gamma_S \mathbf{k}(\mathbf{r})\right]^2}{\left[\hat{\mathbf{k}}^T(\mathbf{r})\Gamma_S^2 \hat{\mathbf{k}}(\mathbf{r})\right]} \tag{2.27}$$

Where " ^ " denotes the estimated values while symbols without the " ^ " represent the actual values. Γ_S and Γ_N are the inverses of the signal and noise subspaces respectively. P_S is the actual power of the underlying current density and σ^2 is the power of the white noise. Theoretically, the second term in the denominator of (2.26) should approach zero because the noise subspace is orthogonal to the lead field vectors. If the $\hat{\mathbf{k}}^T(\mathbf{r})\Gamma_N^2 \hat{\mathbf{k}}(\mathbf{r})$ term does go to zero, both MV and ES Beam have identical SNRs. Unfortunately, when using a realistic head model, the lead field vectors can only be approximated and we cannot assume othogonality with the noise subspace. Therefore, the second term does not go to zero and the SNR decreases for MV Beam. When analyzing real EEG data, defining the noise subspace can be problematic yielding decreased SNRs as well. ES Beam is used to increase the SNR of the inverse solution.

2.3.3 Overdetermined Adaptive Algorithms

2.3.3.1 Multiple Signal Classification

Multiple signal classification (MUSIC) is the overdetermined dipole fitting algorithm that will be examined for the sake of comparison. Like ES Beam, MUSIC uses eigenvalue decomposition to factor **R** into signal and noise subspaces. The working assumption behind MUSIC is that the noise subspace is orthogonal to the lead field matrix at source locations [17].

Like ES Beam, the number of sources must be known à priori to determine the dimensionality of the signal and noise subspaces. Once the signal subspace has been factored from the covariance matrix, a full solution space scan is performed simulating dipoles at each possible location and orientation. A cost

function comparing the degree of orthogonality between the lead field matrix and the noise subspace is computed for each location and orientation.

$$C(\mathbf{r},\theta) = \left\| \left(\mathbf{I} - \mathbf{E}_S \mathbf{E}_S^T\right) \mathbf{k}(\mathbf{r},\theta) \right\|_2 \tag{2.28}$$

$\mathbf{E}_S$ is the signal subspace as defined in (2.24) and therefore $\left(\mathbf{I} - \mathbf{E}_S \mathbf{E}_S^T\right)$ is the noise subspace. At actual source locations, the noise subspace and the lead field matrix are orthogonal and theoretically, the cost function, C should go to zero. The dipole configuration yielding the minimal cost function is assumed the correct source distribution [17]. Multiple minima occur for multiple sources. The cost function in (2.28) can be inverted to mimic a scaled probability density function with maxima located at the minima of (2.28).

$$pdf(\mathbf{r},\theta) = -\log_{10}\left(C(\mathbf{r},\theta)\right) \tag{2.29}$$

Like ES Beam, problems arise when there are multiple sources suffering from some degree of correlation. The computational complexity of the MUSIC algorithm increases with the number of assumed sources.

Chapter 3 - Single Source Localization

3.1 Introduction

When comparing epileptic source localization algorithms, the most important criterion to examine is the algorithm's ability to correctly predict the location of maximum electrical activity. Simulations are performed using a single point source positioned within the solution space at a known location. The forward solution, V, is calculated using (2.1). The inverse solution is estimated using the ES Beam, BK Beam, MN, LORETA, and MUSIC algorithms. The distance between the global maxima for the five inverse solutions are compared with the actual source location to quantify the bias/error of each algorithm. Multiple trials with unique source locations are executed to reduce head geometry and electrode bias.

Once the global maxima are located, the bias introduced by the electrode configuration and depth weighting is quantified by comparing the differences in mean source to electrode distances between the actual source location and the estimated maxima. This will determine if any of the inverse solutions are biased towards a more 'electrode dense' location.

The dispersion (blurring) of the four underdetermined inverse solutions is also determined to estimate the full-width half maxima of the estimated current distributions. Dispersion measurements cannot be performed for MUSIC because the inverse solution is equivalent to a probability density function and does not represent a distribution of source magnitudes.

It is anatomically known that the pyramidal cells of the cortex are oriented normally to the cortical surface [18]. This additional à priori knowledge spatially filters the previously determined inverse solutions by projecting the dipole magnitudes onto the normal vectors. The effects on localization, dispersion, and the robustness to noise are subsequently examined.

The adaptive inverse algorithms, ES Beam, BK Beam, and MUSIC, utilize a window of EEG data to estimate the covariance structure, **R**, in order to determine their respective weighting vectors and solution subspace estimations. The robustness of **R** is dependent on the number of data samples used to calculate it in (2.15). If too few samples are used, spurious correlations may result. Conversely, too many samples are computationally inefficient and assumptions of a stationary source over the entire data sampling period may be violated. Therefore, localization simulations are conducted with an increasing number of data points in order to determine an optimum data sampling window size.

3.2 Materials

3.2.1 Head Model

A realistic head model is used for the single source localization simulations. Geometric details were obtained from T1 weighted NMR images. The head model consists of 176 slices; each slice is 228 x 171 pixels for a total of 6 861 888 voxels. The head model was digitized onto a regular grid with 1 mm resolution. The head model was segmented using a semi-automatic dynamic edge tracer segmentation algorithm into eight tissue types: cerebellum and pons, grey matter/cortex, ventricles and cerebral spinal fluid, white matter, diencephalon (grey matter), skull, scalp, and cerebrospinal fluid surrounding the cortex [19].

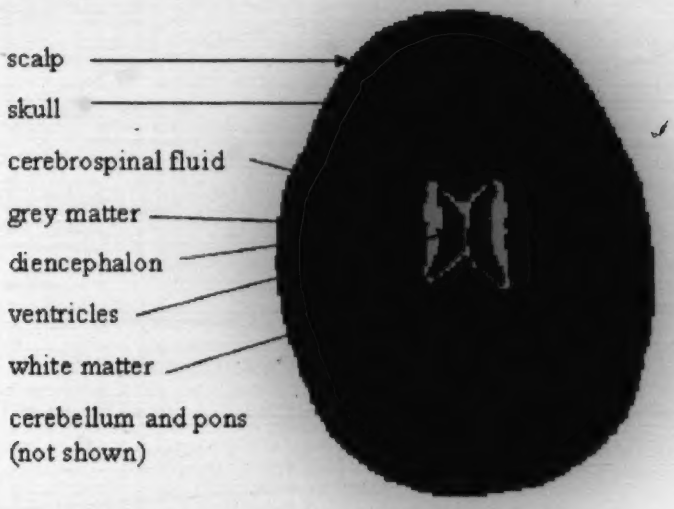

Figure 3 - Single slice of segmented head

The number of voxels for each tissue type is given in Table I.

Table I – Number of voxels per tissue type

Tissue Type	Number of Voxels
Background	4 840 525
Cerebellum and Pons	118 107
Grey Matter (cortex)	455 477
Ventricles and Cerebrospinal Fluid	13 326
White Matter	349 611
Diencephalon (grey matter)	30 459
Skull	393 402
Scalp	499 238
Cerebrospinal Fluid (surrounding cortex)	161 743
TOTAL	6 861 888

The resistivities for the various tissues are listed in Table II [20], [21]:

Table II – Tissue resistivities

Tissue Type	Resistivity (Ω·cm)
Cerebellum and Pons	300
Grey Matter (cortex)	300
Ventricles and Cerebrospinal Fluid	65
White Matter	700
Grey Matter (not cortex)	300
Skull	9000
Scalp	275
Cerebrospinal Fluid	65

The highly resistive skull attenuates the volume currents and causes a great deal of current dispersion before the current reaches the outer surface of the scalp [22]. Therefore, a detailed representation of the variations in skull thickness is of utmost importance to an accurate head model.

3.2.2 Lead Field Matrix

The lead field matrix was solved for using the finite difference method (FDM) in conjunction with the reciprocity theorem as detailed in [10]. The isotropic conductivities used to define the system matrix in (2.4) are given in Table II.

3.2.3 Solution Space

The solution space is defined as a single layer of gray matter along the cortical gray matter - white matter boundary. The solution space consisted of 61 041 voxels, 1 mm^3 in volume. A normal unit vector corresponding to the direction of minimal cortex thickness was determined at each voxel location.

3.3 Methods

Once the head model and solution space were segmented using [19] and the lead field matrix computed using [10], the forward solution for the scalp potentials, **V**, could be accurately determined. The EEG was simulated using a single 17 Hz sinusoidal source with amplitude of 1, located within a randomly chosen solution space voxel. The scalp potentials are calculated via (2.1) at 32 independent point electrodes. The electrode locations are shown in Figure 4.

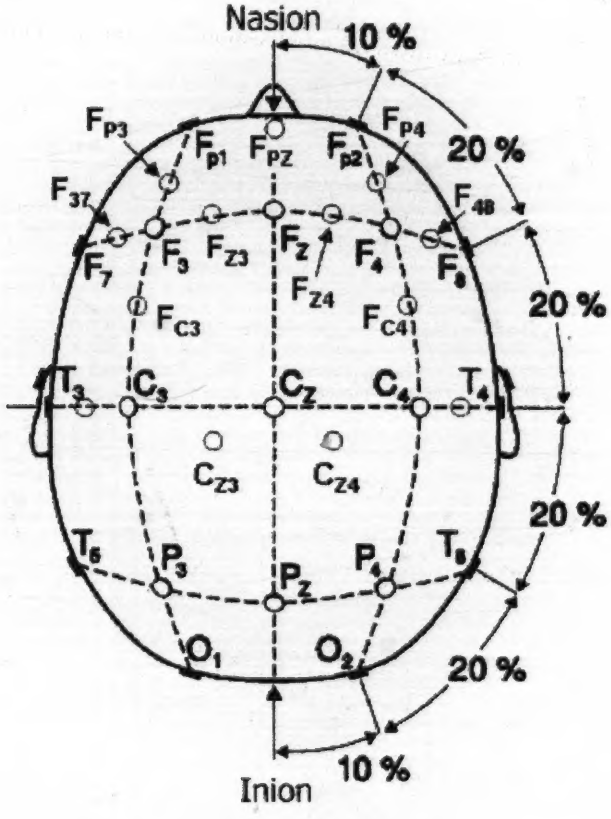

Figure 4 – 32 electrode configuration

The EEG is sampled at 256 Hz for one second. Gaussian white noise is added to **V** at the 32 electrode sites. The signal to noise ratio (SNR) is defined as

the ratio of the sums of the eigenvalues of the signal and noise covariance matrices. For the following simulations, SNR values of 10, 5, and 2 are used in order to be consistent with the lower, middle, and upper noise levels observed with a phantom human head [23]. In addition to simulating more realistic measurement conditions, the added noise also ensures an invertible full rank covariance.

The five inverse solutions are solved for using the previously discussed techniques. For the adaptive algorithms, all 256 samples are used to calculate **R**. A single eigenvector corresponding to the largest eigenvalue is used to define the signal subspace for the ES Beam and MUSIC algorithms. The LORETA smoothing operator used to simulate $\left(\mathbf{B}^T\mathbf{B}\right)^{-1}$ in (2.13), uses the immediate neighboring side, edge, and corner voxels.

Although the adaptive algorithms utilized the entire data window, the instantaneous inverse solution is only determined for the first time slice in which the actual source amplitude is 1. Unless otherwise stated, the aforementioned techniques for generating the forward and inverse solutions are used for all subsequent simulations.

3.4 Results

3.4.1 Example Localization Images

An EEG generated with a single sinusoidal source and a SNR = 5 is shown in Figure 5.

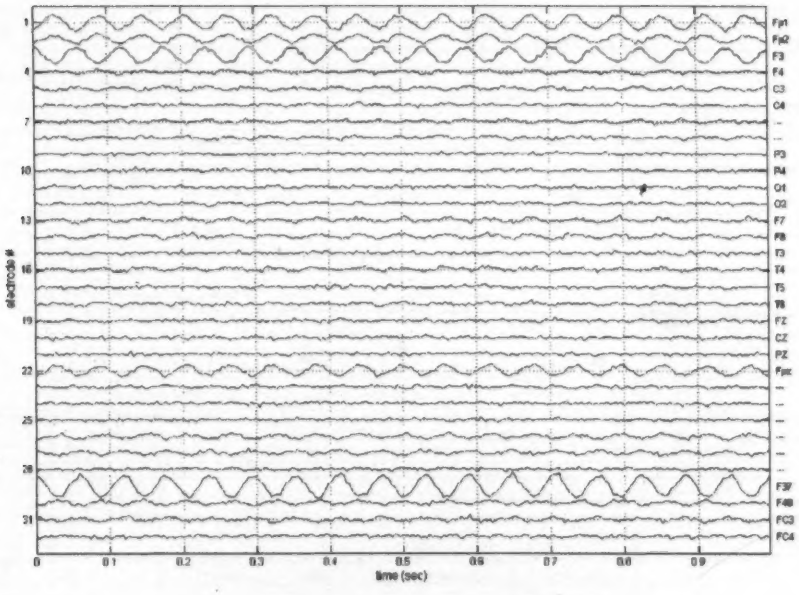

Figure 5 – EEG of sinusoidal source, SNR = 5

The location of the source is shown in Figure 6. It is blurred out to encompass a larger area for easier viewing.

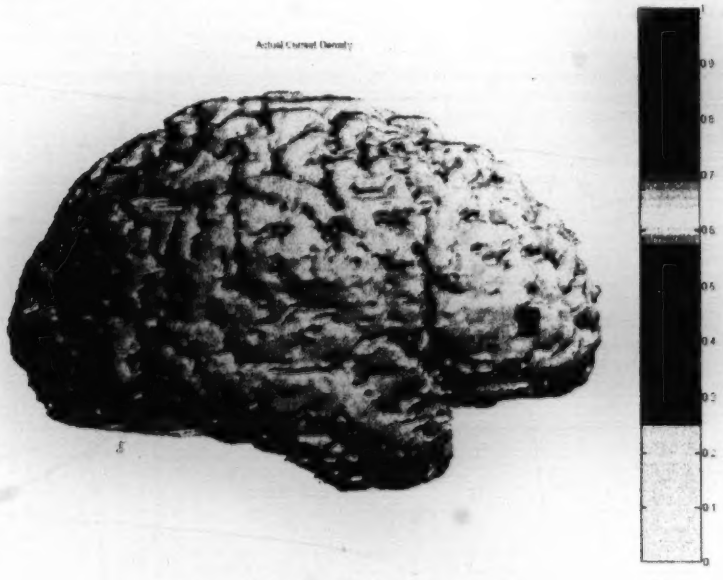

Figure 6 - Actual source location

The inverse solutions using ES Beam, BK Beam, MN, LORETA, and MUSIC are shown in Figures 7 – 11.

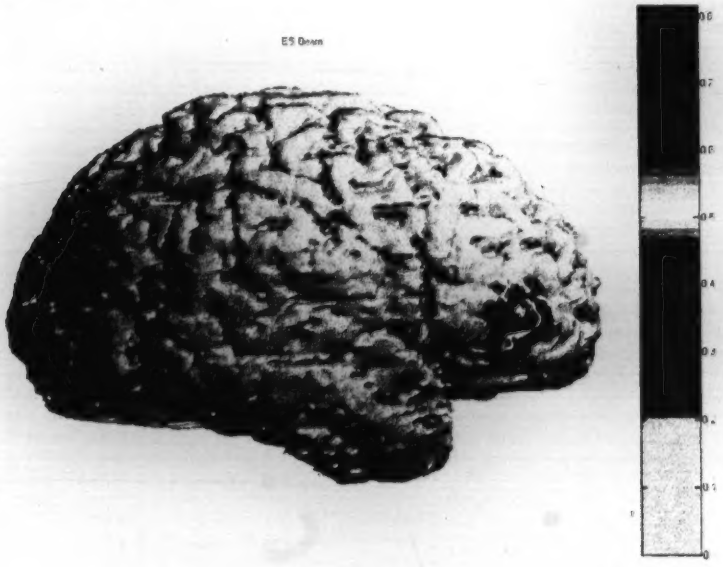

Figure 7 - Inverse solution with ES Beam

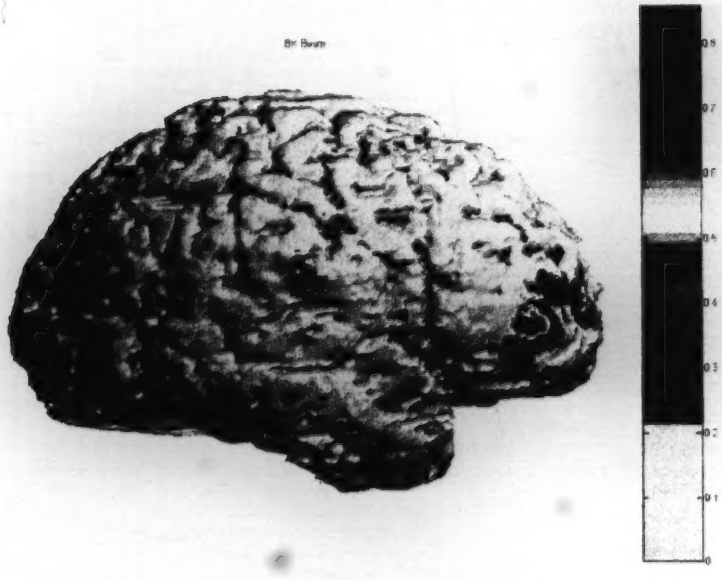

Figure 8 - Inverse solution with BK Beam

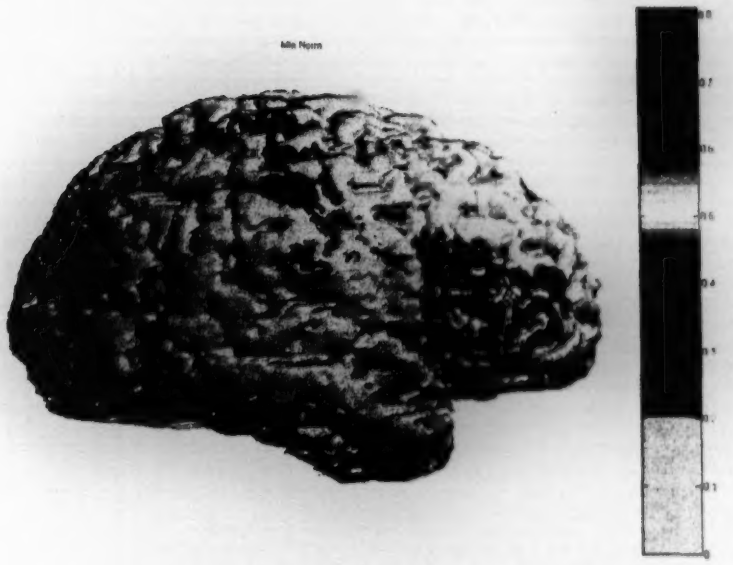

Figure 9 - Inverse solution with MN

Figure 10 - Inverse solution with LORETA

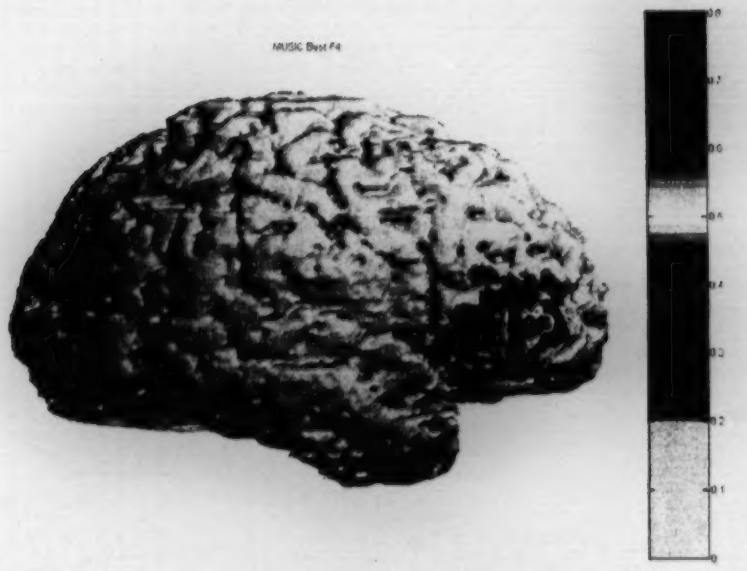

Figure 11 - Inverse solution with MUSIC

3.4.2 Localization Error

Although each inverse algorithm determines the dipole's magnitude and orientation, only the magnitude determines the location of the estimated current density maximum, $\hat{\mathbf{j}}_{max}$. For the underdetermined inverse algorithms, the localization error is defined as the Euclidean distance between the actual dipole location and the global maximum of $\hat{\mathbf{j}}$. The localization error for MUSIC is the straight line distance between the actual source location and the location of the probability density function maximum.

Due to the aforementioned limitations of the various inverse algorithms, the chosen location of the actual dipole source will greatly affect the localizing capabilities of each algorithm. For example, we expect a source located deep within a sulcus or relatively far from any given electrode will be biased towards an electrode. To partially remove this bias from subsequent results, 100 trials were conducted with randomly chosen source locations.

The localization errors for the five inverse algorithms with SNRs of 10, 5, and 2 are listed in Table III. Results are expressed as the mean ± standard errors of the mean for the 100 trials.

Table III – Localization errors

	Localization Error (mm)		
	SNR = 10	SNR = 5	SNR = 2
ES Beam	0.55 ± 0.08	0.93 ± 0.12	1.90 ± 0.25
BK Beam	0.73 ± 0.11	1.37 ± 0.13	4.19 ± 1.17
MN	50.87 ± 3.36	55.03 ± 3.52	66.30 ± 3.61
LORETA	50.48 ± 3.38	57.35 ± 3.58	67.79 ± 3.68
MUSIC	0.39 ± 0.10	0.67 ± 0.11	1.20 ± 0.13

3.4.3 Electrode Bias

Some of the documented flaws of the non-adaptive inverse algorithms, such as MN and LORETA, are their tendencies to bias the inverse solution towards the electrodes in order to minimize overall energy. Little has been reported with respect to the bias the electrodes exert on the inverse solutions of the adaptive beamforming algorithms. To quantify the severity of the bias exerted by the electrodes, the mean distance from the source location, $\mathbf{r}_{max}$, to all 32 electrodes, $\mathbf{e}_i$, is compared to the mean distance from the estimated peak, $\hat{\mathbf{r}}_{max}$ to the same 32 electrodes.

$$Bias = \frac{1}{N}\left(\sum_{i=1}^{N}\left\|\mathbf{r}_{max} - \mathbf{e}_i\right\|_2 - \sum_{i=1}^{N}\left\|\hat{\mathbf{r}}_{max} - \mathbf{e}_i\right\|_2\right) \tag{3.1}$$

It is interesting to note that an estimated peak may be biased away from the nearest electrode towards a more electrode dense location. For this reason, all electrode sites are considered, instead of just the distance to the nearest electrode. A positive bias in (3.1) represents a move to a more 'electrode dense' location.

The electrode biases for all five algorithms are listed in Table IV. Results are expressed as the mean ± standard errors of the mean for the 100 trials.

Table IV – Quantifying electrode bias

	Electrode Bias (mm)		
	SNR = 10	SNR = 5	SNR = 2
ES Beam	0.01 ± 0.01	0.01 ± 0.01	0.02 ± 0.02
BK Beam	0.01 ± 0.01	0.01 ± 0.01	0.01 ± 0.04
MN	0.71 ± 0.27	0.99 ± 0.33	1.38 ± 0.32
LORETA	0.41 ± 0.27	1.03 ± 0.30	0.99 ± 0.32
MUSIC	0.01 ± 0.01	-0.01 ± 0.01	-0.01 ± 0.01

3.4.4 Dispersion

The estimated current density exhibits varying degrees of dispersion (or blurring) due to the underdetermined nature of the inverse problem. The sharpness of the inverse solution increases the resolving power of multiple source configurations. Due to the nonsymmetrical nature of the solution space and the resulting inverse solutions, standard full-width half maximum measurements could not be taken. The distance between the maximum and the half power contour line depends on the direction of the radial path taken from the maximum. Therefore, the dispersion was quantified via:

$$dispersion = \sqrt{\sum_{N} \hat{j}(\mathbf{r})(\mathbf{r}-\mathbf{r}_{max})^2} \tag{3.2}$$

In (3.2), N is the number of voxels with a dipole magnitude greater or equal to $\hat{j}_{max}/2$. The location of the estimated current density peak is $\mathbf{r}_{max}$. For the calculation of the dispersion in (3.2), $\hat{\mathbf{j}}$ is normalized so that $\hat{j}(\mathbf{r}_{max}) = 1$.

Dispersion is calculated for the four underdetermined algorithms, but not for the overdetermined MUSIC algorithm because the output of MUSIC is equivalent to a probability density function and not a series of dipole magnitudes. The various dispersions for SNRs of 10, 5, and 2 are listed in Table IV. Results are expressed as the mean ± standard errors of the mean for the 100 trials.

Table V - Dispersions

	Dispersion (mm)		
	SNR = 10	SNR = 5	SNR = 2
ES Beam	30.6 ± 3.0	51.9 ± 4.4	121.9 ± 9.3
BK Beam	38.3 ± 4.1	128.0 ± 42.2	1202.7 ± 212.5
MN	829.4 ± 62.0	847.2 ± 63.3	793.8 ± 47.5
LORETA	1135.3 ± 86.4	1074.1 ± 81.2	1038.2 ± 69.7

3.4.5 Dispersion with Normal Vectors

Pyramidal cell assemblies are oriented normally to the cortical surface [18]. Therefore, in order to reduce the effects of noise, the three dimensional underdetermined inverse solutions are projected onto the normal vectors associated with each voxel location. The normal vectors correspond to the direction of minimum cortical thickness at each voxel location. It is reasonable to assume that incorrectly estimated sources resulting from noise are not likely to be oriented normally to the cortical surface and experience substantial attenuation upon normal vector projection. The projection operation is applied after each dipole's location and orientation is determined.

An alternative approach to cortical normal vector exploitation is to multiply the three (x, y, z) lead field matrix column vectors of the i^{th} voxel by the corresponding i^{th} normal unit vector:

$$\begin{bmatrix} \mathbf{k}_i^x & \mathbf{k}_i^y & \mathbf{k}_i^z \\ \vdots & \vdots & \vdots \end{bmatrix} \begin{bmatrix} \hat{x}_i \\ \hat{y}_i \\ \hat{z}_i \end{bmatrix} = \mathbf{k}_i \tag{3.3}$$

This yields a single lead field matrix column vector for each voxel instead of three vectors per voxel. Using this technique, the dipole orientations of the resulting inverse solutions are defined along the normal directions and expressed only as a dipole magnitude. This technique reduces the memory requirements and computing time of the various algorithms by two thirds, but does not reduce the effects of noise on inverse solution dispersion. Therefore, the normal vector projection is applied as a post processing filter after the dipole properties are determined.

The resulting differences between the localization errors for the standard and normally projected inverse solutions are shown in Table VI. A positive difference infers that the normalized solution yields improved localization. Results are expressed as the mean difference for the 100 trials.

Table VI – Localization error differences

	Difference in Localization Errors (mm)		
	SNR = 10	SNR = 5	SNR = 2
ES Beam	-0.01	0.02	0.63
BK Beam	0.02	0.42	-0.13
MN	1.13	-2.42	-0.76
LORETA	-0.71	1.18	1.05

The dispersions of the normally projected inverse solutions with SNRs of 10, 5, and 2 are listed in Table VII. Results are expressed as the mean ± standard errors of the mean for the 100 trials.

Table VII – Normally projected dispersions

	Dispersion (mm)		
	SNR = 10	SNR = 5	SNR = 2
ES Beam	16.6 ± 2.1	27.6 ± 2.8	62.3 ± 4.8
BK Beam	22.0 ± 3.1	90.0 ± 33.0	762.4 ± 133.9
MN	492.6 ± 40.8	420.7 ± 35.1	410.3 ± 25.3
LORETA	612.2 ± 46.8	556.7 ± 42.7	550.7 ± 36.2

By comparing the dispersions in Table V and Table VII, we see that the additional à priori knowledge with respect to the solution space anatomy reduces the dispersion considerably as shown in Table VIII.

Table VIII – Reduction in dispersion due to normal vector projection

	Reduction in Dispersion (%)		
	SNR = 10	SNR = 5	SNR = 2
ES Beam	46%	47%	49%
BK Beam	43%	30%	37%
MN	41%	50%	48%
LORETA	46%	48%	47%

A summary of the localization errors and dispersions for the various algorithms are shown in Figure 12 and Figure 13.

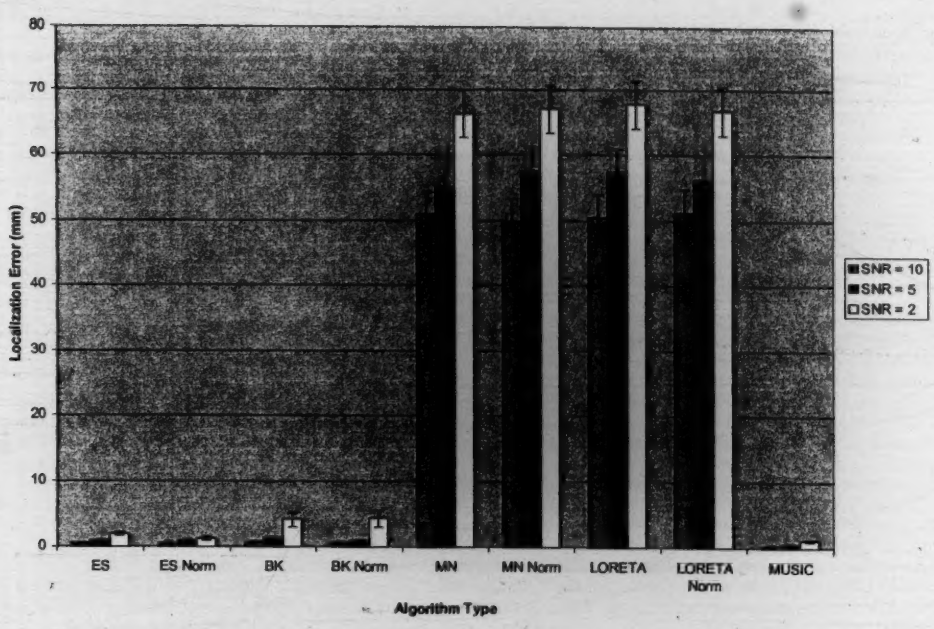

Figure 12 - Localization error for various inverse algorithms

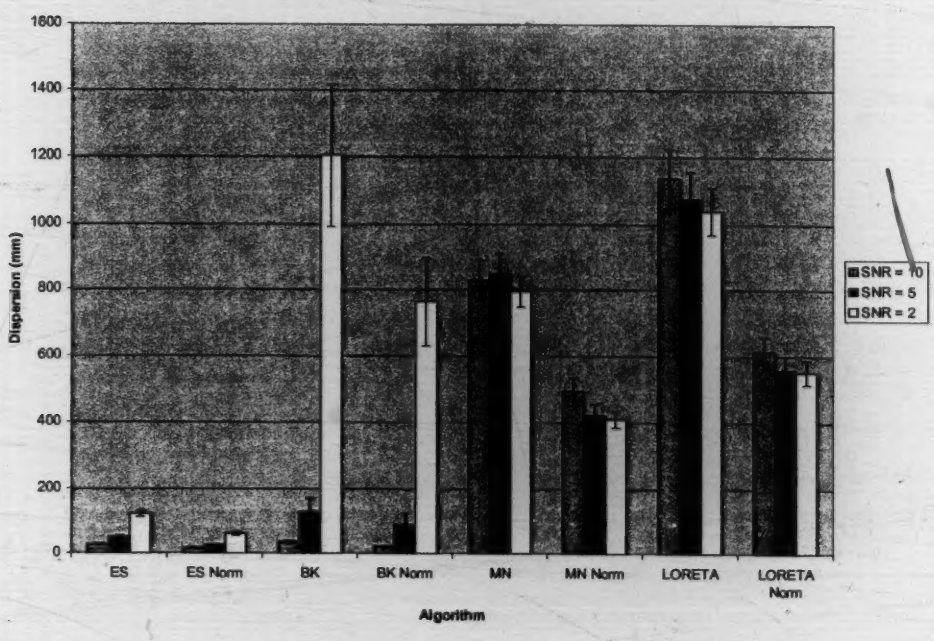

Figure 13 - Dispersion for various inverse algorithms

3.4.6 The Covariance Matrix

The robustness of the covariance matrix used to determine the adaptive (ES Beam, BK Beam, and MUSIC) inverse solutions depends on the number of data samples used to calculate **R** (2.15). If too few samples are used, spurious correlations may result. On the other hand, too many samples are computationally burdensome and may violate stationary source assumptions. When computing **R** and extracting the relevant signal subspace, we assume that the location and number of sources remains constant. If **R** is sampled over too long of a time interval, these assumptions may no longer be valid.

To determine the minimum number of samples required to provide a robust estimate of **R**, a single 17 Hz, radially oriented, source is positioned on a gyrus of the solution space. A gyrus is selected for the source location because it will reduce depth related localization errors. As in the previous simulations, the EEG is calculated using (2.1) and sampled at 256 Hz for one second. Noise is added to the entire EEG data matrix to produce the desired SNR. The number of samples used to calculate **R** ranged from 1 to 256 in single increments starting at the t = 0 sample. To ensure a full rank invertible covariance matrix for BK and ES Beam, a regularization parameter [13] is added to the diagonal elements of **R**.

For each estimate of **R**, the underlying neural electric activity was estimated using ES Beam, BK Beam, and MUSIC. Ten trials were conducted at each increment. The localization error for each algorithm was averaged over the 10 trials. The simulation was conducted with SNRs of 10, 5, and 2.

Since the single source is positioned on a solution space gyrus, it was more accurately localized than other possible deeper sources. For such a favorable source location, there were only slight differences in the ES Beam and BK Beam localization errors. For simplicity, only one trace representing both beamformer's behavior is shown in Figure 14. The localization error versus the data window size for SNRs of 10, 5, and 2 for the beamformer and MUSIC are plotted in Figures 14 and 15 respectively.

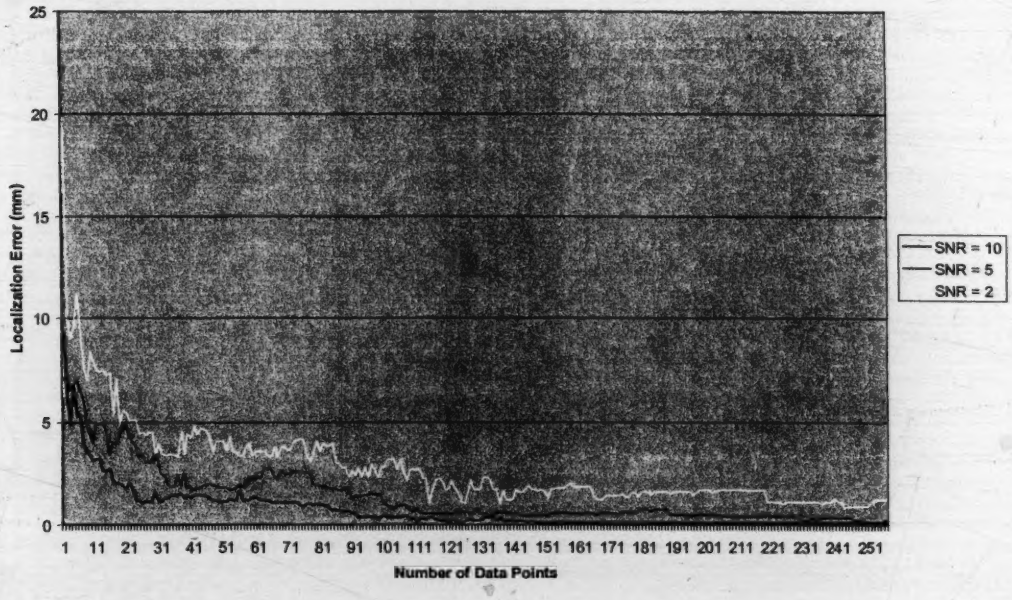

Figure 14 – Beamformer localization error for variable data window size

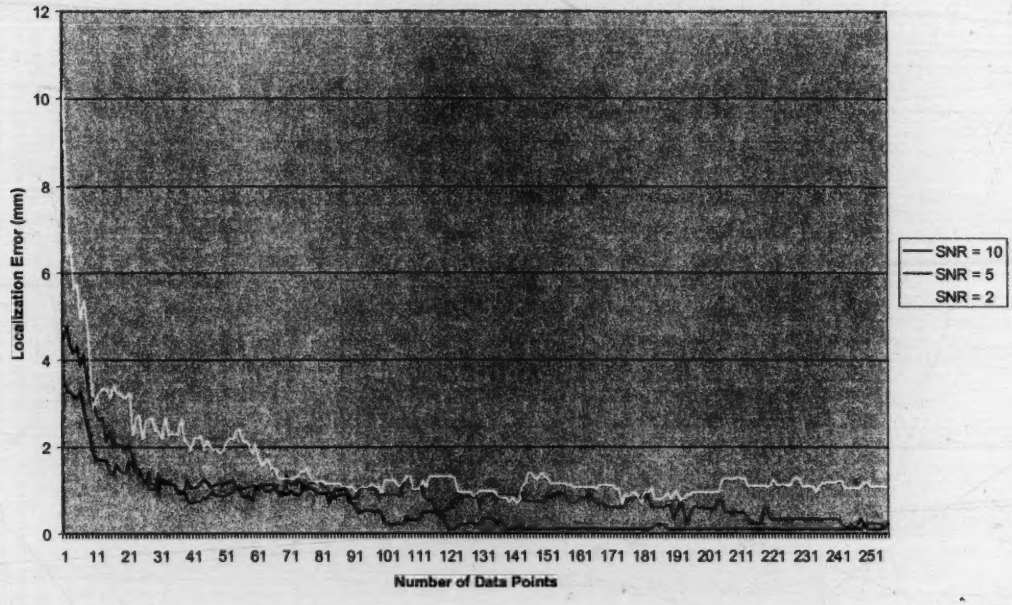

Figure 15 – MUSIC localization error for variable data window size

A comparison between the beamformer and MUSIC, with a SNR = 2, is shown in Figure 16.

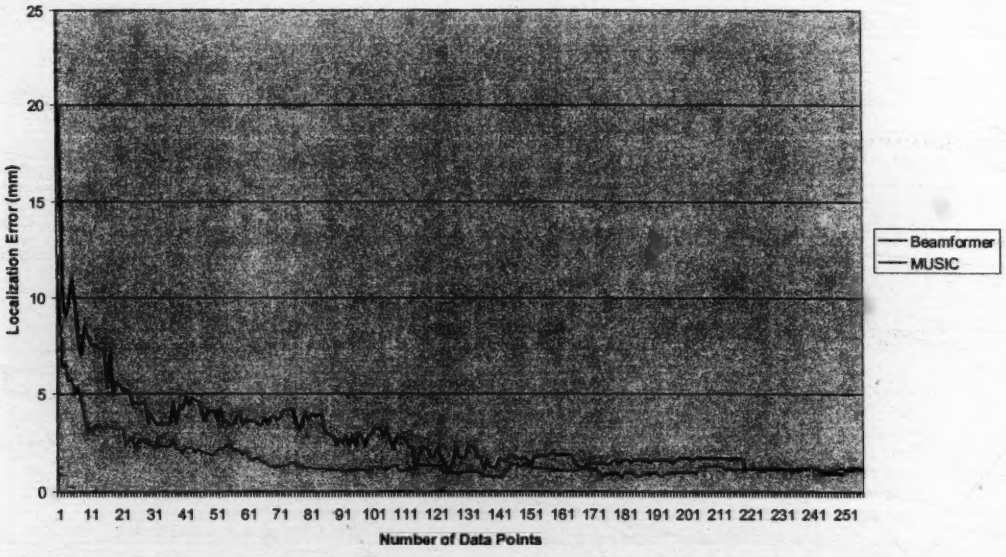

Figure 16 – Beamformer and MUSIC localization errors for variable data window size

3.4.7 Computational/Time Requirements

While the localizing capabilities of the non-adaptive algorithms are inferior to those of the adaptive algorithms, the computational efficiency and speed of the non-adaptive algorithms are far superior. The computational demands of calculating the pseudo inverses, **T**, may be quite burdensome depending of the number of electrodes and the resolution of the solution space. Although, once **T** has been determined for a given head model, it is applied to all inverse calculations using an identical head model and electrode configuration. Therefore, the inverse solution for subsequent time slices is calculated via simple matrix multiplication (2.9). On the other hand, the inverse solutions for the adaptive beamforming techniques are calculated on an individual time slice basis due to the sliding covariance matrix window, yielding long computational times

for each EEG sample. Initial and subsequent time slice calculation times for the adaptive and non-adaptive algorithms are listed in
Table IX. Calculations were executed using MATLAB 7 with a 3.2 GHz processor.

Table IX – Calculation times

	Calculation times (seconds)	
	Initial Calculation	Subsequent Calculations
Adaptive	17.5	17.5
Non-Adaptive	9.0	1.5

3.4.8 Signal Subspace Dimensionality

The adaptive inverse algorithms that use signal subspace projection (ES Beam and MUSIC) require à priori knowledge with respect to the number of underlying sources. When the number of sources is known, it is obvious how many eigenvectors/dimensions are needed to adequately map the signal subspace, but if the number of sources is unknown, problems arise.

The following simulation uses multiple dipole sources to form an EEG. Three uncorrelated, radially oriented, sinusoidal sources with frequencies of 13 Hz, 17 Hz, and 21 Hz are situated at considerable distances from one another. The locations of the three sources are shown in Figure 17.

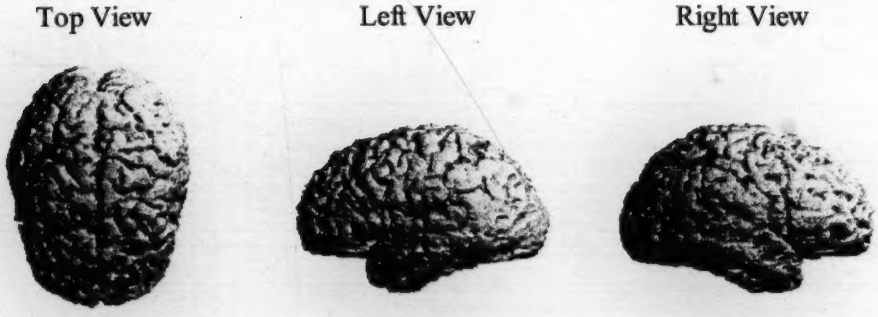

Figure 17 – Actual location of three uncorrelated sinusoidal sources

Noise with a SNR = 5 is added at the electrode sites. The inverse solutions are calculated using all five inverse algorithms. Inverse solutions that are not signal subspace specific (BK Beam, MN, and LORETA) are shown in Figure 18 to illustrate multi source performance.

Borgiotti-Kaplan Beamformer

Minimum Norm

LORETA

Figure 18 – Inverse solutions for three source configuration using signal subspace independent algorithms

Comparing the three inverse distributions, it is evident that both MN and LORETA indicate a phantom source located in the frontal lobe. This is of interest because it coincides with the region with the highest electrode density. The BK Beam adequately resolves three separate sources while the other two algorithms tend to blend the three sources into a single phantom source.

Ideally, the three eigenvectors corresponding to the three largest eigenvalues will define the signal subspace needed for ES Beam and MUSIC. Subsequent adaptive inverse solutions are determined for both over and underestimated signal subspace dimensionalities/ranks.

The normalized eigenvalues, shown in Figure 19, illustrate the percentage of power contained in each dimension.

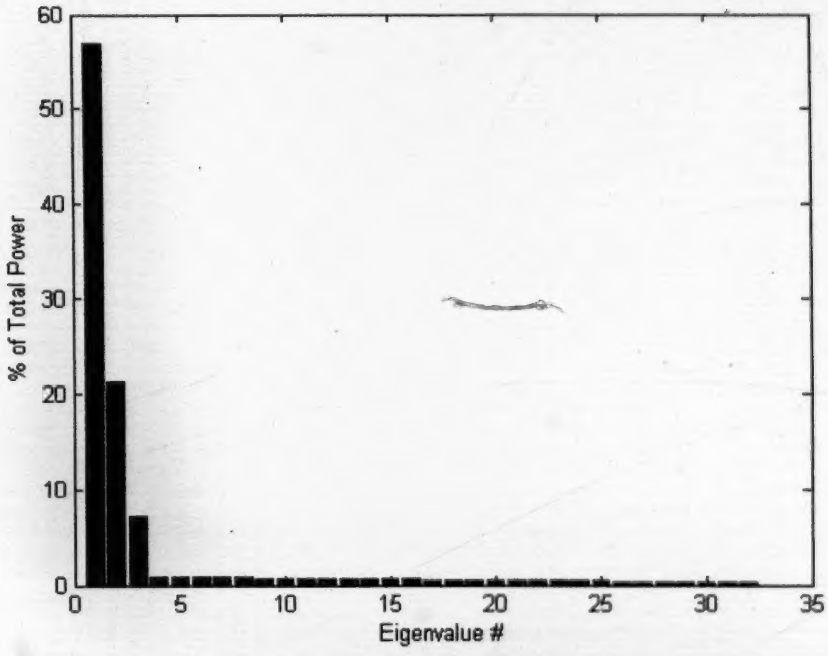

Figure 19 – Normalized eigenvalues of three source configuration

Inverse solutions with a signal subspace dimensionality/rank of one, three, and ten are shown below. The one, three, and ten dimensional subspaces account for 57.0%, 85.2%, and 90.4% of the total EEG power respectively.

Top View	Left View	Right View
Rank = 1		
ES Beam		
		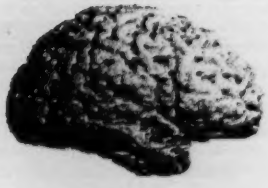
MUSIC		
Rank = 3		
ES Beam		

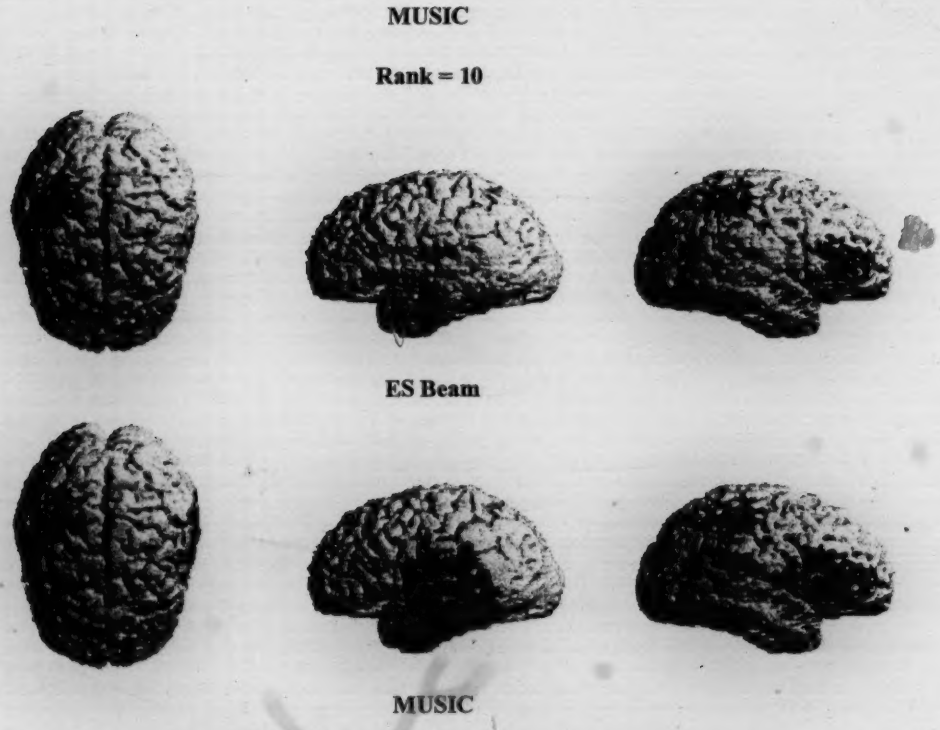

Figure 20 – Inverse solutions for three source configuration using signal subspace dependent algorithms with a variable dimensionality/rank of signal subspace

3.5 Discussion

The localization errors listed in Table III illustrate the accuracy of the three adaptive algorithms. Regardless of noise level, MUSIC localizes most accurately, followed by ES Beam and BK Beam. As the SNR decreases, the signal subspace specific algorithms (ES Beam and MUSIC) illustrate a robustness that is not present with BK Beam. This is an expected result since MUSIC and ES Beam factor the desired signal subspace from the noisy EEG before proceeding with localization. The MN and LORETA inverse solutions are very similar to one another and neither is capable of producing accurate results. The errors of the non-adaptive algorithms in a low noise environment are substantially larger than the results obtained at the highest noise levels with the adaptive algorithms.

The results in Table IV show that there is a definite trend for the non-adaptive algorithms (MN and LORETA) to bias the inverse solutions towards regions of greater electrode density. The accurate results obtained for the adaptive algorithms illustrate a greater immunity to electrode bias. These results are consistent with the shortcomings of the non-adaptive algorithms mentioned in the literature [5] and [6].

Incorporating the anatomical normal vector projection operator into the localization algorithms yields neutral and positive results. Differences in peak localization error are minimal with slight improvements for the normally projected current source distributions. The largest improvement in localization error is 1.18 mm. While this appears to be a significant improvement, it only represents a 3.48% decrease in localization error due to the large errors already associated with the LORETA algorithm.

The normally projected solution reduces the dispersion by a relatively constant amount (37% $\rightarrow$ 50%) for all four underdetermined algorithms across the entire range of signal to noise ratios (Table VIII). The reduced dispersion in conjunction with the albeit slight reduction in localization error creates a more focused and precise inverse solution. In order to take full advantage of these benefits, high resolution medical images and rigorous segmentation programs are required to accurately map the solution space. Without accurate solution space details, the normal projection operator could have negative effects on source localization.

Figures 14 and 15 illustrate how the localization error may be reduced by increasing the number of data samples used to estimate the covariance structure, **R**. Relatively constant localization errors were achieved when the number of samples exceeds 150. This is equivalent to approximately 0.6 seconds of data. At this point, an adequately representative covariance structure is established. Although additional data points do not affect the localization error, they can handicap adaptive algorithms with respect to computational efficiency.

The numerical results (150 samples, 0.6 seconds) cannot be assumed to be concrete thresholds for adequate localization. Data threshold levels are dependent upon the electrode configuration, number of underlying dipole sources, noise levels, and the duration of source stationarity. This simulation was conducted to illustrate the generalized trend in localization error with respect to an increasing number of data points.

Increasing the number of data points used to estimate **R** also helps reduce the effects of noise. From Figures 14 and 15, we see larger differences between localization errors at different noise levels when the data window is small. As the data window increases in size, the differences in the localization error become less dependent on the noise level. Greater data window sizes help eliminate false correlations within the noise matrix.

Figure 16 is a comparison of the localization errors of the beamformer and MUSIC algorithms with a SNR = 2 as the data window size is increased. From Figure 16, it is evident that MUSIC requires substantially less data than the beamformer to produce minimal localization error. The localization error of the beamformer approaches the performance of MUSIC given a large enough data window (approximately 220 samples in the above scenario). MUSIC yields smaller localization errors with a small data window because the algorithm does not require an inverted covariance matrix like the beamformers. Therefore, MUSIC does not require a full rank covariance matrix or the use of regularization parameter that has been shown to degrade spatial resolution [13].

Table IX shows the differences in the computation times for non-adaptive algorithms and the beamformers. With the given head model, deriving a single set of beamforming weights requires almost twice as much time as the derivation of a non-adaptive pseudo inverse. Since the weightings are constantly updated, beamformers can become quite time and memory consuming.

The computational time for MUSIC depends on the complexity of the hypothesized source configuration. For example, it takes substantially longer to perform a solution space scan with multiple dipoles than just a single dipole.

More complicated beamforming algorithms have been proposed that perform a rough scan of the solution space to generate a crude picture of the electrical activity. Subsequently, beamforming techniques are only applied to regions of suspected activity as opposed to the entire solution space to reduce the computation time [24].

The three source simulations in Section 3.4.8 illustrate the importance of accurately predicting the number of underlying sources for ES Beam and MUSIC. When the dimensionality of the signal subspace is underestimated (i.e. Rank = 1), ES Beam yields one dominant source and a secondary source of much smaller magnitude. On the other hand, MUSIC is confined to yielding a single source that theoretically contributes the greatest proportion of power to the EEG. Unlike MUSIC, ES Beam can still generate other sources that are still visible on the cortical surface, but these secondary sources are greatly attenuated by the signal subspace projection coefficient in the derivation of the weightings (2.25).

When the dimensionality of the signal subspace is chosen correctly (Rank = 3), three distinct sources are visible for both ES Beam and MUSIC. The sources are generally in the correct locations. Searches for local maxima disclose localization errors of 1 mm, 1.41 mm, and 1.73 mm for the three sources. The locations of the local maxima were identical for the two algorithms. It would appear that the ES Beam algorithm yields more localized results, but this conclusion is misleading due to the difference in algorithm interpretations. The output of MUSIC is a probability density function for the locations of the best-fit dipoles while ES Beam outputs the degree of electrical activity at each voxel site. Therefore, the dispersion of the two algorithms cannot be compared.

Overestimating the dimensionality of the signal subspace (Rank = 10) has only minor effects on the quality of the inverse solutions. Increasing the dimensionality from three to ten is equivalent to generating pass filters for an additional 5.2% of the EEGs total power. It is assumed that the small amount of additional power is almost entirely due to noise and the resulting inverse solutions will suffer from poorer localization and increased dispersion. The localization

errors for the three sources using ES Beam are 0 mm, 3.32 mm, and 1.41 mm and the errors using MUSIC are 1.41 mm, 3.32 mm, and 1.41 mm. The localization errors tend to increase for each additional noise-related eigenvector included in the signal subspace estimation. The MUSIC probability density function consists of 10 local maxima, but maxima (dipoles) four through ten are too weak to be visible.

The previous simulations illustrate that it is wise to err on the cautious side when estimating the dimensionality of the signal subspace. If the rank is over estimated, localization will suffer slightly and inverse solution dispersion will increase, but the overall picture is still evident. On the other hand, underestimating the number of possible sources can greatly hinder localization results producing either phantom sources or the omission/attenuation of significant sources.

Chapter 4 - Electrode Montage Density vs. Localizing Capabilities

4.1 Introduction

The locations of the measurement electrodes significantly bias the inverse solutions of non-adaptive algorithms like MN and LORETA. The effects of electrode bias have been noted in [5], [22], as well as section 3.4.3. The bias is a result of the inverse solutions pulling towards regions of higher electrode density in order to minimize the total energy. A logical step to reduce the bias would include increasing the density of the electrode montage. Theoretically, if each possible source location is in close proximity to an electrode, the dipole at that location will experience less bias, yielding a more accurate inverse solution.

Additional electrodes reduce the underdetermined nature of the inverse problem and therefore should produce more accurate results with increased topographical resolution [5]. Additional electrodes can also yield a more accurate covariance structure. This will help adaptive algorithms reduce the effects of additive random noise. This effect is similar to how increasing the number of EEG data points reduces the number of spurious positive correlations. This theory assumes that the additional electrodes do not produce an increase in noise that cannot be "adequately accounted for" [5].

4.2 Materials

4.2.1 Head Model

Due to the complexities, time constraints, and inaccuracies associated with computing the lead field matrix for a realistic head model, a concentric three shell head model was used for the following simulations. The three concentric shells are homogeneous with isotropic conductivities consistent with measured cortex,

skull, and scalp values. The resistivities for the cortex, skull, and scalp are shown in Table X.

Table X – Spherical head model resistivities

Tissue Type	Resistivity $(\Omega \cdot cm)$
Cortex	350
Skull	28 000
Scalp	350

4.2.2 Lead Field Matrix

The lead field matrix for a realistic head model is estimated numerically while analytic solutions exist for simpler head models such as the three concentric shell head model [3]. An exact lead field matrix will eliminate a possible source of error for inverse solutions and will generate a more precise picture of how the electrode density affects the localizing capabilities of the various inverse algorithms.

The lead field matrix for a three concentric sphere head model is computed using the methods discussed in [25]. The scalp potential measured at a given point on the outer shell surface with spherical coordinates (R, α, β) is [25]:

$$V(R,\alpha,\beta)=\frac{1}{4\pi\sigma}\sum_{n=1}^{\infty}\frac{2n+1}{n}\bar{b}^{n-1}\left[\frac{\xi(2n+1)^2}{d_n(n+1)}\right] \cdot\left[n\bar{m}_r P_n(\cos\alpha)+\bar{m}_t P_n^1(\cos\alpha)\cos\beta\right] \tag{4.1}$$

where $\bar{b}$ is the eccentricity of the dipole in the three concentric sphere head model, σ is the conductivity of the cortex and the scalp and σ_s is the conductivity of the skull. $\xi = \sigma_s/\sigma$ is the ratio between the skull and cortex conductivities. The radial and tangential components of the dipole are $\bar{m}_r$ and $\bar{m}_t$ respectively. P_n and P_n^1 are the Legendre and associated Legendre polynomials. Only the first 50 Legendre and associated Legendre polynomials were used to solve (4.1).
In (4.1),

$$d_n = \left[(n+1)\xi + n\right]\left[\frac{n\xi}{n+1} + 1\right] + (1-\xi)\left[(n+1)\xi + n\right] \cdot \left(f_1^{2n+1} - f_2^{2n+1}\right) - n(1-\xi)^2 \left(\frac{f_1}{f_2}\right)^{2n+1} \tag{4.2}$$

The inner and outer skull radii are r_1 = 8.7 cm and r_2 = 9.2 cm respectively. The outer scalp radius is R = 10 cm. In (4.2), $f_1 = r_1/R$ and $f_2 = r_2/R$.

A single column of the lead field matrix is equivalent to the solution of (4.1) with a unity dipole source oriented along a coordinate system basis vector.

4.2.3 Solution Space

The solution space is a 1 mm thick spherical shell with a radius of 8.5 cm and consists of 51 741 current dipoles. Defining the solution space on the surface of a shell of a constant radius will eliminate any errors associated with depth weighting that detract from the MN and LORETA inverse solutions. The solution space does not consist of the full spherical shell, but a truncated shell with the bottom section removed to more accurately represent a realistic cortex. Assuming the z = 0 origin lay at the center of the sphere, the minimum z value for the solution space is z = - 3 cm. The solution space is shown in Figure 21.

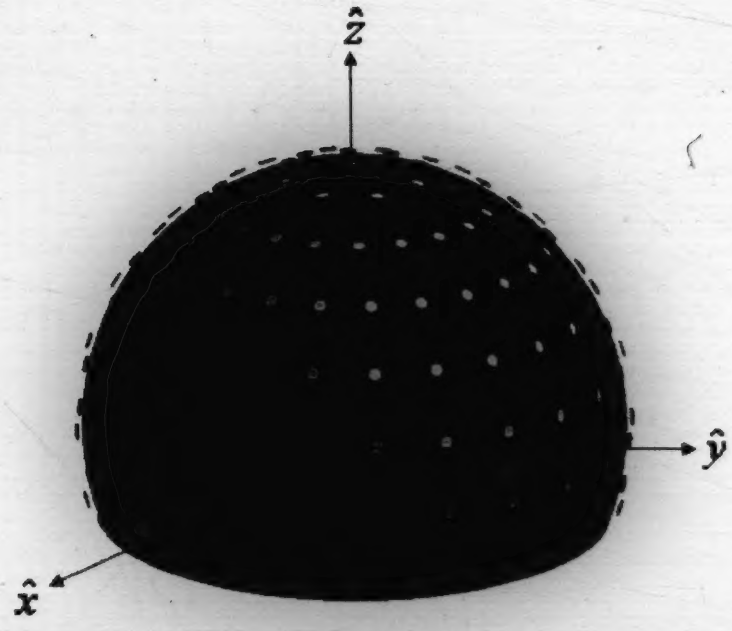

Figure 21 - Solution space for three concentric shell head model with 113 electrode configuration

4.2.4 Electrode Montage

Unlike the variation of the 10-20 electrode montage used for the realistic head measurements, the electrodes in the following simulations were evenly distributed to achieve a constant inter-electrode distance. No electrodes were positioned below the lower limit of the solution space. Therefore, the minimum possible z coordinate for any given electrode was z = -3 cm. Seven different electrode montages were examined. The number of electrodes in each montage is 17, 37, 61, 113, 149, 197, and 249. The 249 electrode montage is comparable to commercially available 256 channel Geodesic EEG System [26].

4.3 Methods

The EEG is simulated using a single 17 Hz sinusoidal dipole source of unit amplitude, oriented normally to the solution space surface. The location of the source is chosen randomly within the solution space. The scalp potentials, V(t),

are determined via the forward solution, (2.1), using the lead field matrices corresponding to the 17, 37, 61, 113, 149, 197, and 249 electrode montages. All of the lead field matrices are computed with double precision except the 249 electrode lead field matrix that is calculated with single precision due to memory constraints. The simulated EEG is sampled at 256 Hz for one second.

For each electrode configuration, Gaussian white noise is added to **V** at the electrode sites. The SNR is defined as the ratio of the sums of the eigenvalues of the signal and noise covariance matrices. For the following simulations, SNR values of 10, 5, and 2 were used in order to be consistent with the lower, middle, and upper values observed with a phantom human head [23]. In addition to simulating more realistic measurement conditions, the added noise also ensures a full rank covariance matrix, allowing matrix inversion.

The five inverse solutions are obtained using the techniques discussed earlier. For the adaptive algorithms, all 256 samples were used to define the covariance structure, **R**. A single eigenvector corresponding to the largest eigenvalue defines the signal subspace for the ES Beam and MUSIC algorithms. The regularization parameter [13], used to ensure stable inversion of the covariance matrix for the beamformers, is equal to 1% of the largest eigenvalue of **R**.

The simulation consists of 100 trials; each trial has a unique, randomly chosen source location. For each trial, the forward and inverse solutions were determined using the 17, 37, 61, 113, 149, 197, and 249 electrode montages.

4.4 Results

For the four underdetermined algorithms (ES Beam, BK Beam, MN, and LORETA), the localization error is defined as the straight line distance from the actual source location to the global maximum of the inverse solution. The localization error for MUSIC is the straight line distance between the actual source location and the location of probability density function maximum.

The localization errors for each algorithm, for the various electrode montages, with SNRs of 10, 5, and 2, are shown in Figures 22 - 26. Results are expressed as the mean for the 100 trials.

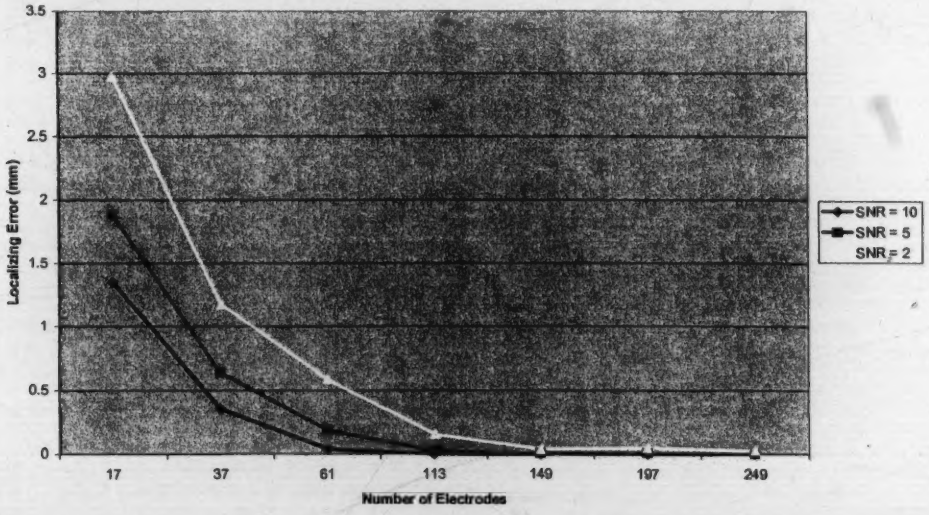

Figure 22 – Localization error with eigenspace projection beamformer for multiple electrode configurations

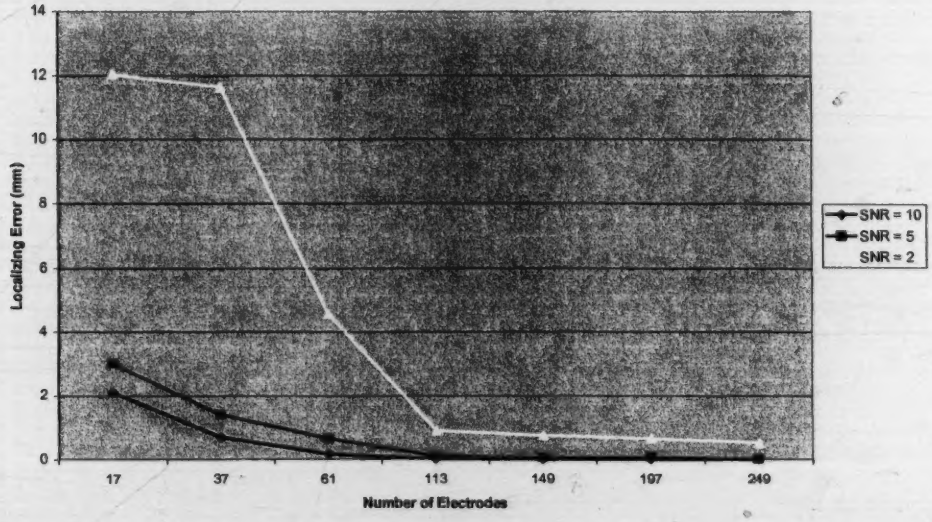

Figure 23 – Localization error with Borgiotti-Kaplan beamformer for multiple electrode configurations

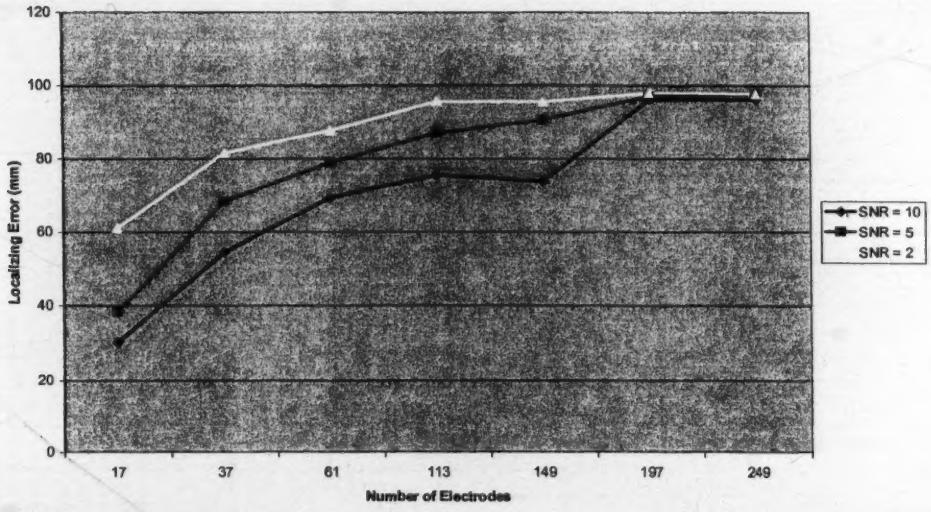

Figure 24 – Localization error with minimum norm for multiple electrode configurations

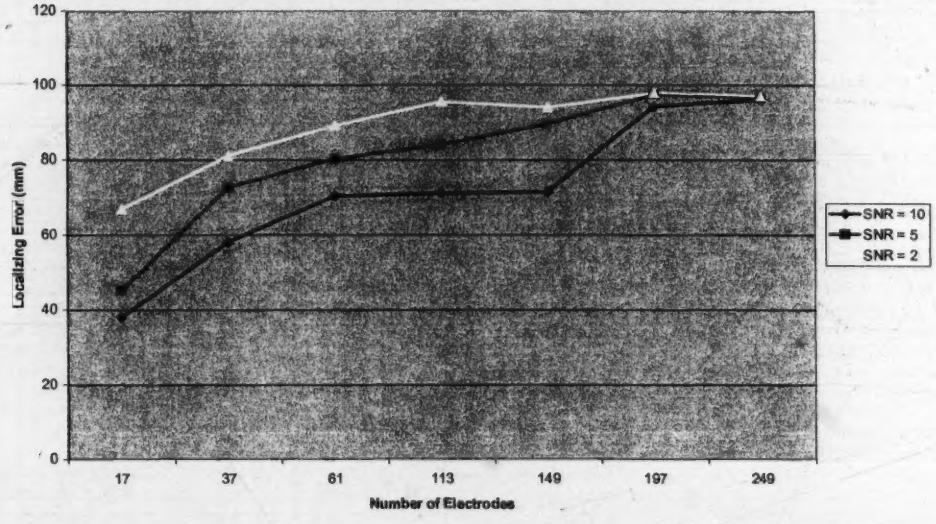

Figure 25 – Localization error with LORETA for multiple electrode configurations

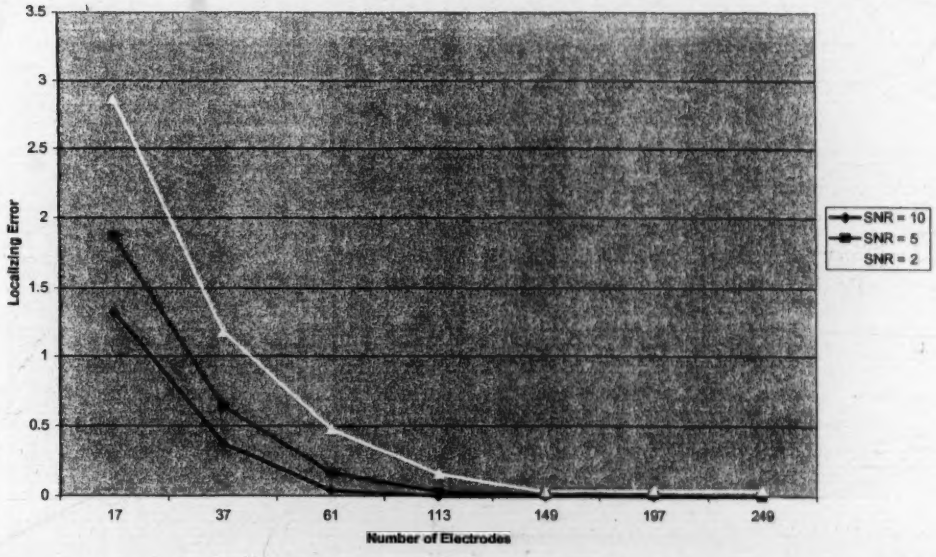

Figure 26 – Localization error with MUSIC for multiple electrode configurations

The dispersions, (3.2), are also calculated for the seven electrode montages for the four underdetermined inverse algorithms. The dispersions for each algorithm, with the various electrode montages, with SNRs of 10, 5, and 2, are shown in Figures 27 - 30. Results are expressed as the mean for 100 trials.

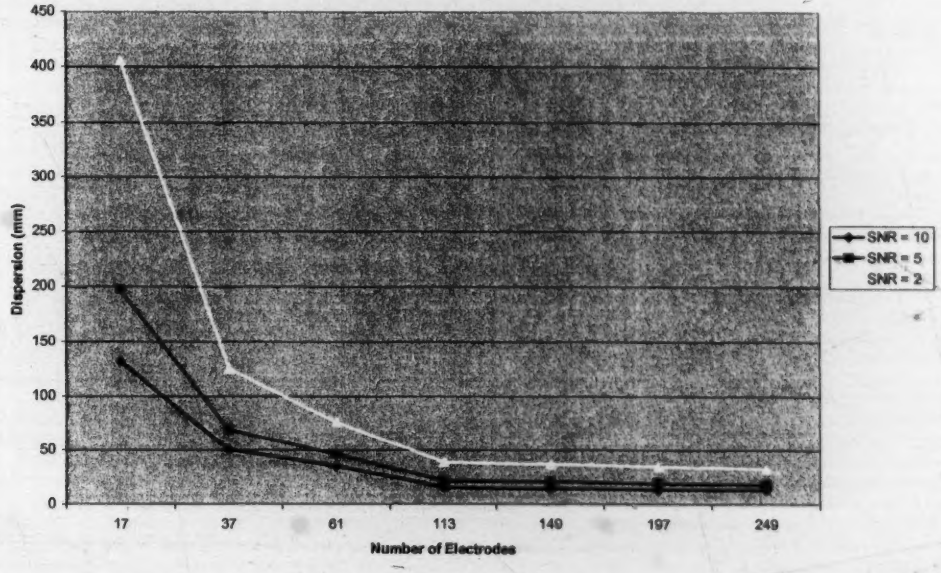

Figure 27 – Dispersions for multiple electrode configurations using eigenspace projection beamformer

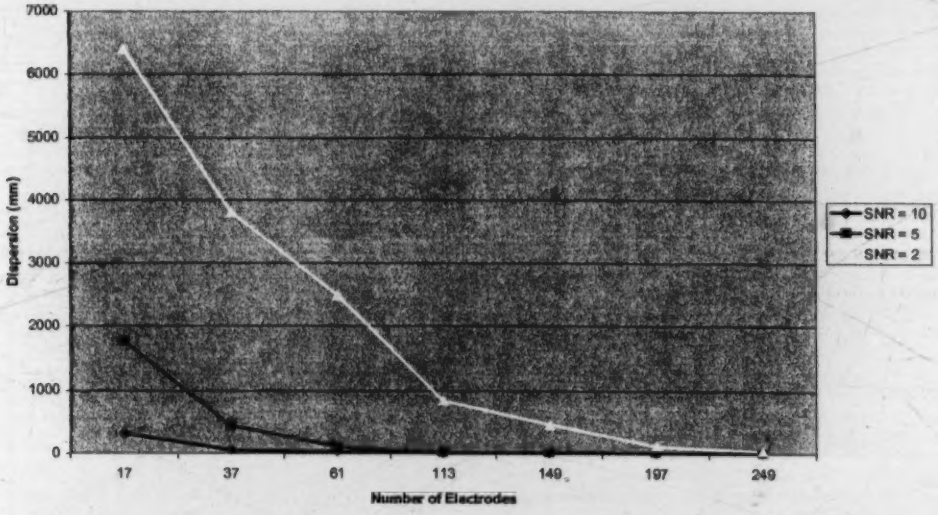

Figure 28 – Dispersions for multiple electrode configurations using Borgiotti-Kaplan beamformer

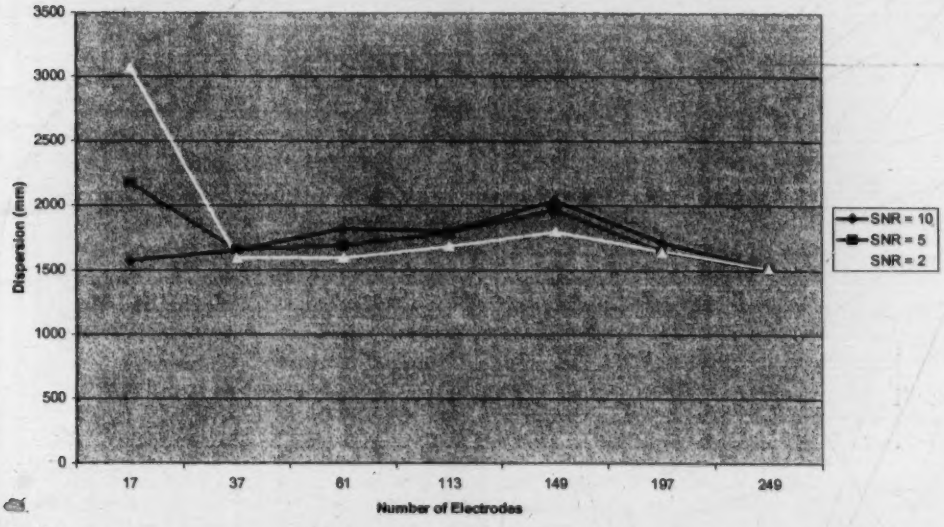

Figure 29 – Dispersions for multiple electrode configurations using minimum norm

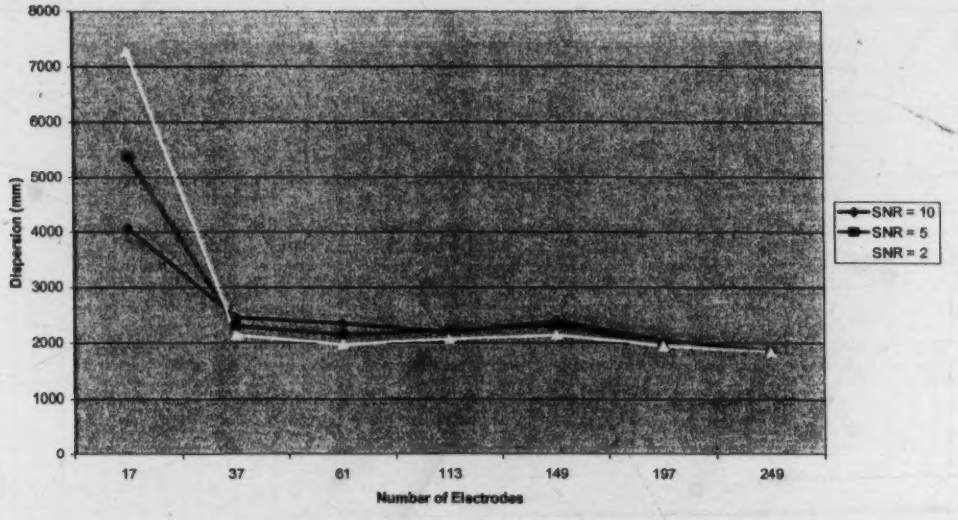

Figure 30 – Dispersions for multiple electrode configurations using LORETA

Consistent with previous single source localizing experiments, the adaptive algorithms yield smaller localization error and dispersions compared the non-adaptive algorithms. Compared to BK Beam, the two signal subspace based algorithms, ES Beam and MUSIC, exhibit superior localizing capabilities. In addition, the adaptive algorithms experience reduced localization error and dispersion as the number of electrodes increases.

The localization error data also suggests that increasing the number of electrodes reduces the effect of noise. Large discrepancies in localization error due to varying SNR exist for the adaptive inverse solutions for the sparse electrode configurations. As the number of electrodes exceeds 149, the adaptive inverse algorithms produce similar localization errors and dispersions regardless of the SNR. Therefore, we conclude that increasing the number of electrodes reduces the effect of uncorrelated noise for the adaptive inverse algorithms.

The performance of the non-adaptive algorithms with respect to an increasing electrode density produced counter intuitive results. Both MN and LORETA suffered increasing localization errors as the number of electrodes increased. MN and LORETA exhibit substantially greater localization errors for

all electrode and noise combinations than the three adaptive algorithms. With an increasing number of electrodes, the MN and LORETA localization errors increased until a relative plateau is reached with 197 electrodes. The minimum localization errors for MN and LORETA were 30.27 mm and 37.94 mm respectively and occurred with only 17 electrodes. On the other hand, minimum localization errors for ES Beam, BK Beam, and MUSIC were substantially lower with values of 0.00 mm, 0.01 mm, and 0.00 mm respectively and occurred when electrode density was at its highest level with 249 electrodes.

MN and LORETA localization errors become less dependent on the SNR as the number of electrodes increases (minimal difference observed with 249 electrodes), unfortunately, the errors are too large ~ (95 mm → 98 mm) to be of any use in a clinical environment.

The dispersions of the non-adaptive solutions follow more intuitive decreasing trends with respect to increasing electrode density. This result is similar to the behavior of the adaptive algorithms under similar conditions.

4.5 Discussion

Reasons for the poor localizing ability of the non-adaptive algorithms are discussed in Chapter 3. A major conclusion drawn from the previous single source simulations is that the electrode configuration biases the estimated maxima towards regions of greater electrode density in order to minimize the overall energy. By decreasing the inter-electrode distance while maintaining a regular configuration, we hoped to reduce the severity of bias exerted by the electrodes. Unfortunately, the simulations contradicted the hypothesis, indicating that other faults must exist within the MN and LORETA inverse algorithms.

Since the lead field matrix was derived analytically and used for the both the adequately performing adaptive algorithms and the poorly performing non-adaptive algorithms, its accuracy cannot be responsible for skewing the results. Instead the errors must reside in the derivation of the pseudo inverse, **T**, (2.9) and (2.11). As the number of electrodes increase, **T** increases proportionately. The

size of **T** is $(N \times 3 \cdot M)$ where N is the number of electrodes and M is the number of dipoles within the solution space. Therefore, each additional electrode adds an additional (3 · 51 741) = 155 223 entries to **T**. Assuming there are small inaccuracies in the derivation of **T**, each additional electrode will contribute a substantial number of spurious entries that will propagate throughout the estimated inverse solution. Therefore, the electrode bias witnessed in Chapter 3 is only responsible for a portion of the MN and LORETA localization errors. A more accurate pseudo inverse is required to further reduce the localization error.

Another factor to consider when altering the electrode density is the effect on electrode sensitivity. Electrode sensitivity is affected by the locations of the electrodes as well as the conductive properties of the head model [27]. In order to determine the sensitivity of a given electrode pair, we must examine the "reciprocity theorem" which states that "the knowledge of the current density (or electric field) throughout a volume conductor caused by an *injection* of current between two (stimulating) electrodes completely specifies how these same electrodes, when serving as recording electrodes, pick up the potentials caused by dipole sources at any place in the volume conductor [27]."

Consider two electrodes positioned on the scalp that are connected by an external voltage source (stimulating mode): current flows through the conductive head model from one electrode to the other. The current density at any location within the head model depends on the anisotropic and inhomogeneous properties of the various tissue types. The sensitivity of an electrode pair (measurement mode) to an electric dipole source located at any point in the head model is proportional to the current density at the same location if the electrode pair was operating in a stimulating mode. More specifically, the direction of the sensitivity is equal to the negative gradient of the induced electric field [2].

Due to the highly resistive barrier of the skull, a substantial portion of the current will flow from the "source" electrode through the scalp to the "sink" electrode without penetrating the skull or brain. The closer the source and the sink are to one another, the less resistive the scalp current pathway becomes.

Therefore, even less of the injected current penetrates the brain and the internal sensitivity decreases. In fact, the greatest sensitivity for an electric dipole source located deep within the brain occurs when the source and sink electrodes are positioned on opposite sides of the head. Unfortunately, such a sparse configuration does not provide enough information for accurate source localization.

In the simulations detailed above, the head model consisted of three concentric spheres of constant radii with dipole sources located on the equivalent cortical surface. Therefore, our results are not skewed by the affect of decreasing sensitivity with respect to source depth. The same assumptions cannot be made for realistic head models where the solution space is not always equidistant from the EEG montage.

At first glance, increasing the electrode density initially appears to be a viable solution to reducing the bias associated with inverse source localization algorithms, but upon further investigation, this is not the case for all of the investigated algorithms. Increasing the number of electrodes has a definite advantage in reducing the localization error and dispersion for the ES Beam, BK Beam, and MUSIC algorithms. A more electrode dense EEG measurement configuration also helps reduce the effects of noise, especially in the signal subspace dependent solutions (ES Beam and MUSIC). These advantages are partially offset by the increase in computation time and memory requirements for both the derivation of the lead field matrix and the calculation of the beamforming weighting vectors. Also, electrode sensitivity suffers as inter electrode distances decrease making deeper sources less visible at the electrodes. A delicate balance with respect to electrode density must exist that maximizes electrode sensitivity and computational efficiency while providing adequate spatial source information required for accurate source localization. On the other hand, simulations showed that additional electrodes had a negative effect on the localization error of the non-adaptive algorithms. This leads us to believe that the pseudo inverses, **T**,

contain inaccuracies that propagate as **T** grows in size in proportion with the number of electrodes.

Chapter 5 - Localization of Real EEG Data

5.1 Introduction

Previous simulations in Chapters 3 and 4 involved the localization of a single stationary source with the remainder of the solution space electrically inactive. From these simulations, we concluded that the adaptive inverse solutions (BK Beam, ES Beam, and MUSIC) are the most accurate in localizing a single source. ES Beam and MUSIC make use of signal subspace projection to further improve their localizing capabilities while reducing the effects of noise. Although ES Beam and MUSIC perform better than the other three investigated algorithms (MN, LORETA, and BK Beam), they require the à priori knowledge with respect to the number of sources underlying the EEG. This knowledge may not be present when analyzing real EEG data. ES Beam and MUSIC also assume that the eigenvectors corresponding to the greatest source of power coincide with epileptic activity.

Inter-ictal EEG data collected from an epileptic patient will be used to test the performance of the five inverse algorithms. In previous simulations, the location of the electric dipole source was known and the effectiveness of the various inverse solutions could easily be quantified by comparing the characteristics of the inverse solution with the known source characteristics. For the clinically obtained EEG data, the location, magnitude, and orientation of the actual source(s) are unknown, making it difficult to assess the performance of each algorithm. Instead, the quality of the inverse solutions will be assessed by splicing together consecutive inverse solution images into a video and assessing the physiological probability of the observed seizure propagation. From the various videos, we will look for consistent areas of focused electrical activity that could represent an epiletogenic zone.

Another fault that has affected the performance of all five algorithms in previous simulated results is the accuracy of the lead field matrix. During the

simulation of the EEG, the lead field matrix used to simulate the EEG in the forward solution is identical to the lead field matrix used to calculate the inverse solution. Using clinical EEG data, instead of simulated EEG data, will introduce an additional source of error due to the differences between the estimated discretized lead field matrix and the actual continuous conductivities linking the cortex to the scalp. The differences between estimated and actual lead field matrices will affect the performance of all five source localizing inverse algorithms. The erroneous effects of differing lead field matrices for the beamforming algorithms are detailed in [16].

In addition to examining the performance of the five aforementioned inverse solutions, adaptations of the ES Beam and MUSIC that further define the signal subspace will also be considered. Principal component analysis (PCA) and temporal independent component analysis (ICA) will be performed on the EEG data matrix to extract the time series that are characteristic of epileptic activity. Both PCA and ICA have the potential to extract the epileptic subspace from the EEG data to improve upon epileptic source localization. The varimax algorithm will be used to rotate the vectors spanning the signal subspace in order to concentrate the signal variance over a minimum number of electrodes.

5.2 Background Information

As seen in previous chapters, projecting the derived weights onto the signal subspace improves the performance of the beamformer. In addition, correctly predicting the signal subspace also improves the performance of MUSIC. The process of determining the signal subspace can be achieved through various rotations and factoring techniques such as: principal component analysis [28], independent component analysis [29], and the varimax rotation [30].

The EEG potentials, **V**, can be factored into spatial and temporal components.

$$\mathbf{V} = \mathbf{XY} \tag{5.1}$$

In (5.1), the columns of **X** are the spatial components while the rows of **Y** are the temporal components. Each temporal component defines how a single component fluctuates over time while the corresponding column vector of **X** is a series of electrode loadings that describes how the temporal component is distributed over the scalp. Select columns of **X** can be used to define the signal and noise subspaces. Subsequent subsections outline different techniques for performing the factorization in (5.1).

5.2.1 Principal Component Analysis

Principal component analysis (PCA) utilizes singular value decomposition (SVD) to factorize the EEG data into three matrices:

$$\mathbf{V} = \mathbf{U}\mathbf{S}\mathbf{W}^T \tag{5.2}$$

In (5.2), **U** is a N x N (N = the number of electrodes) matrix of orthogonal column eigenvectors. **W** is a T x T (T = number of data samples) matrix; each column of **W** has unit variance and describes how each component varies over time. Only the first N columns of **W** are of interest (N is the rank of **W**). **S** is a N x T diagonal matrix of singular values defining the rms value of each temporal component [28].

It is more computationally efficient to calculate the temporal components via eigenvalue decomposition of the square, symmetric covariance matrix, **R** (2.15).

$$\mathbf{R} = \mathbf{U}\lambda\mathbf{U}^T \tag{5.3}$$

The eigenvectors of **R** are the same as the eigenvectors of **V** and the eigenvalues, λ, of **R** are the squares of the singular values of **V**. Therefore, the temporal components can be obtained via:

$$\mathbf{W}^T = \lambda^{-1/2}\mathbf{U}^T\mathbf{V} \tag{5.4}$$

The first N temporal components are visually inspected in search of components resembling epileptic waveforms. Ideally, a small number of the components would exhibit the typical epileptic "spike and wave" waveform. The eigenvectors

corresponding to the epileptic waveforms can be used to define the signal subspace needed for the eigenspace projection beamformer as well as MUSIC.

PCA can also extract epileptic components from an EEG that can be used to localize epileptic sources using non-adaptive techniques like MN and LORETA. In this case, only the temporal components resembling epileptic waveforms are included in the reconstruction of the epileptic EEG (5.2) while the remaining components are set to zero. This would reduce the contributions from non-epileptic sources.

PCA differs slightly from the eigenspace projection algorithm because it no longer assumes that the high power components are epileptic in nature. It may be erroneous to assume that the component(s) with the most power are epileptic and not due to other neurological activity. Visually inspecting each component generates a greater understanding of the underlying sources and provides insight into the number of possible epileptic sources.

5.2.2 Independent Component Analysis

Independent component analysis is an alternative technique for performing the decomposition in (5.1). The EEG is assumed to be the result of linear mixing of the underlying electrical activity within the brain. Temporal independent component analysis (ICA) extracts the time series of the underlying sources as well as the weightings that govern signal mixing at the electrodes. The ICA model is identical to the model in (5.1).

V is a N x T matrix of scalp potentials. N is equal to the number of electrodes and T is the number of data samples. Matrix **Y** is also a N x T matrix representing the statistically independent, unit variance time series of N sources that generate the EEG. **X** is N x N matrix of "mixing coefficients' that determine the degree of influence each time series has at each electrode site. The ICA model assumes that the number of independent sources does not exceed the number of electrodes. Firstly, the ICA algorithm applies PCA in order to reduce

the dimensionality of **V** so that only the waveforms contributing significant portions of the overall EEG power are considered.

The central limit theorem[3] is the underlying principle that enables the extraction of the independent components: a single independent component of **V** will be less Gaussian than the sum of the independent components that constitute **V**. Gaussianity is measured using combinations of kurtosis and negentropy [29]. Each independent component has a corresponding vector that can be normalized to define the signal subspace necessary for the implementation of ES Beam and MUSIC. Like PCA, ICA allows us to localize and visualize sources corresponding to a given waveform while nulling the contributions from other waveforms. Unlike PCA, the column vectors of **X** are not constrained to be orthogonal to one another.

The i^{th} independent time component can be projected into the N electrode head space, forming a single rank EEG via:

$$\mathbf{V}_{ICA}^{i} = \mathbf{X}(:,i)\mathbf{Y}(i,:) \tag{5.5}$$

5.2.3 Varimax Rotation

Varimax is a subspace rotating algorithm that redistributes the loadings of a set of eigenvectors, **X**, so that the loadings are concentrated over a smaller number of electrodes [30]. This is achieved by maximizing the variance of the vectors. The varimax rotation reduces the complexity of the EEG interpretation because it assumes that a small group of electrodes are largely responsible for detecting each principal component. The loadings of the electrodes that do not account for large variation are redistributed via rotation onto the electrodes accounting for the

---

[3] The central limit theorem states that the probability distribution function of a sum of independent random variables with arbitrary distributions, approaches a Gaussian distribution as the number of variables increases [34].

majority of component variation. The rotated vectors remain orthogonal to one another during the varimax rotation and the subspace spanned by the vector set does not change with rotation. The larger the dimensionality of the original subspace, the more electrode specific the rotated electrode loadings become. For example, a 29 dimensional subspace can be rotated so that only one electrode is weighted while the remaining 28 electrode weightings are set to zero. Conversely, the varimax rotation will have no effect on a one dimensional subspace.

5.3 Methods

5.3.1 Head Model and Solution Space

The details regarding the head model and solution space are identical to those mentioned in Chapter 3 for the realistic head simulations. To summarize, the head model was segmented from NMR images and contains 7 tissue types (cerebellum and pons, cortical grey matter, ventricles and cerebrospinal fluid, white matter, non-cortical grey matter, skull, scalp, and cerebrospinal fluid that surrounds the cortex) of varying isotropic resistivities. The resistivities are listed in Table II. The solution space consisted of a single layer of cortex composed of 61 041 voxels with 1 mm^3 resolution located along the white matter – grey matter boundary.

5.3.2 Electrode Montage

The EEG data is collected using 30 electrodes. The C_Z electrode is designated the common ground. Eighteen electrodes follow the 10-20 electrode configuration and an additional eleven electrodes were concentrated around the frontal region of the scalp because this is the region where the clinicians suspected the origin of the epileptic activity. The locations of the 29 measurement electrodes and the ground electrode are shown in Figure 31.

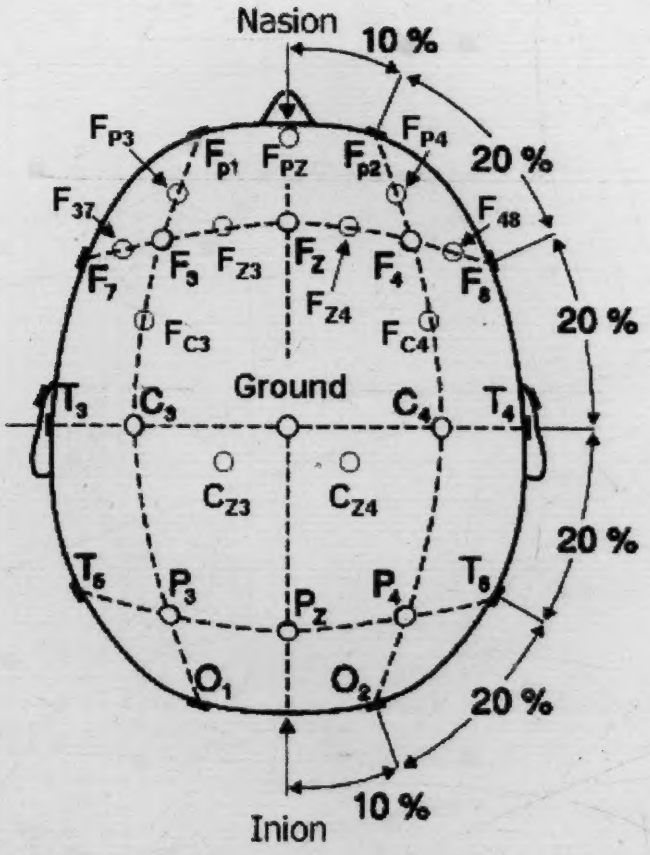

Figure 31 – Location of 30 electrodes

5.3.3 Lead Field Matrix

The lead field vectors for each orthogonal direction of every solution space voxel are solved for using the reciprocity theorem outlined in [10]. A thorough explanation of the lead field matrix derivation may be found in Chapter 2.

5.3.4 EEG Data

Real EEG data was obtained from the University of Alberta hospital for a female patient in her mid to late twenties. Clinicians diagnosed the patient with right frontal lobe epilepsy. The localization results of the five aforementioned

algorithms will be evaluated based on their ability to localize an epiletogenic zone consistent with the region hypothesized by clinicians.

The available EEG consists of 3 seconds of data sampled at 256 Hz yielding 772 samples. The EEG data is band-pass filtered with lower and upper corner frequencies of 1 and 20 Hz respectively. The filter reduces the high frequency noise and removes any DC offset from the EEG. The 772 sample EEG is shown in Figure 32.

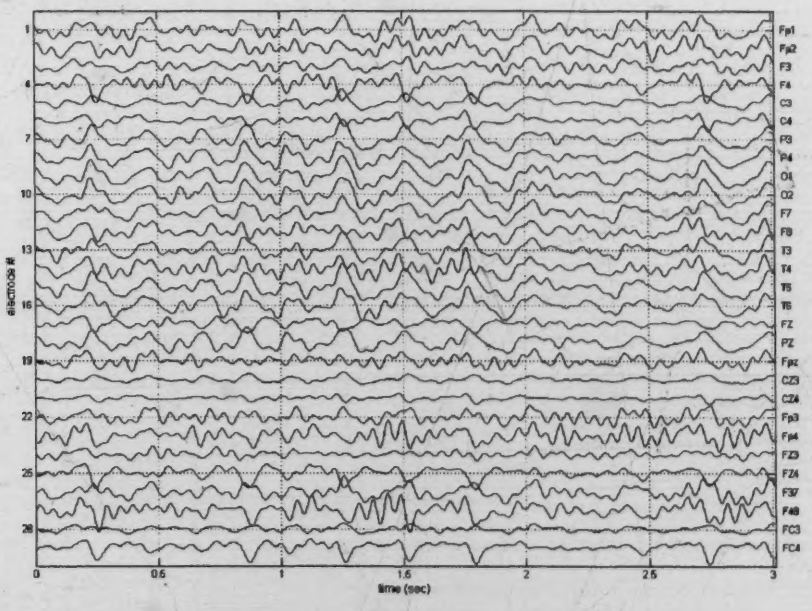

Figure 32 – 772 sample, 29 electrode EEG

The beamforming weighting vectors are derived from the inverted EEG data covariance matrix. Therefore, the covariance matrix must remain full-rank. The non-adaptive algorithms do not require a full rank data set, so the EEG can be further filtered via rank reduction. Projecting the EEG data onto the most "powerful" or "active" eigenvectors of **V**, can theoretically isolate the EEG subspace associated with epileptiform activity while eliminating the less "powerful" background/noise components of the EEG. The projection is obtained from:

$$\mathbf{V}_{\text{epileptiform}} = \mathbf{U}(:,1:Q)\mathbf{U}(:,1:Q)^T\mathbf{V} \tag{5.6}$$

U(:,1:Q) denotes the first Q eigenvectors of **V** arranged in columnar form. Q is the dimensionality of the ictal signal subspace and is determined by examining the magnitudes of the eigenvalues of **R**. If an eigenvalue is large, the corresponding eigenvector is included in the epileptiform activity subspace. The normalized eigenvalues are shown in Figure 33.

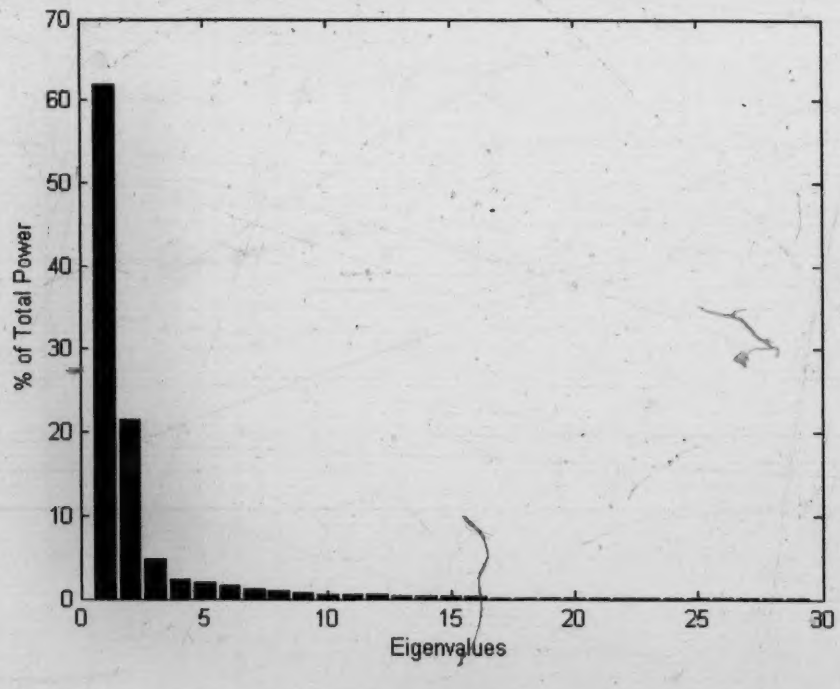

Figure 33 - Eigenvalues of the EEG and the percentage of power represented in each dimension

The eigenvalues show that 83.4% of the total power resides in the first two components and 88.2% in the first three components, suggesting two or three underlying sources. The filtering technique in (5.6) is used with a three dimensional signal subspace to improve the localizing capabilities of the non-adaptive MN and LORETA algorithms.

5.3.5 Data Window for the Covariance Matrix

As noted in Chapter 3, the larger the number of samples used to compute the covariance matrix, the more accurate the localizing capabilities of the adaptive inverse algorithms. This generalization assumes that the source is stationary and unfortunately, this assumption may not be valid for real data. When the size of the window is small, the beamformer weightings change rapidly resulting in a "flashing" video representation. To ensure some temporal stability, 257 samples were used to calculate **R** with 128 points on either side of the time slice of interest.

5.3.6 Temporal Smoothing

When consecutive instantaneous solutions are catenated together, unintuitive "flashing" video clips resulted. In order to obtain a continuous video of source activity, temporal smoothing was applied to the EEG data.

For the non-adaptive inverse algorithms, an instantaneous inverse solution is:

$$\hat{\mathbf{j}}(t) = \mathbf{T}\mathbf{v}(t) \tag{5.7}$$

Given that we are only interested in the magnitude of the distributed dipoles at each voxel location, we can display the power, **s**(t), associated with the estimated current density:

$$\mathbf{s}(t) = diag\left(\mathbf{T}\mathbf{R}(t)\mathbf{T}^{T}\right) \tag{5.8}$$

Where $\mathbf{R}(t)$ denotes the covariance structure of a small window of data centered about the time slice in question. **R**(t) is defined by:

$$\mathbf{R}(t) = \frac{\mathbf{V}\left(:, t-\frac{w}{2} : t+\frac{w}{2}\right)\mathbf{V}\left(:, t-\frac{w}{2} : t+\frac{w}{2}\right)^{T}}{N(w+1)} \tag{5.9}$$

The width of the smoothing window is defined by w and N is the number of electrodes. Increasing w will create a more temporally smooth inverse solution. The temporal smoothing window was 11 points long

In a similar manner, the instantaneous inverse solution for a voxel located at $\mathbf{r}$ with orientation $\boldsymbol{\eta}$ using one of the beamforming techniques is:

$$\hat{\mathbf{j}}(\mathbf{r},\eta,t) = \mathbf{w}^T(\mathbf{r},\eta,t)\mathbf{v}(t) \tag{5.10}$$

To apply temporal smoothing, the power at each voxel location, $\mathbf{s}(\mathbf{r},\eta,t)$, is displayed using the smoothing window covariance structure (5.9) instead of the instantaneous potentials:

$$\mathbf{s}(\mathbf{r},\eta,t) = \mathbf{w}^T(\mathbf{r},\eta,t)\mathbf{R}(t)\mathbf{w}(\mathbf{r},\eta,t) \tag{5.11}$$

Because there is no need to invert the covariance matrices in (5.8) or (5.11), the temporal smoothing covariance matrix may be decreased in rank and tailored to include only the component(s) of interest.

5.4 Results

Video clips consisting of 772 frames were made using the traditional methods (MN, LORETA, BK Beam, ES Beam, and MUSIC) as well as more advanced subspace projection techniques utilizing PCA, ICA, and the varimax rotation. In order to describe each algorithms performance, a common frame from each video is shown with additional details added when necessary. The 63rd slice is chosen because it contains a well-defined peak, flanked by periods of reduced activity in both directions. These conditions should yield optimal localization results. The blue vertical line on the EEG indicates the 63rd slice.

5.4.1 Localization Results Using Traditional Methods

5.4.1.1 MN and LORETA

The pseudo inverses, **T**, were calculated using the MN and LORETA algorithms. The EEG was projected onto three eigenvectors, accounting for 88.2% of the total power of the EEG.

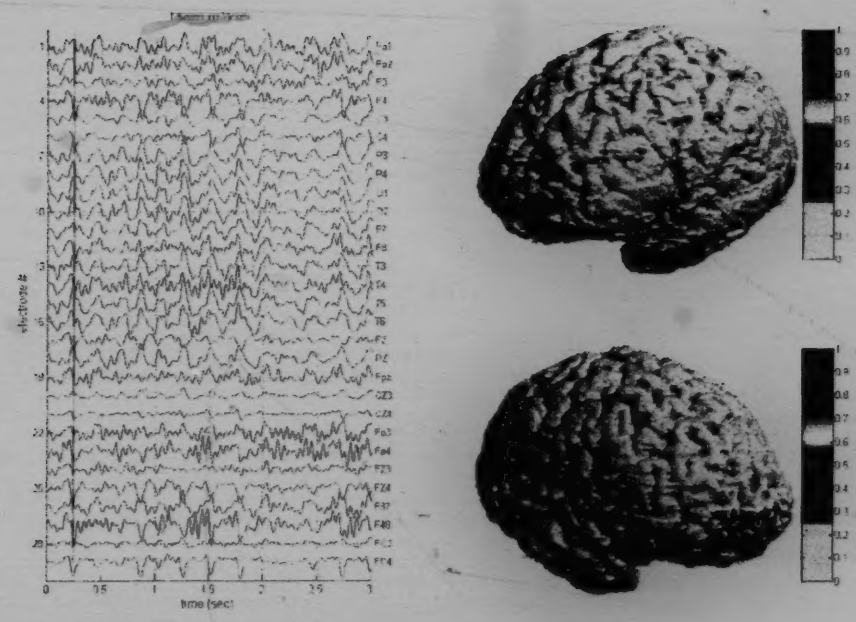

Figure 34 – Minimum norm inverse solution

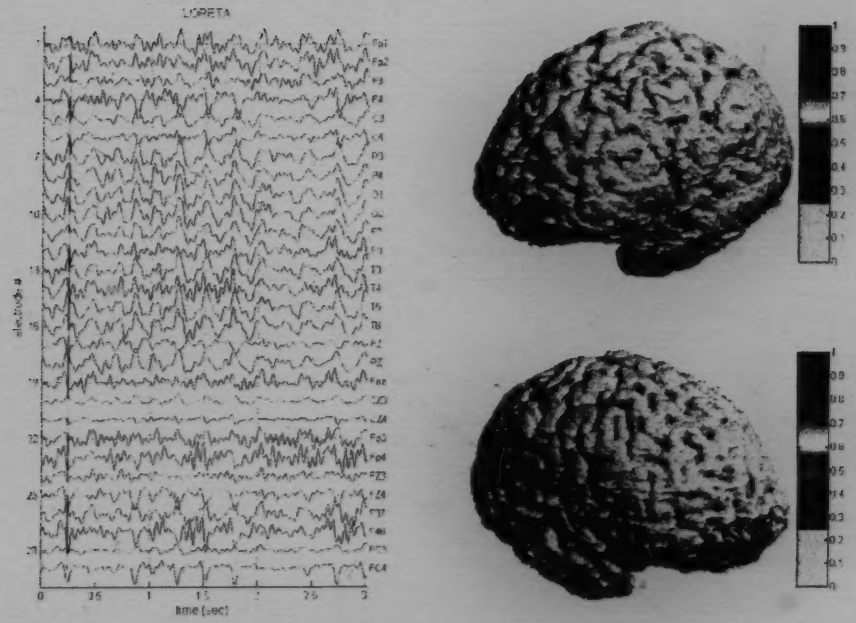

Figure 35 – LORETA inverse solution

5.4.1.2 Borgiotti-Kaplan and Eigenspace Projection Beamformers

The BK and ES Beam algorithms were applied to the same EEG. A moving data window of 257 samples is used to define the covariance matrix needed to calculate the beamforming weights. For the ES Beam, the weights are projected onto the signal subspace defined by the first three eigenvectors of the 257 sample, full rank data covariance matrix. The 11 data samples used to compute the temporal smoothing covariance matrix are also projected onto the same three dimensional subspace. Neither of the subspace projections are implemented for the BK Beam.

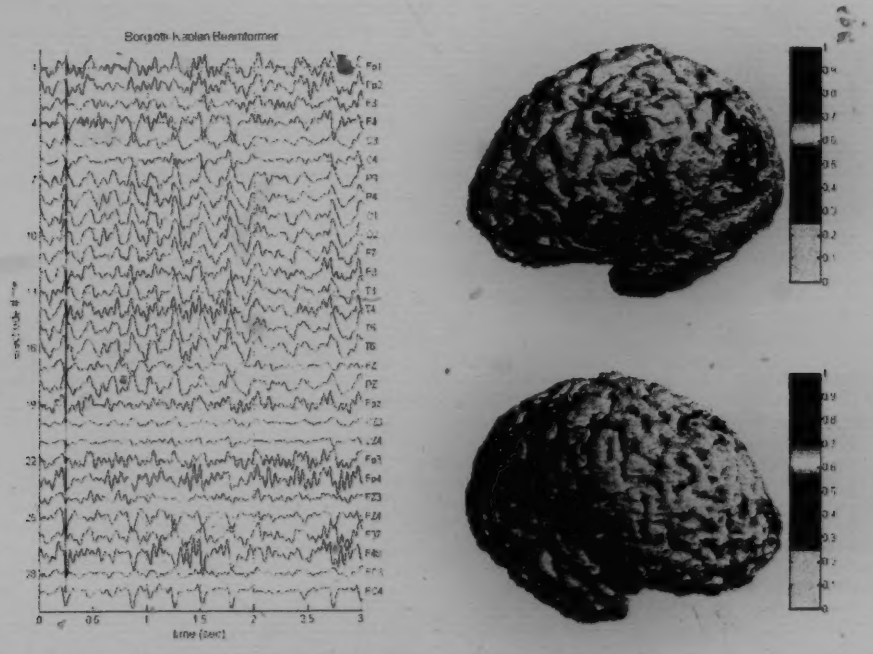

Figure 36 – Borgiotti-Kaplan beamformer

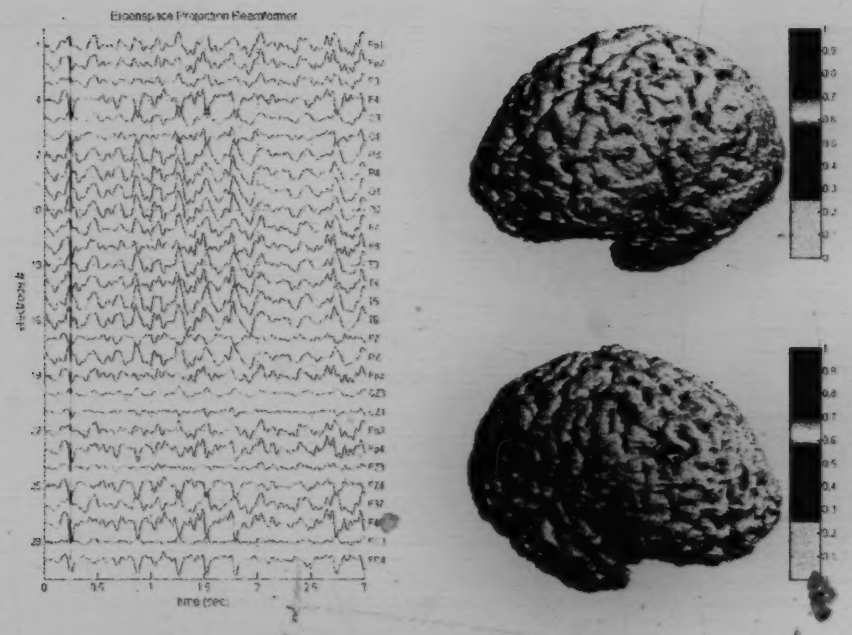

Figure 37 – Eigenspace projection beamformer

5.4.1.3 Multiple Signal Classification

The inverse solution at n = 63 is calculated using the MUSIC algorithm. From looking at the magnitudes of the eigenvalues in Figure 33, it was decided that three dipoles should be fitted into the solution space. The data covariance matrix used to define the signal and noise subspaces for the MUSIC algorithm is identical to the one used to calculate the weights for BK and ES Beam.

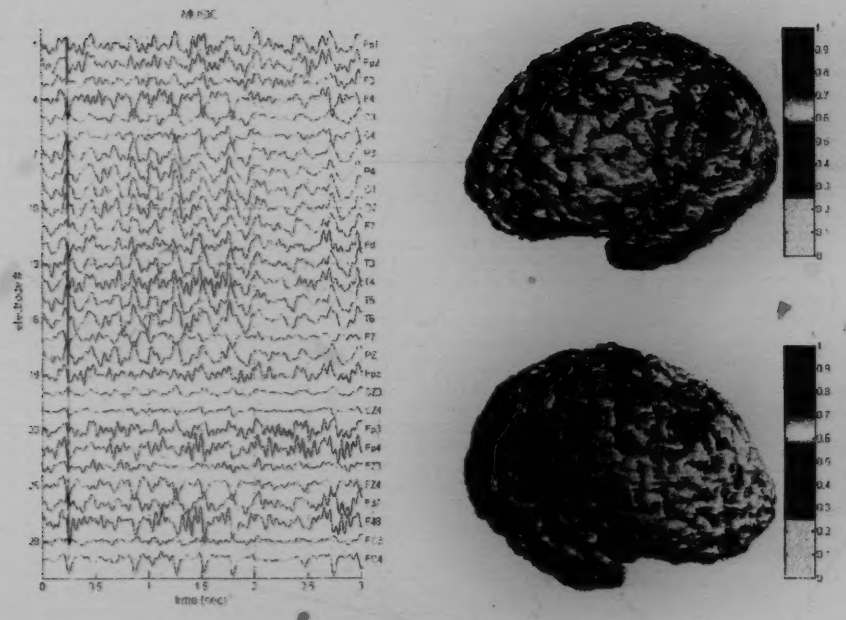

Figure 38 – MUSIC Inverse Solution

5.4.1.4 Summary of Traditional Methods

The MN and LORETA solutions are very similar to one another and are concentrated about the front of the frontal lobe. Both solutions show more electrical activity on the right hand side of the head. This is expected due to the asymmetrical characteristics of the EEG. For example, large fluctuations are observed at electrodes F4 and FC4 compared to their symmetrical counterparts F3 and FC3. It is possible that these two inverse solutions are biased towards the frontal lobe because of the increase in electrode density at the frontal region of the scalp (see Figure 31).

The inverse solution for the BK Beam fluctuated rapidly and covered areas on both sides of the temporal lobe. During the second and third second of data, the activity spread to the central and left regions of the frontal lobe. The BK Beam results were very difficult to interpret and do not provide a high level of confidence. Although, the sharp focus seen in ES Beam was evident in many of

the BK Beam inverse solutions, the BK Beam solution appeared to be more easily corrupted by noise.

In previous chapters, the BK Beam algorithm incorporated a regularization parameter in order to invert the data covariance matrix. This was necessary because the covariance matrix was not necessarily full rank despite the added white noise. Unfortunately, the regularization parameter is equivalent to adding additional white noise to the EEG data [13]. From looking at the eigenvalues in Figure 33 it appears that all 29 eigenvalues are large enough that a regularization parameter is unnecessary, but a regularized solution was computed regardless. The BK Beam inverse solution produced with the regularization parameter was even more variable than the non-regularized video. This result reinforces just how susceptible the BK Beam is to added noise.

The ES Beam video has quite a focused and relatively stationary peak located at the same position as the frontal lobe maximum in Figure 37. During the second half of the data, the focus begins to shift towards the central portion of the frontal lobe with brief pulses of activity on the left hand side during the third second of data. Of all the algorithms, ES Beam produces the most focused source location and appears to agree with the observed EEG data set. Since 88% of the EEG power is accounted for in the three dimensional subspace, it is fair to conclude that the drastic reduction in dispersion is not a result of excessive data filtering.

Without a known source location, it is difficult to determine which location (MN/LORETA, ES Beam, or either) is the correct location of the epileptic focus. The clinicians treating the patient diagnosed the epileptogenic zone to a region resembling the focus obtained with ES Beam. Their expert opinion in conjunction with the excellent performance of ES Beam in previous chapters biases our suspicions towards the ES Beam result.

The source location probability density function associated with MUSIC is quite broad covering both the right temporal lobe and the aft portions of the frontal lobe. The MUSIC algorithm was repeated with both one and two

hypothesized sources with very similar results. Also, the number of samples used to estimate the signal and noise subspaces was varied with only slight differences in the results. Like the four other algorithms, MUSIC shows a right side dominant solution that is expected based on the observed EEG.

Sixteen consecutive frames of the LORETA and ES Beam inverse solution are shown in Figures 40 and 41 to illustrate how the electrical activity propagates throughout the head during an inter-ictal spike. Only the right hand side of the head is shown because it contains the majority of the electrical activity. The 16 frames chosen were slices 317 – 333. This portion of the EEG lies between the two red vertical lines in Figure 39 and contains an inter-ictal spike.

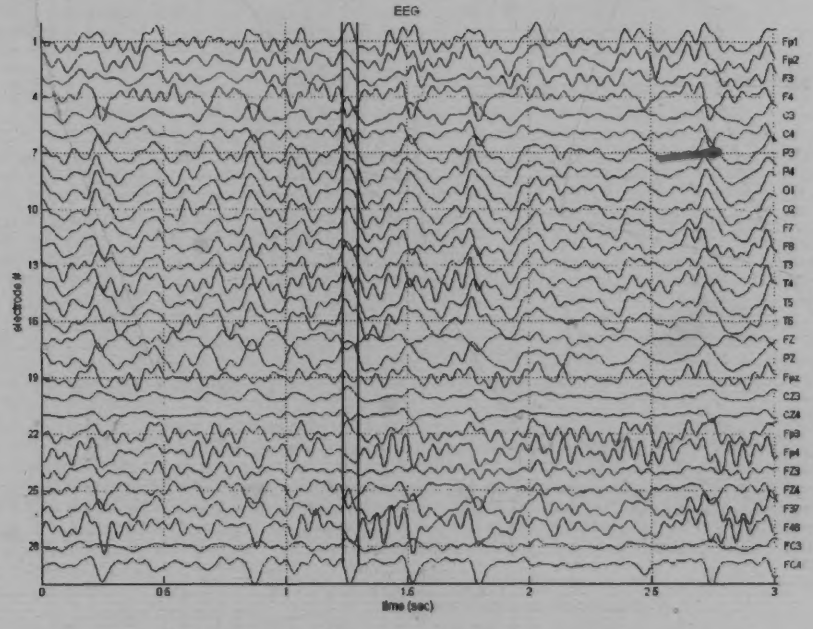

Figure 39 - Portion of EEG used in consecutive images

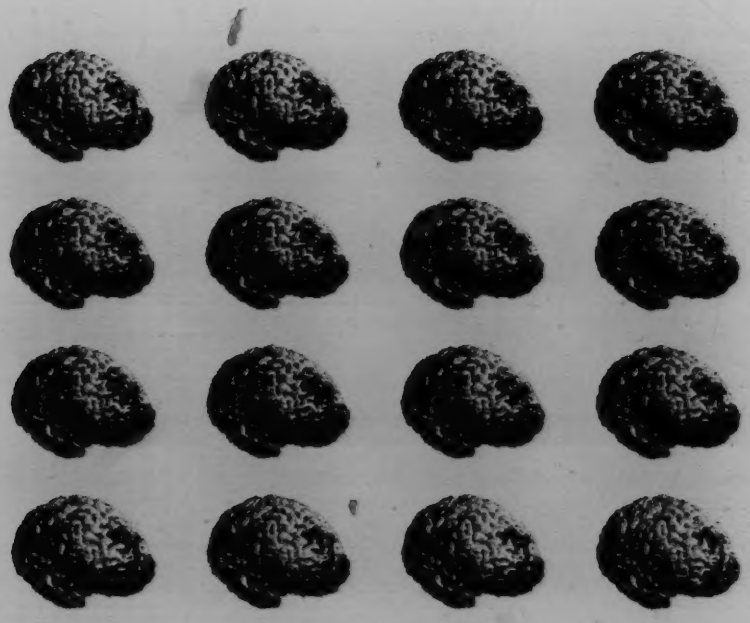

Figure 40 - LORETA consecutive inverse solutions (left to right, top to bottom)

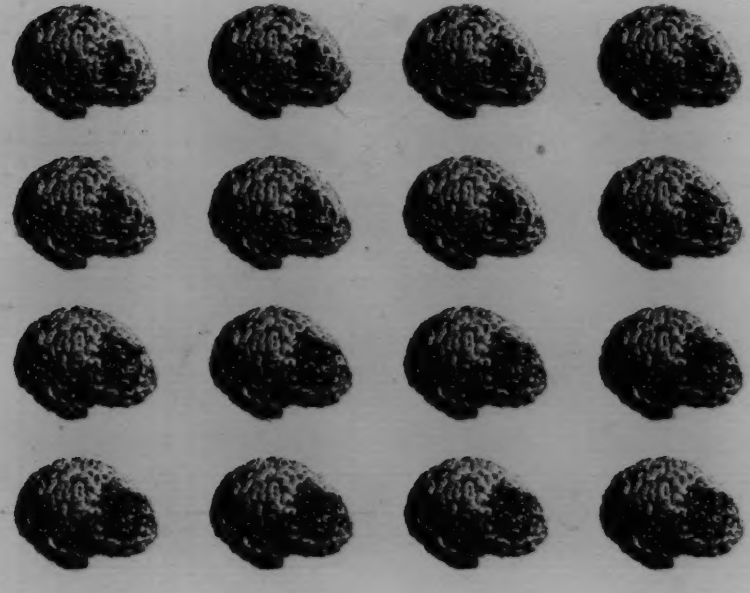

Figure 41 - ES Beam consecutive inverse solutions (left to right, top to bottom)

Figure 40 illustrates how the LORETA algorithm localizes the inverse solution at very front of the frontal lobe with greater electrical activity on the right hand side. As the EEG approaches the peak, the LORETA inverse solution propagates outwards and towards the right hand side of the frontal lobe. The ES Beam series shows a radial trend in signal propagation from the focus located on the right hand side of the frontal lobe.

Besides location, another difference between Figures 40 and 41 is the speed of signal propagation. Both inverse solutions experience equal temporal smoothing, but the LORETA inverse solution is already receding by the 16^{th} frame while the ES Beam inverse solution is not. This difference can be attributed to the underlying full rank EEG that is used to derive the beamforming weights. More variance in future samples will yield larger weights as the moving covariance matrix slides to the right. This example illustrates that the covariance structure based algorithms impose additional temporal smoothing on the inverse solution.

5.4.2 EEG Analysis Using Advanced Methods

5.4.2.1 Eigenspace Projection with Principal Component Analysis

The magnitude of the eigenvalues in Figure 33 suggests two or three possible sources, but without looking at the principal components corresponding to the eigenvalues, we cannot assume that the most dominant sources are epileptic waveforms. The temporal principal components indicate how the power distributed along a given eigenvector fluctuates over time. The temporal principal components are determined via (2.9) and the first eight are plotted on the right hand side of Figure 42.

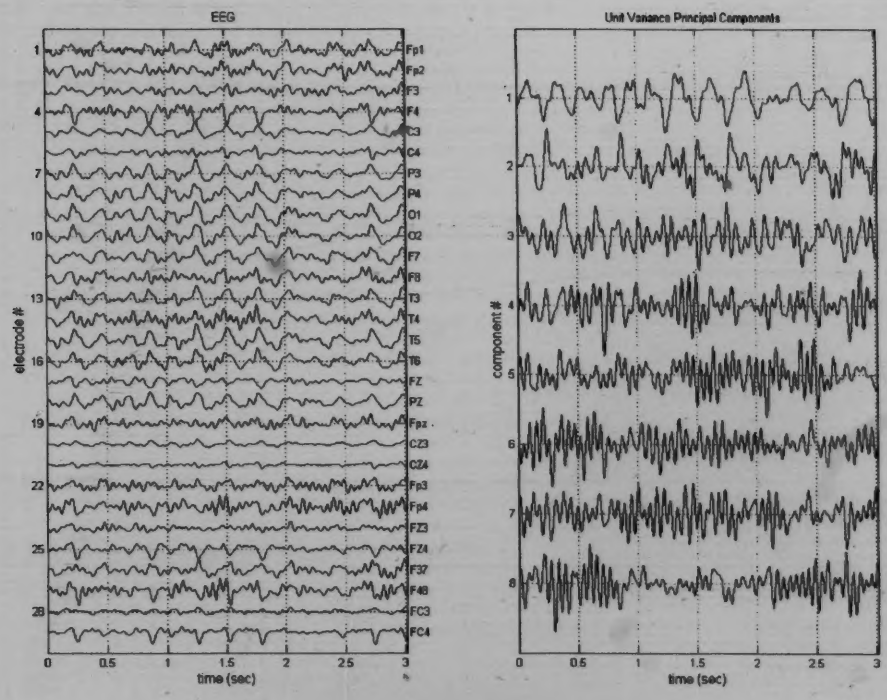

Figure 42 - Temporal principal components
Left side – Original EEG
Right side – First eight temporal principal components

The low frequency waveforms associated with epilepsy are evident to some degree in principal components one through three. The remaining components appear to lack epileptic features.

ES Beam is used to view the inverse solution corresponding to each temporal component. Therefore, if there was a particular component of interest, we can isolate it from the others, regardless of component power.

The full rank EEG is still required to derive the initial beamformer weights. The initial weightings are subsequently projected onto the signal subspace defined by the eigenvector of the desired temporal component to create a new, more specific set of beamformer weights. The weighting vectors are applied to the single rank EEG consisting of the desired component projected onto

the 29 electrode head space. The first three projected principal components are shown in Figure 43.

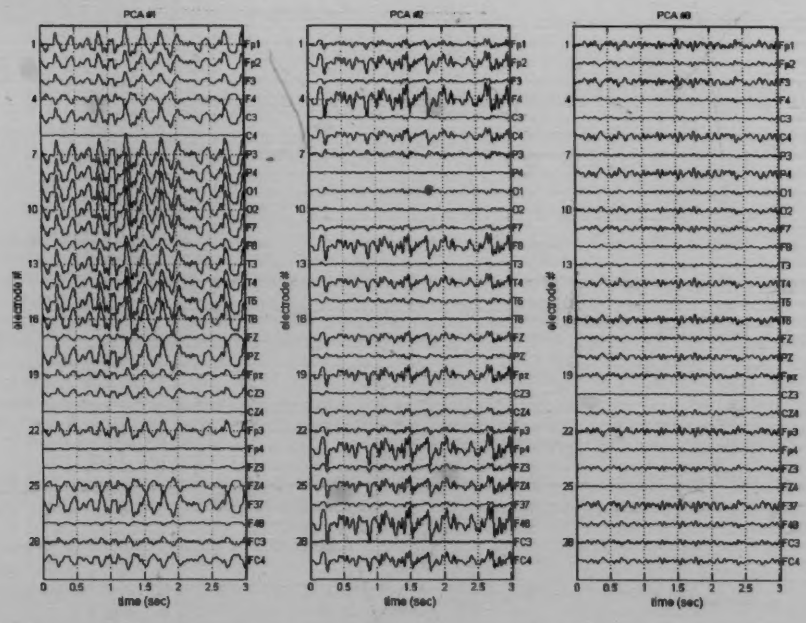

Figure 43 - Three temporal components projected into the 29 electrode measurement space

The magnitude of the EEG traces reinforces that principal component (PC) #3 represents a small portion of power compared to the first two components. PC #1 is relatively symmetrical across the sagittal plane while PC #2 illustrates a great degree of asymmetric behavior between the left and right hemispheres. Inverse solutions for the 63rd slice of PC #1 and PC #2 are determined using ES Beam and shown in Figures 41 and 42.

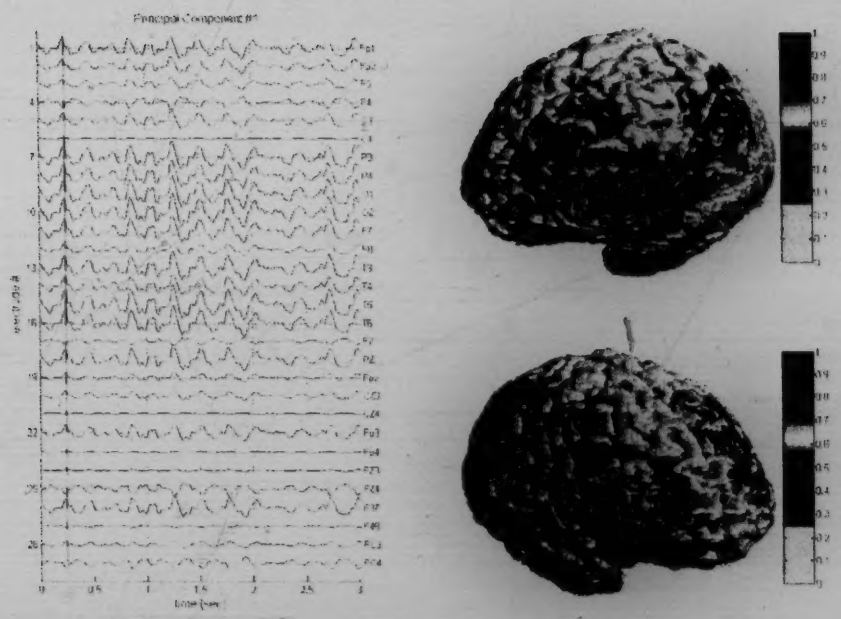

Figure 44 – PC #1 inverse solution

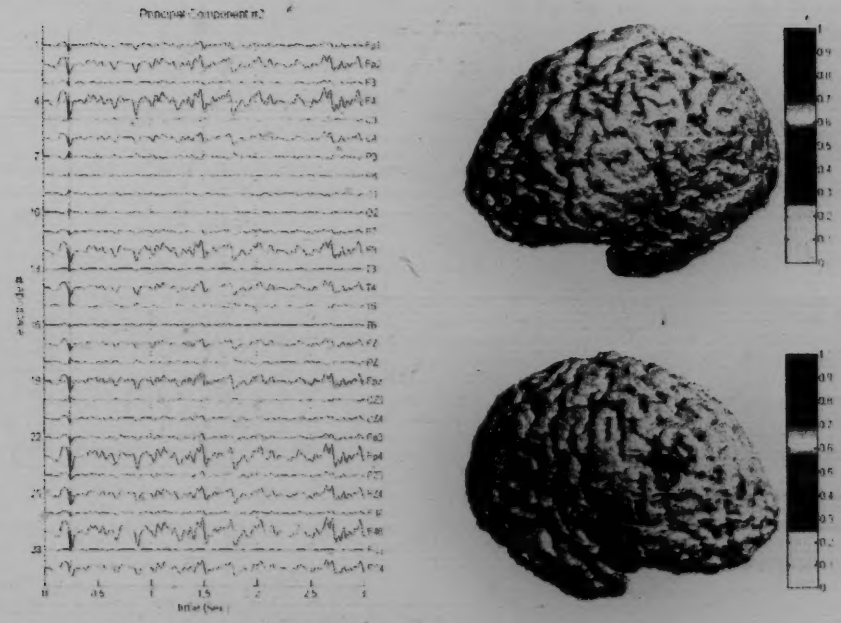

Figure 45 – PC #2 Inverse solution

5.4.2.2 Summary of Principal Component Analysis Localization

Although there are some clear distinctions between the two components, there are also some similarities that must be addressed. Both components seem to produce a well defined peak in the right frontal lobe during the first second of data (although this peak is not evident in PC #1 at n = 63). PC #1 produces a sharp focus in the same location as Figure 45 at 0.86 s. The second component is more consistent in reproducing foci in the same location. During the next second of data, PC #1 becomes more dispersed about the solution space while the second component yields little electrical activity. During the third second of data, a significant portion of power is prevalent in the frontal lobe for both PC #1 and #2. PC #2 even shows significant power of the left hand side during this time interval.

The inverse solutions for PC #1 and #2 were also calculated using MN and LORETA. Both components had concentrated amounts of activity in the front region of the frontal lobe (similar to Figures 34 and 35). This further fuels suspicions that the non-adaptive algorithms are susceptible to biases due to the uneven distribution of electrodes.

5.4.2.3 Eigenspace Projection with Independent Component Analysis

The first four temporal principal components generated in the previous section underwent ICA to formulate four statistically independent time components. The software used to execute the ICA algorithm is the "FastICA" algorithm, freely available online [31]. The four independent time components are displayed in Figure 46.

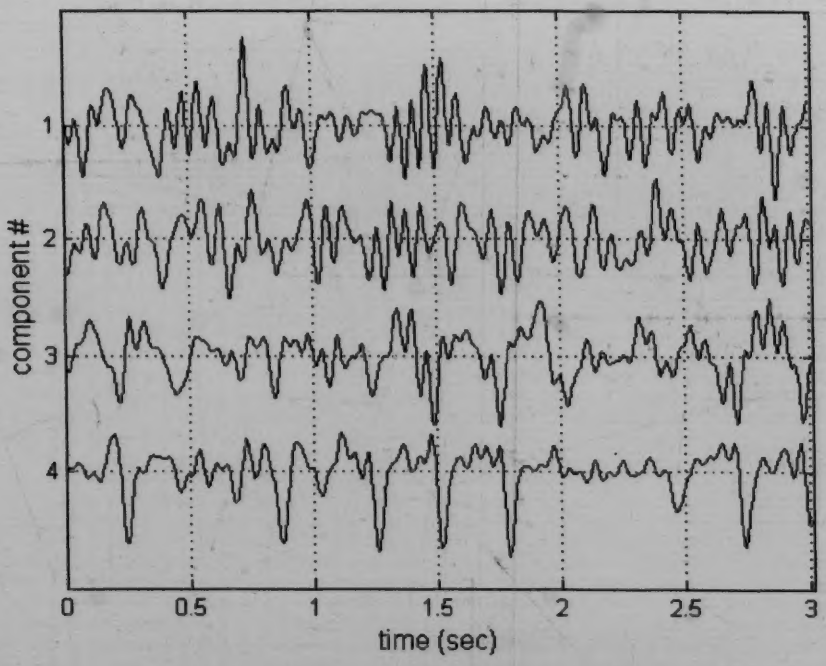

Figure 46 – Four unit variance independent components

Independent components (IC) three and four show the greatest resemblance to the desired "spike and wave" waveform commonly associated with epilepsy. Each component is projected onto the 29 electrode head model to illustrate how each individual component is seen by all 29 electrodes. This helps confirm which components are epileptic in nature. The projection of the i^{th} time component is computed via (5.5).

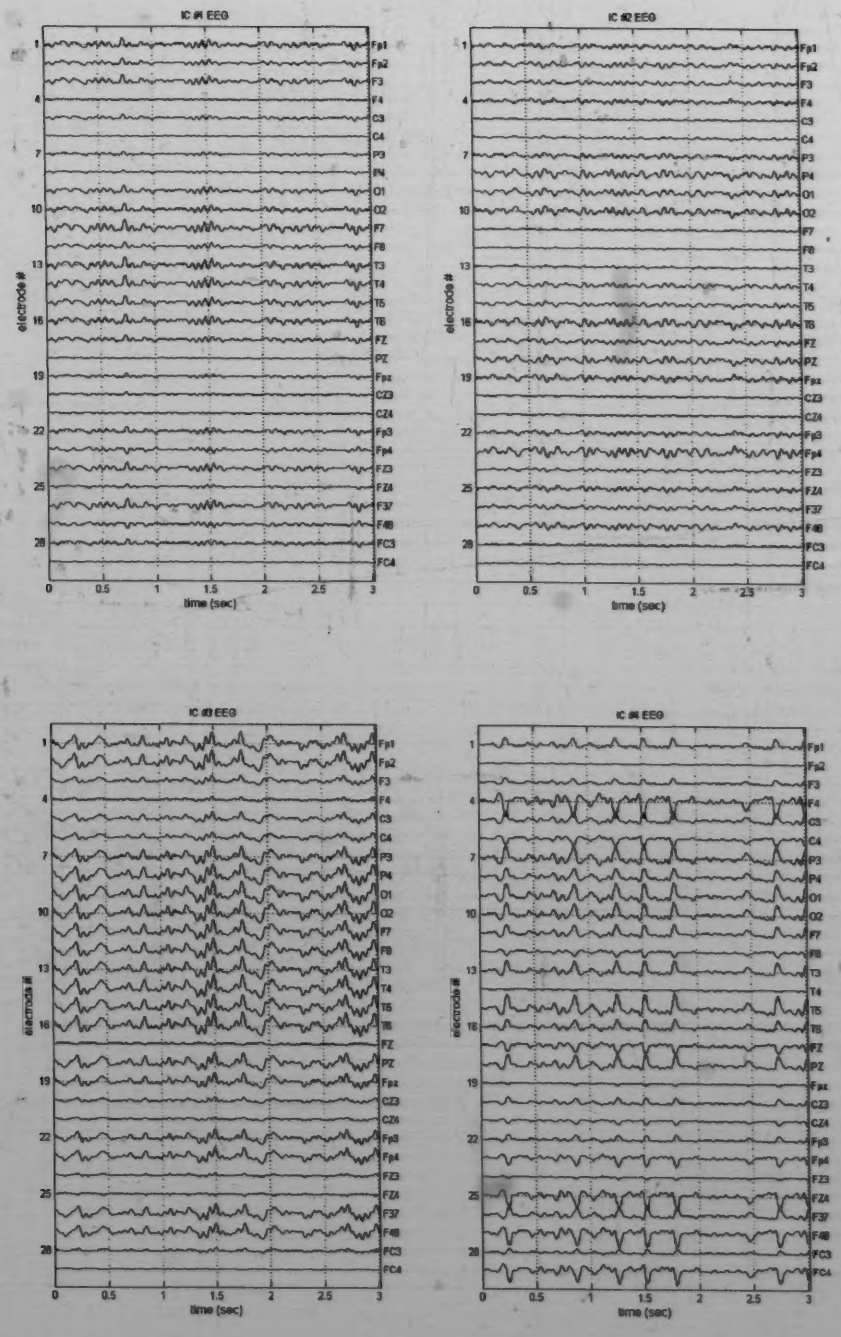

Figure 47 – Four independent components projected into 29 electrode measurement space

As hypothesized earlier, IC #3 and IC #4 show the greatest epileptic characteristics while accounting for 42.2% and 32.9% of the total EEG power respectively. IC #3 possesses very symmetric properties across the sagittal plane while IC #4 has a high degree of asymmetrical behavior.

Unlike other rotations, ICA no longer requires that the corresponding eigenvectors for the independent components are orthogonal. The angle between the eigenvectors for IC #3 and IC #4 is 61.1°.

The individual electrode loadings of the eigenvectors of IC #3 and IC #4 illustrate how the ICA rotation redistributes the electrical sensitivity over the 29 electrodes. With respect to their contributions to overall EEG power and symmetrical behavior, IC #3 is comparable to PC #1 while IC #4 is compared to PC #2. Bar graphs illustrating the differences between the electrode loadings are shown in Figure 48.

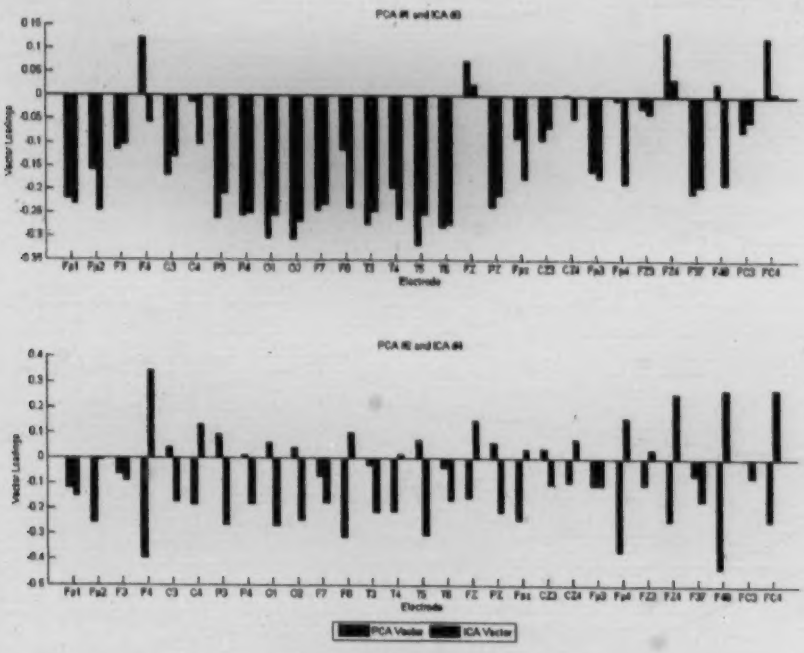

Figure 48 - Comparison of ICA and PCA eigenvectors
Top – PC #1 vs. IC #3
Bottom – PC #2 vs. IC #4

From Figure 48, it is evident that PC #1 and IC #3 are quite comparable. The ICA rotation defines a signal subspace which is more sensitive to fluctuations in electrodes Fp2, F8, T4, Fpz, Fp4, and F48. All six of these electrodes are located in the frontal right hand side on the head. In theory, this should draw the inverse solution for IC #3 towards the frontal right hand side of the solution space. The loadings of IC #4 show no resemblance to PC #2. IC #4 shows high electrode sensitivities at F4, P3, O1, O2, T5, Fz4, F48, and FC4. Unlike IC #3, the high sensitivity electrodes are located at various regions spanning the entire head. This does not bode well for a well-defined localized inverse solution.

The inverse solutions for IC #3 and #4 were calculated ES Beam with the beamformer weights projected onto each components respective subspace.

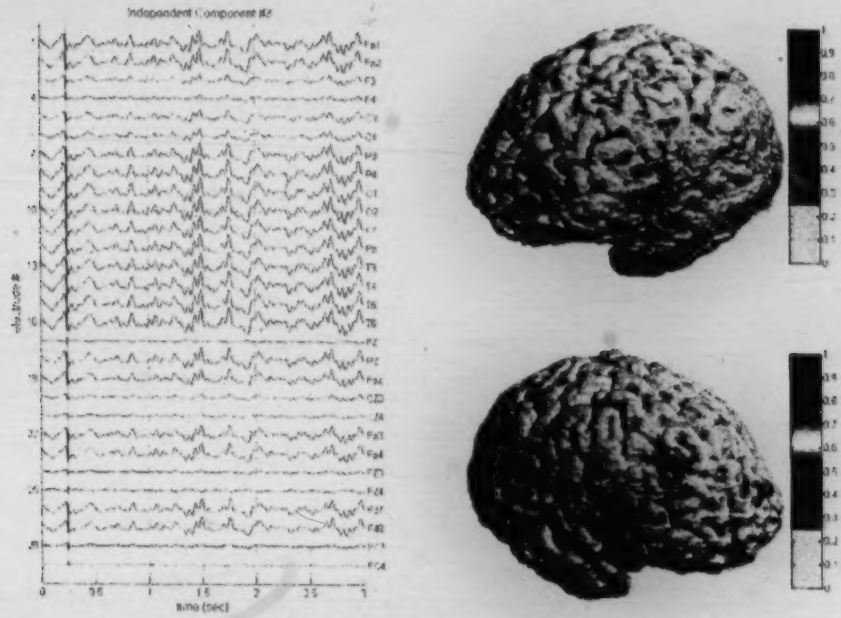

Figure 49 – IC #3 inverse solution

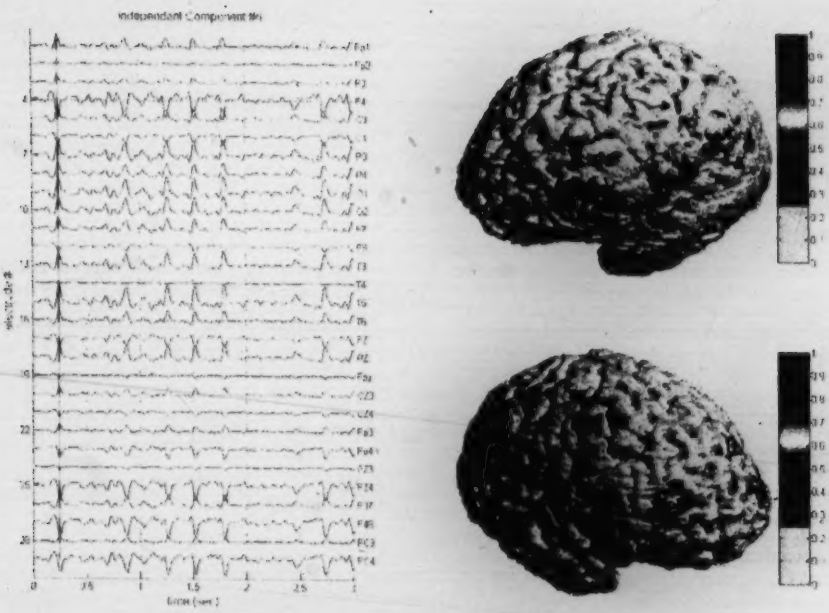

Figure 50 –IC #4 inverse solution

5.4.2.4 Summary of Independent Component Analysis Localization

The inverse solution of IC #3 produces similar electrical foci to those found with ES Beam as well as activity in the right frontal region of the solution space at later times in the EEG. Unlike PC #1, the peak electrical activity of IC #3 is more contained to right hand side of the frontal lobe. This is to be expected based on the increase in the loadings of the electrodes in that region as a result of the ICA rotation. While other inverse solutions migrate to the frontal and left regions of the solution space, IC #3 remains relatively fixed in position.

The loadings of IC #4's eigenvector did not exhibit a focused tendency in the electrode sensitivities like the tendency witnessed for IC #3. Instead, select electrodes spanning the entire solution space experienced increases in sensitivity. This leads us to believe that IC #4 is not a focused epileptic waveform, but some other neurological artifact. The inverse solution corresponding to IC #4 shows a

wide variety of source locations, migrating from the right hand side to left hand side and then to the frontal lobe as time progresses.

It is interesting to note that IC #4 has many identical looking peaks that produce extremely different inverse solutions. Reasons for the extreme differences lie in the underlying full rank covariance matrix used to define the initial beamforming weightings.

5.4.2.5 Eigenspace Projection with Varimax

The varimax rotation rotates the principal components in order to re-distribute the loadings onto a few electrodes while maintaining the orthogonality of the basis vectors. The rotation of the vectors does not alter the spanned subspace. In a similar fashion to ICA, the first four PC's were rotated using the varimax rotation algorithm. The original EEG was projected onto each of the four signal subspaces defined by the four rotated vectors. The effect of the varimax rotation on the first two principal components is shown in Figure 51.

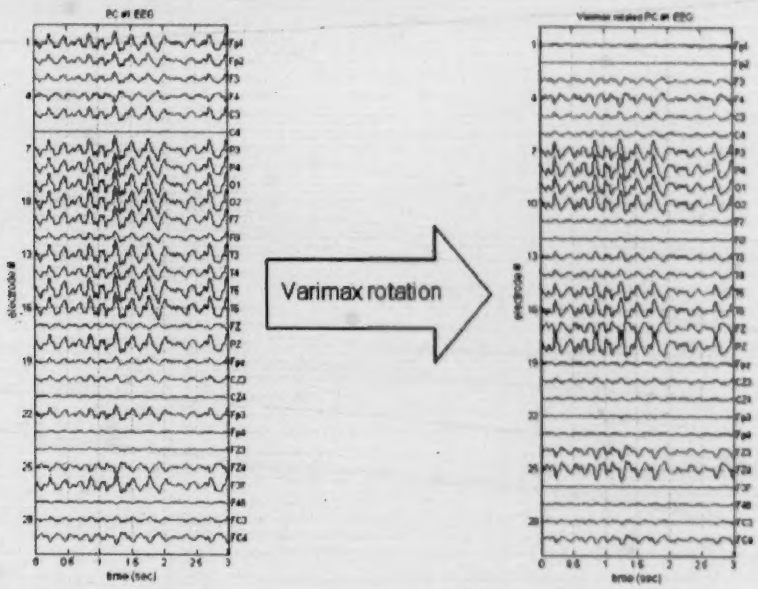

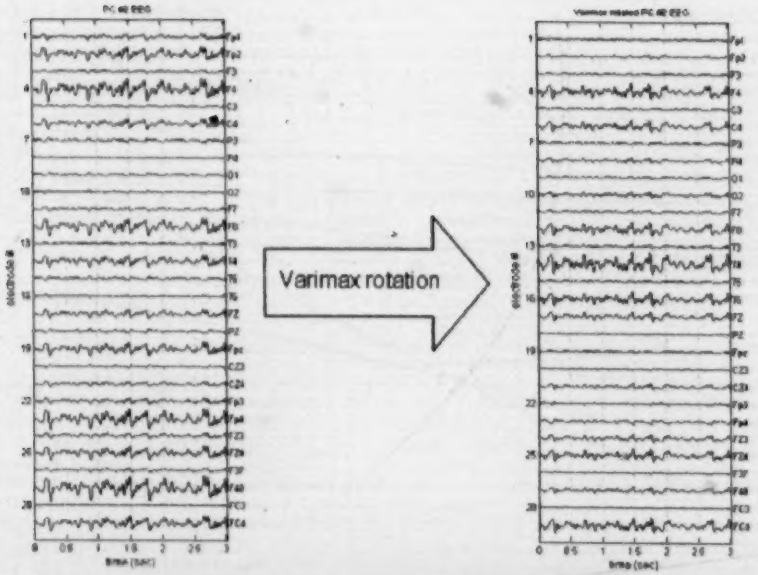

Figure 51 – Effect of the varimax rotations on the back projected principal components
Top – PC #1 (top, left), rotated PC #1 (top, right)
Bottom – PC #2 (bottom, left), rotated PC #2 (bottom, right)

The magnitude of the electrode loadings for both the original spatial PC and the corresponding varimax rotated spatial PC are shown for the first two components in Figure 52.

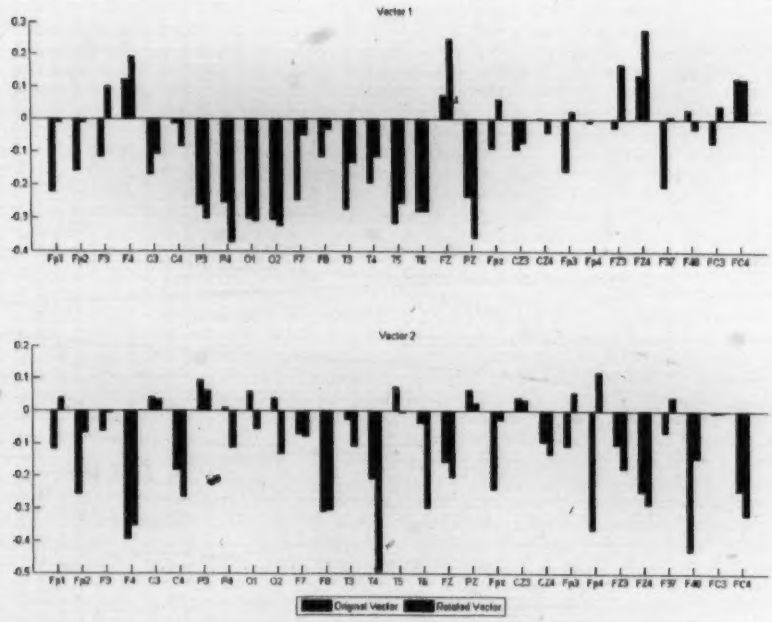

Figure 52 - Comparison of PC and rotated PC eigenvectors
Top - PC #1
Bottom - PC #2

For PC #1, the varimax rotation substantially increases the loadings/sensitivities of electrodes F4, C4, P4, Fz, Pz, FZ4, while switching the polarity of FZ3. With the exception of FZ3, these electrodes all reside in central-right hand side of the solution space. For PC #2, electrodes increasing in sensitivity are: C4, P4, O2, T4, T6, while the frontal right hand side electrodes (Fp2, F4, Fpz, Fp4, and F48) all experience a decrease in sensitivity. Initial investigation, leads us to believe that the inverse solution will be biased towards the right hand side of the temporal and occipital lobes.

The inverse solutions for the two varimax rotated components were calculated using ES Beam with the aforementioned subspace projection techniques.

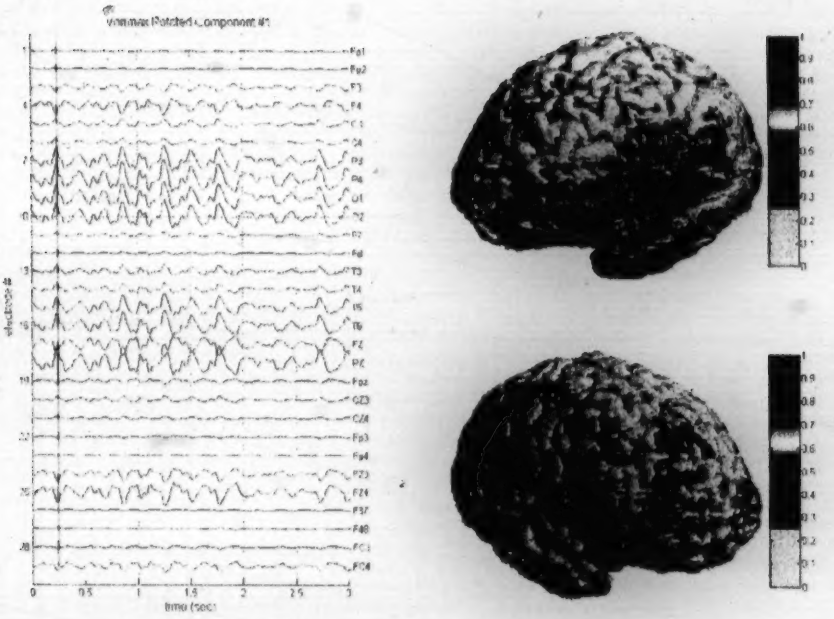

Figure 53 – Varimax rotated PC #1 inverse solution

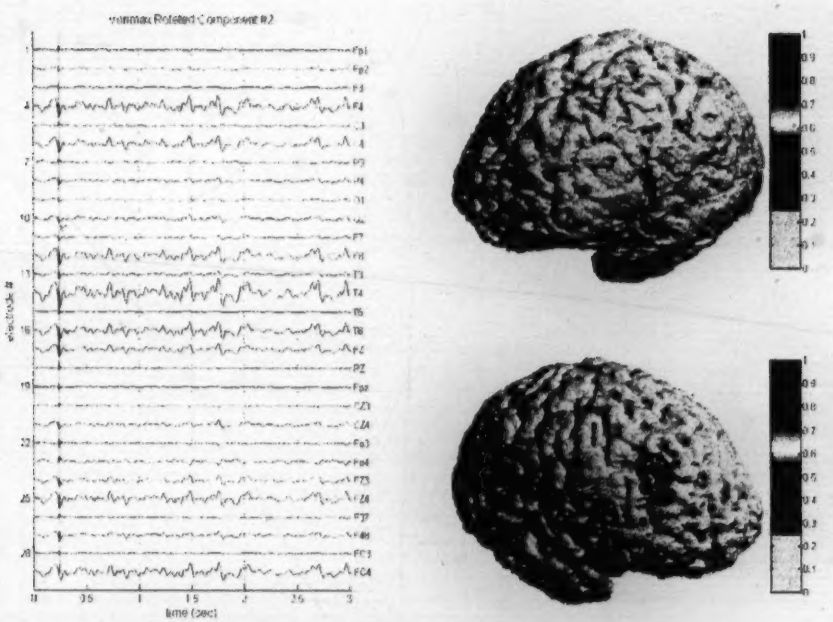

Figure 54 – Varimax rotated PC #2 inverse solution

5.4.2.6 Summary of Varimax Rotation Localization

Ideally the varimax rotation would place the emphasis on a few electrodes and would help reduce noise and background electrical activity by suppressing the data observed at other electrodes. Unfortunately, the observed inverse solutions for both of the rotated electrodes did little clarify matters.

Each spike in the rotated PC #1 EEG yielded very dispersed inverse solutions. The most focused inverse solution occurred at 2.75 s and was confined to the front of the frontal lobe. This is an unexpected result given that the single rank EEG shows very little activity at electrodes Fp1 and Fp2.

The second varimax rotated PC produced focused inverse solutions that resided in the right hand side of the frontal lobe (see Figure 54) for all of the peaks in the first half of the data. During the second half of the data, the foci bounced around the left and right hand side of the frontal lobe with a higher degree of dispersion. Again, this is an unexpected result based on the decrease in sensitivities for the electrodes located on the right hand side of the frontal region of the scalp. Although the second rotated component still produces foci in the common location, the inverse solutions do not seem intuitive based on the single rank EEG.

5.5 Discussion

Two focused locations dominated the above studies. The non-adaptive algorithms yielded a focused region at the front of the frontal lobe while many of the adaptive algorithms yielded sources on the right hand side of the frontal lobe. The diagnosis of the clinicians treating the patient agrees more favorably with the results obtained with the adaptive, eigenspace projected algorithms than the non-adaptive algorithms. Their professional diagnoses in conjunction with the superior results of the adaptive techniques seen in Chapters 3 and 4, leads us towards the source locations obtained with adaptive algorithms. Additional signal subspace factoring techniques such as principal component analysis, temporal

independent component analysis, and the varimax rotation did little to clarify the situation.

The unintuitive results obtained when mapping single components illustrate how the beamformers are handicapped by the full rank EEG. For the adaptive inverse solutions, the covariance matrix used to define the initial beamforming weights was calculated using a 257 sample, moving window of data. Theoretically, this should increase the adaptability of these algorithms because the weightings are constantly adjusted to the changing covariance structure, providing more representative results. For comparison, videos were also made with the various beamforming techniques that had a fixed covariance structure based on all 772 samples. These videos were much more intuitive than the ones mentioned in previous sections because similar EEG spikes produced similar looking inverse solutions. On the other hand, we can show several examples where single spikes in the projected, single component EEG look the same, but the underlying full rank covariance matrix is quite different. This produces two different inverse solutions for what appears to be the same neurological event. The fixed covariance matrix method localizes to the same point at both instances in time while the variable covariance matrix method does not. Although the fixed covariance matrix method produces better looking and more intuitive results, we cannot assume them to be more accurate.

A potentially large source of error with the analysis of the EEG data and the corresponding head model is the conflicting EEG referencing techniques. The lead field matrix was derived assuming a common reference while the data was collected using a linked electrode montage. The erroneous effects produced by this discrepancy are unquantifiable. To try and reduce the complications introduced by combining the two techniques, the two rows of data that were collected at the linked electrodes were omitted from the EEG data. Removing the two electrodes increases the underdetermined nature of the inverse problem.

The derivation of the lead field matrix also assumed that the various tissue types were isotropic in nature. This approximation makes the derivation much

less burdensome, but does introduce additional inaccuracies in the lead field matrix. In reality, the human head is highly anisotropic with conductivity differences of 1:10 for the radial and tangential directional components of the skull and a 10:1 difference in directions parallel and normal to the nerve fibers in the white matter [32]. Therefore, ignoring the anisotropic conductivities of our current head model will yield a less accurate lead field matrix and hinder the localizing ability of all of the investigated inverse algorithms.

To enhance the quality of the EEG source localization results, a greater EEG sampling frequency is required to show the chronological order of seizure propagation. Depending of the amount of myelin insulation coating an axon, the speed of propagation of an action potential ranges from 0.5 m/s to 100 m/s [33]. Assuming that the maximum diameter of the head is 20 cm, the amount of time for an action potential to propagate to the opposite side of the head ranges from 0.4 s to 2 ms. The current EEG sampling rate of 256 Hz translates to a 3.9 ms sampling interval. Therefore, the dynamics of action potential propagation cannot be deciphered for faster moving signals. The corresponding inverse solution will look like two distinct sources instead of a single source propagating outwards. Increasing the EEG sampling frequency will provide additional information to emphasize the propagation of epileptic foci.

Another possible source of error for the non-adaptive algorithms is the concentration of the electrodes around the frontal lobe. The additional electrodes were placed there to improve the spatial resolution in that region, but as shown in previous chapters, an uneven electrode density can bias the non-adaptive inverse solutions.

Chapter 6 - Conclusions and Future Work

6.1 Conclusions

The adaptive beamforming methods showed great promise in their ability to accurately localize simulated sources while limiting solution dispersion. Compared to the non-adaptive algorithms, the beamformers showed an unparallelled robustness to noise and were not as heavily biased by the electrodes. In addition, beamformers exhibited a positive correlation between localization accuracy and electrode density that could be further exploited to improve results.

Two source locations typically prevailed in our analysis of the clinically obtained inter-ictal EEG in Chapter 5. The non-adaptive algorithms produced results at the very front of the frontal lobe while the adaptive algorithms typically localized the source to the right hand side of the frontal lobe. The epileptogenic zone specified by the eigenspace projected beamformer agreed with the general region diagnosed by the clinicians treating the patient further enhancing our confidence in the algorithm. Trying to isolate specific epileptic waveforms via PCA, ICA, and the varimax rotation appeared to confirm previous diagnoses, but did little to further improve matters. Mind you, the selection of epileptic waveforms and components is a rather subjective process that would benefit greatly from the expertise of an epileptologist and/or a neurologist.

Although the eigenspace projection beamformer agreed within reason to the clinical diagnosis, there is no gold standard with which to properly quantify the performance of the various algorithms for the clinical data analyzed in Chapter 5.

6.2 Future Work

The quality of the inverse solution is proportional to the accuracy of the forward solution. Therefore, future work should lean towards improving the accuracy of

the lead field matrix. As mentioned earlier, more accurate tissue conductivities with anisotropic properties are required in order to formulate a more accurate head model. Future experiments analyzing the effect of different skull to cortex ratios could shed light on the poor performance of the non-adaptive algorithms in Chapter 4 where a more highly resistive skull was used to define the three concentric shell head model.

In Chapter 3, 100 randomly located single source locations were used to estimate the localization error for each algorithm. Time permitting; a more effective measure of localization error would incorporate a trial performed at each possible source location. In addition to providing a more conclusive mean value, a three dimensional head model map could display the localization error associated with each source location. This map could be used to determine the relationship between the head model anatomy and source localization error and assist in redefining/incorporating anatomical related weightings for the non-adaptive inverse algorithms.

Future experiments of this nature should be more conscientious with respect to the data acquisition to avoid having conflicting reference points between the lead field matrix and the data. The effect this oversight has on the results obtained in Chapter 5 is unquantifiable and possibly quite substantial.

The lack of knowledge with respect to the seizure source location made it very difficult to assess the performance of the various inverse solutions. Therefore, it would be advantageous to combine EEG with fMRI data in order to cross reference the individual results with one another. Although fMRI has poor temporal resolution, it could provide a much needed spatial baseline to assess each of the algorithms.

Reference List

[1] All About Epilepsy and Siezures. Retrieved March 20, 2006. http://www.epilepsy.com/101/ep101_epilepsy.html

[2] Malmivuo J, P. R. Electroencephalography. In: *Bioelectromagentism - Principles and Applications of Bioelectric and Biomagnetic Fields*, New York, USA: Oxford University Press, 1995.

[3] Baillet S, M. J. L. R., Electromagnetic brain mapping *IEEE Signal Processing Magazine*, vol. 18, pp. 14-30, 2001.

[4] Tsai, J. Nervous System. In: *Bioinstrumentation*, ed. John G. Webster. John Wiley & Sons, Inc., 2004.pp. 228-236.

[5] Michel CM, M. M. L. G. G. S. S. L., EEG source imaging *Clinical Neurophysiology*, vol. 115, pp. 2195-2222, 2004.

[6] Pascual-Marqui RD, Review of methods for solving the EEG inverse problem *International Journal of Bioelectromagnetism*, vol. 1, pp. 75-86, 1999.

[7] Sarvas J, Basic mathematical and electromagnetic concepts of the biomagnetic inverse problem *Phys Med Biol*, vol. 32, pp. 11-22, 1987.

[8] Vanrumste B, EEG dipole source analysis in a realistic head model, PhD Dissertation 2002. Ghent University.

[9] Vanrumste, B., Van Hoey, G., Van de Walle, R., D'Have, M. R., Lemahieu, I. A., and Boon, P. A., The validation of the finite difference method and reciprocity for solving the inverse problem in EEG dipole source analysis *Brain Topogr*, vol. 14, pp. 83-92, Winter, 2001.

[10] Neilson, L. A., Kovalyov, M., and Koles, Z. J., A computationally efficient method for accurately solving the EEG forward problem in a finely discretized head model *Clin Neurophysiol*, vol. 116, pp. 2302-14, Oct, 2005.

[11] David J. Griffiths. *Introduction to Electrodynamics*, Upper Saddle River, New Jersey, USA: Prentice Hall, 1999.

[12] Huang, M. X., Shih, J. J., Lee, R. R., Harrington, D. L., Thoma, R. J., Weisend, M. P., Hanlon, F., Paulson, K. M., Li, T., Martin, K., Millers, G. A., and Canive, J. M., Commonalities and differences among vectorized beamformers in electromagnetic source imaging *Brain Topogr*, vol. 16, pp. 139-58, Spring, 2004.

[13] Sekihara K, N. S. P. D. M. A. M. Y., Reconstructing spatio-temporal activities of neural sources using an MEG vector beamformer technique *IEEE Transactions on Biomedical Engineering*, vol. 48, pp. 760-771, 2001.

[14] Spencer ME, L. R. M. J. L. P., Adaptive filters for monitoring localized brain activity from surface potential time series *Conference Record of the Twenty-Sixth Asilomar Conference on Signals, Systems, and Computers*, vol. 1, pp. 156-61, 1992.

[15] Van Veen, B. D., van Drongelen, W., Yuchtman, M., and Suzuki, A., Localization of brain electrical activity via linearly constrained minimum variance spatial filtering *IEEE Trans Biomed Eng*, vol. 44, pp. 867-80, Sep, 1997.

[16] Sekihara K, N. S. Neuromagnetic source reconstruction and inverse modeling. In: *Modeling and Imaging of Bioelectric Activity - Principles and Applications*, ed. He B. New York, USA: Kluwer Academic/Plenum Publishers, 2004.pp. 213-250.

[17] Mosher, J. C., Lewis, P. S., and Leahy, R. M., Multiple dipole modeling and localization from spatio-temporal MEG data *IEEE Trans Biomed Eng*, vol. 39, pp. 541-57, Jun, 1992.

[18] Martin JH. The Collective Electrical Behavior of Cortical Neurons: The Electroencephalogram and the Mechanisms of Epilepsy. In: *Principles of Neural Science*, ed. Kandel ER, S. J. J. T. Norwalk, Connecticut, USA: Appleton & Lange, 1991.pp. 777-791.

[19] Withey D, Dynamic Edge Tracing: Recursive Methods for Medical Image Segmentation, PhD Dissertation 2006. University of Alberta.

[20] Haueisen, J., Tuch, D. S., Ramon, C., Schimpf, P. H., Wedeen, V. J., George, J. S., and Belliveau, J. W., The influence of brain tissue anisotropy on human EEG and MEG *Neuroimage*, vol. 15, pp. 159-66, Jan, 2002.

[21] Haueisen, J., Ramon, C., Eiselt, M., Brauer, H., and Nowak, H., Influence of tissue resistivities on neuromagnetic fields and electric potentials studied with a finite element model of the head *IEEE Trans Biomed Eng*, vol. 44, pp. 727-35, Aug, 1997.

[22] Koles, Z. J., Trends in EEG source localization *Electroencephalogr Clin Neurophysiol*, vol. 106, pp. 127-37, Feb, 1998.

[23] Leahy RM, M. J. S. M. H. M. L. J., A study of dipole localization accuracy for MEG and EEG using a human skull phantom *Electroencephalogr Clin Neurophysiol*, vol. 107, pp. 159-73, 1998.

[24] Hwang D, N. S. P. O. S. K., Multiresolution MEG (Magnetoencephalography) Imaging by Adaptive Beamformer Scanning *Proceedings of the 25th Annual International Conference of the IEEE EMBS, Cancun Mexico*, vol. pp. 955-8, Sep 17, 2003-Sep 21, 2003.

[25] Ary, J. P., Klein, S. A., and Fender, D. H., Location of sources of evoked scalp potentials: corrections for skull and scalp thicknesses *IEEE Trans Biomed Eng*, vol. 28, pp. 447-52, Jun, 1981.

[26] Electrical Geodesics, Inc. Retrieved February 27, 2007. www.egi.com

[27] Katznelson RD. EEG recording, electrode placement, and aspects of generator localization. In: *Electric Fields of the Brain*, ed. Nunez, P. New York: Oxford University Press, 1981.pp. 176-213.

[28] Smith, LI. A tutorial on principal component analysis. Retrieved December 11, 2006. http://csnet.otago.ac.nz/cosc453/student_tutorials/principal_components.pdf

[29] Hyvarinen, A. and Oja, E., Independent component analysis: algorithms and applications *Neural Netw*, vol. 13, pp. 411-30, May, 2000-Jun 30, 2000.

[30] Abdi H, Factor Rotations in Factor Analyses 2003.

[31] Hyvarinen, Aapo. The FastICA package for MATLAB. Retrieved October 5, 2006. http://www.cis.hut.fi/projects/ica/fastica/

[32] Wolters, C. H., Anwander, A., Tricoche, X., Weinstein, D., Koch, M. A., and MacLeod, R. S., Influence of tissue conductivity anisotropy on EEG/MEG field and return current computation in a realistic head model: a simulation and visualization study using high-resolution finite element modeling *Neuroimage*, vol. 30, pp. 813-26, Apr 15, 2006.

[33] R.H.S.K. Widmaier EP. *Vander, Sherman, & Luciano's Human Physiology: The Mechanisms of Body Function,* McGraw Hill Higher Education, 2004.

[34] Papoulis A, P. S. *Probability, Random Variables and Stochastic Processes,* New York, USA: McGraw Hill, 2002.